

Stephan Putzke

---

Doktorarbeit

# Alternating-gradient focusing of large neutral molecules

Erstellt am Fritz-Haber-Institut  
der Max-Planck-Gesellschaft



im Fachbereich Physik der  
Freien Universität Berlin eingereichte Dissertation

Berlin, 2012

---

- 1. Gutachter** Prof. Dr. Gerard J. M. Meijer  
Fritz-Haber-Institut der Max-Planck-Gesellschaft  
Freie Universität Berlin
  - 2. Gutachter** Prof. Dr. Ludger Wöste  
Freie Universität Berlin
- Disputation** 28. November 2012

## Kurzfassung

Im Rahmen dieser Arbeit wurde ein neues Molekularstrahlexperiment aufgebaut, das es erlaubt, große neutrale polare Moleküle zu fokussieren und zu transportieren. Die Fokussierung basiert auf der Stark-Wechselwirkung der Moleküle mit zeitlich veränderlichen inhomogenen elektrischen Feldern unter Anwendung der Methode der alternierenden Gradienten (AG). Ziel war es, den Transport durch die elektrischen Felder auf Moleküle mit einem Masse-zu-Dipolmoment-Verhältnis ( $m/\mu$ ) innerhalb einer schmalen Bandbreite zu beschränken, analog zur Selektion von Ionen mit bestimmten Masse-zu-Ladungs-Verhältnissen ( $m/q$ ) im Quadrupolmassenspektrometer.

Für die Charakterisierung des Aufbaus wurde ein gepulster Molekularstrahl verwendet. Die Detektion der transportierten Moleküle erfolgte rotationsaufgelöst per laserinduzierter Fluoreszenzspektroskopie. Als prototypisches Molekül wurde Benzonitril ( $C_6H_5CN$ ) gewählt, das ein für die AG-Fokussierung günstiges  $m/\mu$ -Verhältnis besitzt und gut zu detektieren ist. In Abhängigkeit von der angelegten Schaltfrequenz wurde die Verteilung der fokussierten Moleküle als Funktion der Ankunftszeit und der transversalen Geschwindigkeit bestimmt. Die  $\mu/\Delta\mu$ -Auflösung hängt von der Form der Schaltsequenz ab. Der erreichte Wert von 20 ist ausreichend, um ausschließlich Benzonitrilmoleküle im absoluten Grundzustand und in Rotationszuständen mit demselben Dipolmoment zu transportieren. Entscheidend ist dabei die erreichte Genauigkeit der elektrischen Felder durch eine magnetische Halterung der Hochspannungselektroden. Die experimentellen Ergebnisse stimmen gut mit Trajektorienimulationen überein.

Am Beispiel der Fokussierung des Benzonitril-Argon van der Waals-Komplexes wurde demonstriert, wie Moleküle mit gleichem Dipolmoment, jedoch verschiedener Masse selektiert werden können. Der Komplex war ebenfalls im Molekularstrahl enthalten. Durch die Untersuchung der Transmissionscharakteristika konnte gezeigt werden, dass er dasselbe permanente Dipolmoment wie Benzonitril trägt. Durch die Wahl geeigneter Schaltfrequenzen konnte die Transmission der beiden Spezies auf Benzonitril beschränkt werden.

Mittels der AG-Fokussierung kann der Anwendungsbereich der Stark-Abbremsung auf große Moleküle erweitert werden. Die Leistungsfähigkeit des sogenannten AG-Abbremsers hängt entscheidend von der Genauigkeit der erzeugten elektrischen Felder ab. Im letzten Teil dieser Arbeit wird die Charakterisierung eines neuen AG-Abbremsers gezeigt, der in unserer Arbeitsgruppe neu aufgebaut wurde. Es stellte sich jedoch heraus, dass die Transmission selbst bei der erzielten präzisen Ausrichtung der Hochspannungselektroden zu gering ist, um das angestrebte Fangen großer Moleküle in einer Falle zu realisieren.

## Abstract

This thesis describes experiments using a second generation alternating-gradient (AG) focuser for large molecules. A beam of polar molecules is focused and transported through the switched electric fields of the quadrupole. The device is a quantum-state selector, since, at a given switching frequency, the transmission of the guide depends on the mass-to-dipole-moment ( $m/\mu$ ) ratio of the quantum state that the molecule is in. The working principle is closely related to that of the quadrupole mass spectrometer, which exploits the mass-to-charge ratio ( $m/q$ ) of charged particles to restrict the transmission to a narrow  $m/q$ -range.

The  $m/\mu$ -selector is characterized in detail using a pulsed beam of benzonitrile ( $C_6H_5CN$ ), a prototypical large molecule, in combination with rotational quantum state resolved detection. The arrival time distribution as well as the transverse velocity distribution of the molecules exiting the selector are measured as a function of the ac frequency. The  $\mu/\Delta\mu$ -resolution of the selector can be controlled by the applied ac waveforms and a value of up to 20 can be obtained with the present setup. This is sufficient to exclusively transmit benzonitrile molecules in quantum states with the same  $m/\mu$ -value as the absolute ground state. The operation characteristics of the  $m/\mu$ -selector are in quantitative agreement with the outcome of trajectory simulations. Crucial for the good performance of the AG focuser is the accuracy of the generated electric fields due, for instance, to the employed magnetic holding scheme, resulting in a high transmission.

Not only is it possible to select quantum states of a given molecule by their dipole moment, but also molecules having the same dipole moment and different masses can be separated. This is demonstrated by AG focusing the benzonitrile-argon van der Waals complex, which is also present in the benzonitrile beam. The complex is formed between benzonitrile molecules and argon atoms from the seed gas and its electric dipole moment is found to be the same as for benzonitrile by comparing the transmission characteristics of the two species. Based on their different masses, the transmission of the two molecules can be restricted to benzonitrile by applying suitable ac waveforms.

Using AG focusing, the Stark-deceleration technique can be extended to work not only for molecules in low-field-seeking quantum states, but, in principle, also for high-field-seeking molecules. In the last part of this work, the extended AG decelerator that has been set up in our group is characterized. The performance of the device, as for the selector, critically depends on the accuracy of the electric fields and, thereby, on the alignment of the high-voltage electrodes. At the presently achieved level of accuracy, the transmission is found to be very limited, prohibiting the efficient deceleration and envisioned trapping of large, high-field-seeking molecules.

# Contents

<b>1</b>	<b>Introduction</b>	<b>7</b>
<b>2</b>	<b>Large molecules in electric fields</b>	<b>11</b>
2.1	Asymmetric-rotor molecules in electric fields . . . . .	11
2.1.1	Rotational energy levels . . . . .	11
2.1.2	Numerical calculation of energy levels . . . . .	15
2.1.3	Transitions and excitation spectra . . . . .	15
2.2	Molecular properties of benzonitrile and the benzonitrile-argon complex . . . . .	17
<b>3</b>	<b>Alternating-gradient focusing</b>	<b>21</b>
3.1	General principles of alternating-gradient focusing . . . . .	21
3.1.1	Electrode geometries . . . . .	22
3.1.2	Stability and the duty cycle . . . . .	24
3.2	Numerically simulating the ac electric quadrupole selector . . . . .	27
3.2.1	Numerical simulation of the electric field . . . . .	27
3.2.2	Numerical trajectory simulations . . . . .	29
3.3	Alternating-gradient deceleration . . . . .	31
<b>4</b>	<b>Setup</b>	<b>37</b>
4.1	Molecular beam setup . . . . .	38
4.1.1	Vacuum system . . . . .	38
4.1.2	Source . . . . .	38
4.2	The ac electric selector . . . . .	40
4.2.1	Design . . . . .	40
4.2.2	High-voltage electronics and switching scheme . . . . .	44
4.3	Rotational-state-specific detection . . . . .	47
4.3.1	Laser system . . . . .	47
4.3.2	Laser-induced-fluorescence (LIF) detection . . . . .	48
4.3.3	Laser-frequency stabilization . . . . .	49
<b>5</b>	<b>Rotational-state-specific guiding of benzonitrile</b>	<b>57</b>
5.1	Fluorescence excitation spectra . . . . .	57
5.2	AC frequency scans . . . . .	63
5.3	Rotational-state-selective transmission . . . . .	67
5.4	Stark-energy calculations . . . . .	67
5.5	Trajectory calculations . . . . .	70
5.6	Transmission of molecules in individual $M$ -components . . . . .	73

5.7	Resolution . . . . .	76
5.8	Transmission vs. field strength . . . . .	76
5.9	Phase effects . . . . .	77
5.10	Conclusions . . . . .	83
<b>6</b>	<b>Alternating-gradient focusing of the benzonitrile-argon complex</b>	<b>85</b>
6.1	LIF spectra and discussion . . . . .	85
6.2	Frequency-dependent transmission curves and discussion . . . . .	88
6.3	Conclusions . . . . .	92
<b>7</b>	<b>The alternating-gradient decelerator</b>	<b>95</b>
7.1	Experimental details . . . . .	95
7.2	Focusing and deceleration of benzonitrile . . . . .	96
7.3	Discussion and outlook . . . . .	99
<b>8</b>	<b>Summary and outlook</b>	<b>105</b>
	<b>Bibliography</b>	<b>107</b>
	<b>List of publications</b>	<b>115</b>
	<b>Curriculum vitae</b>	<b>117</b>
	<b>Selbstständigkeitserklärung</b>	<b>119</b>
	<b>Danksagung</b>	<b>121</b>
<b>A</b>	<b>Laser-frequency stabilization</b>	<b>123</b>
A.1	Components . . . . .	123
A.2	Peak detection . . . . .	124
A.3	Input logic - signal processing . . . . .	124
A.4	Software stabilization loops . . . . .	125

# Chapter 1

## Introduction

A detailed knowledge of molecular properties is essential in order to understand everyday processes, for example in biology, climate research and astrophysics. Since the early days, when the existence of molecules was still to be proven by the physics Nobel laureate Jean Perrin (awarded 1926), the field of molecular physics has made tremendous progress. Today, full control over the internal and external degrees of freedom of molecules seems within reach [1, 2].

Molecules commonly have a complicated energy-level structure. With increasing size, their degrees of freedom grow rapidly and their theoretical description becomes evermore sophisticated. The title of this thesis immediately raises the question: "What is a *large* molecule?" In the context of the manipulation of polar molecules, the size of a molecule can be classified by the character of the interaction with an electric field as detailed below. To anticipate the classification, molecules of the size of carbon monoxide and ammonia, for example, are considered small, while benzonitrile, the prototypical large molecule used in the reported experiments, is considered large.

Meaningful experiments need a controlled setting. The properties of molecules are naturally influenced by the surrounding environment, be it in the gaseous phase, e. g., in the atmosphere, or the liquid phase, e. g., in biological systems. To achieve an isolated environment in which molecules are free from collisions and interactions, for example, with other molecules, solvents, or containers, the molecular beam method has proven to be versatile. Molecular beams have played a central role in many experiments in physics and chemistry and have found a wide range of applications [3].

For many of these applications it is crucial that the internal quantum state distribution of the molecules in the beam is accurately known and that it can be controlled. The cooling of molecules in an adiabatic expansion strongly reduces the number of populated levels, thereby tremendously simplifying the optical spectra of the molecules [4]. For large molecules, however, many levels will still be populated at the low temperatures ( $\approx 1$  K) that can be achieved in a molecular beam. Moreover, even at the lowest possible temperatures, molecules with a complex potential energy landscape like bio-molecules, are known to be frozen into different minima and to be present in various conformational structures in the beam [5].

Therefore, to control the quantum-state distribution (and thereby the conformational distribution) of large molecules in a beam, additional filtering techniques need to be applied. This can be achieved with electric, magnetic or optical fields, or any combination thereof [1, 6–9, and references therein]. Recent developments of techniques to control

(mostly) molecular beams of small molecules include the quantum-state selective deceleration using microwave radiation [10], optical fields [11, 12], and traveling electric fields [13, 14].

A wide variety of electric field geometries has been used in the past to control the trajectories of polar molecules in a beam. The original geometries were devised to create strong electric field gradients on the beam axis to efficiently deflect molecules. As early as 1921, Fritz Reiche and Hartmut Kallmann proposed to spatially separate polar molecules by dipole-moment-dependent deflection in inhomogeneous electric fields [15].<sup>1</sup> In fact, the proposal stimulated Otto Stern to announce the analogous, so-called Stern-Gerlach experiment about a year ahead of its successful implementation [17]. In their ground breaking experiment, in 1922, Stern and Gerlach demonstrated the quantization of the magnetic moment by spatial separation of silver atoms using inhomogeneous *magnetic* fields [18, 19]. Electric deflection was experimentally demonstrated later in 1927 by Wrede [20], a graduate student of Stern, and similar experiments were conducted, mostly to measure dipole moments of molecules [21–23].

Later, electric field geometries were designed to focus molecules in selected quantum states further downstream of the molecular beam [24]. For these experiments, one has to distinguish between molecules that are in so-called low-field-seeking (lfs) or high-field-seeking (hfs) quantum states; as the name suggests, the former are attracted to regions of low electric field whereas the latter experience a force in the direction of a high electric field. In a seminal experiment, performed more than half a century ago, an electrostatic quadrupole focuser was used to couple a beam of ammonia molecules into a microwave cavity. This beam initially contained an almost equal number of molecules in the upper (lfs) and the lower (hfs) inversion states. The radially symmetric electric field in the quadrupole focuser had zero electric field strength on the beam axis, resulting in a focusing (defocusing) of ammonia molecules in the upper (lower) inversion doublet levels. The resulting inverted population distribution in the microwave cavity led to the demonstration of microwave amplification by stimulated emission of radiation, i. e., the invention of the maser, by Gordon, Zeiger and Townes [25].

In this work, the manipulation of beams of large molecules using electric fields is presented. Due to their small rotational constants and the resulting high density of levels, large molecules are hfs in all their low-lying rotational levels already at modest electric field strengths. It must be noted that the ground state of any molecule is hfs as well. Focusing is considerably more complicated for molecules in hfs states than for molecules in lfs states as no electric field maximum can be created on the molecular beam axis using static fields alone.

To focus large molecules, therefore, dynamic focusing has to be applied [26], much like that which is routinely done to transport charged particles [27]. The dynamic focusing of neutral polar molecules has first been experimentally demonstrated on ammonia molecules in hfs quantum states by implementing the alternating-gradient (AG)

---

<sup>1</sup>Interestingly, Reiche and Kallmann were both working at the Kaiser Wilhelm-Institut für physikalische Chemie und Elektrochemie in Berlin, the predecessor to the present Fritz-Haber-Institute. Almost 90 years after the proposal, such a deflector has been built at the Fritz-Haber-Institute to prepare quantum-state selected samples of large molecules [16].

---

focusing technique [28]. More recently, it has also been applied in the deceleration of metastable CO [29], in the trapping of ND<sub>3</sub> molecules [30], in the guiding of a cold beam of molecules from an effusive source [31], and in the transport of CaF [7]. Dynamic focusing has also been applied to large molecules, e. g., in the deceleration of benzonitrile [32] as well as in the separation of two different conformational structures of 3-aminophenol (C<sub>6</sub>H<sub>7</sub>NO) [33]. In the latter experiment the ac electric quadrupole guide was used to selectively transmit molecules depending on their mass-to-dipole-moment ( $m/\mu$ ) ratio, analogous to the transmission of ions with a certain mass-to-charge ( $m/q$ ) ratio in a quadrupole mass filter. The technique is based on two static electric-field geometries that are rotated relative to each other by 90°, both of which lead to focusing of molecules in one transverse direction and to defocusing in the perpendicular direction. By alternating between the two configurations at a suitable frequency, an overall focusing of the beam can be achieved. Successful applications of the AG focusing scheme for ions include the 2D-confinement in quadrupole mass filters [34, 35] and the 3D-confinement in Paul traps [36].

In this work, two newly set-up, second-generation devices are described, implementing AG focusing to manipulate molecules in hfs quantum states: a focuser and a decelerator. To characterize the two devices, pulsed beams of rotationally cold benzonitrile (C<sub>6</sub>H<sub>5</sub>CN) molecules are used, and the arrival time distribution as well as the transverse velocity distribution of the molecules exiting the devices are measured using high-resolution electronic spectroscopy. The resolution of the laser system is sufficiently high that molecules in individual rotational quantum states can be probed selectively. This is important for characterization, because the interaction with the electric fields is highly quantum-state specific. The operation characteristics of the devices are compared to the outcome of numerical trajectory simulations.

The focuser is a successor to the quadrupole guide mentioned above [37]. Because the device selectively transmits molecular species with different  $m/\mu$ -ratios, it is not only a focuser, but it can also be considered a selector and shall be referred to as such hereafter. Compared to the previous generation, the selector is scaled up by a factor of 1.5. The increased electrode distance results in a larger spatial acceptance and the longer electrodes allow for a longer interaction time of the molecular beam with the electric fields. In Chapter 5, the dependence of the transmission through the selector and the  $\mu/\Delta\mu$ -resolution on the applied ac waveforms is studied and the transmission of selected subsets of rotational levels is demonstrated.

Using the previous selector, selective transmission was demonstrated for two conformers of 3-aminophenol with electric dipole moments differing by a factor of 3. By applying asymmetric waveforms to the present selector, transmission can be restricted to benzonitrile molecules in their ground state where their effective dipole moment in the electric fields is only about 5% higher than the dipole moment of the closest lying state. This high resolution is attributed to a novel magnetic holding scheme that results in a substantially, about one order of magnitude, increased accuracy of the mechanical alignment.

In these experiments, the transmission of benzonitrile molecules with different dipole moments is studied. In Chapter 6, the transmission of benzonitrile (103 amu) and the

benzonitrile-argon van der Waals complex (143 amu) is compared. The permanent electric dipole moment of the benzonitrile monomer is expected not to change significantly upon the attachment of the argon atom, because the parent molecular structure remains unchanged [38]. Therefore, transmission is studied for species with (nearly) identical dipole moments but different masses. From comparison with trajectory simulations it is indeed seen that the magnitude and the orientation of the dipole moment relative to the benzonitrile molecule are preserved. Furthermore, the relative densities of the two species in the beam are deduced and it is discussed how transmission can be restricted to either one of the two species alone.

The second device implementing AG focusing is an AG decelerator (Chapter 7) with which not only transverse focusing can be achieved, but also the longitudinal motion of polar molecules can be controlled. This is realized using a series of pulsed inhomogeneous fields, similar to the working principle of the so-called Stark-decelerator [39]. For small, lfs molecules freely adjustable beam velocities have been demonstrated [40–43]. There is great interest in the application of the Stark-deceleration technique to larger, heavier molecules such as bio-molecules or YbF. The latter, for example, is studied by Tarbutt *et al.* to measure the permanent electric dipole moment of the electron which is a test for physics beyond the standard model [14, 44]. A largely enhanced sensitivity is expected from decelerated and subsequently trapped molecules compared to molecules in a molecular beam. To apply the Stark-deceleration technique to hfs molecules, a revised electric-field geometry is required for transverse focusing. Deceleration using such an AG deceleration scheme has been demonstrated for diatomic molecules in hfs states, e. g., CO [29] and OH [45], and for the deceleration of large molecules, e. g., YbF [46] and benzonitrile [32]. In all these experiments the inhomogeneous electric fields at the ends of the high-voltage electrodes are exploited. Hfs molecules are decelerated by turning the high voltages on when the molecules are inside a deceleration stage and switching off after they exited the stage.

The design of the present decelerator is revised from the first generation used in references [32, 45].<sup>2</sup> The number of deceleration stages is doubled to 54 and the orientation of the stages, i. e., the focusing directions, are rotated by 90° after every two stages compared to the previous three-stage pattern. Trajectory simulations show that ground-state benzonitrile molecules can be slowed from 320 to 150 m/s using 81 stages, thereby removing 80% of their kinetic energy [47]. With the two-stage pattern, the transmission through the device is predicted to drop to about 12% compared to guiding, greatly enhanced over the 0.05% transmission expected for the three-electrode pattern. From the present, 54-stage decelerator, however, a very low transmission is obtained which is most likely attributed to mechanical misalignments, resulting in distorted electric fields, thereby reducing the number of stable molecular trajectories through the device. Therefore, the accuracy of the electric fields needs to be greatly enhanced in the next generation decelerator to reach beam velocities low enough for the envisioned trapping of hfs molecules.

---

<sup>2</sup>The decelerator has been designed by Henrik Haak and assembled by André van Roij (Radboud University Nijmegen), Kirstin Wohlfart, and Fabian Grätz in the group headed by Jochen Küpper.

# Chapter 2

## Large molecules in electric fields

In this chapter, the theoretical models are detailed that are needed to understand the interaction between asymmetric top molecules and electric fields. First, the rotational energy levels are derived, and the simulation of rotationally resolved electronic fluorescence excitation spectra is explained. Next, the molecular structure and the relevant constants of benzonitrile and the benzonitrile-argon complex are summarized.

### 2.1 Asymmetric-rotor molecules in electric fields

A detailed understanding of the spectroscopic features of large molecules is essential for insight in the rotational-state-specific detection applied in this work. The following description summarizes the approach as described in greater detail, for example, in the books written by Gordy and Cook [48] and Kroto [49]. Molecular spectra are usually first calculated from the molecular energy levels in the absence of any external fields. The interaction between polar molecules and an electric field is governed by the Stark effect, which must be included in the calculations when such an electric field is present.

#### 2.1.1 Rotational energy levels

The eigenstates of a molecule can be calculated from the non-relativistic Schrödinger equation

$$\hat{H}\psi = W\psi \quad (2.1)$$

that connects the Hamiltonian  $\hat{H}$ , the wave function  $\psi$ , and the internal energy  $W$ . In the Born-Oppenheimer approximation the motion of the nuclei and the electrons of a molecule are decoupled [50]. Therefore, the molecular wave function can be expressed as product of the electronic, vibrational, rotational, and nuclear spin wave functions

$$\psi = \psi_{\text{el}}\psi_{\text{vib}}\psi_{\text{rot}}\psi_{\text{ns}} \quad (2.2)$$

and the energy is the sum of the individual energies

$$W = W_{\text{el}} + W_{\text{vib}} + W_{\text{rot}} + W_{\text{ns}}. \quad (2.3)$$

In this work, supersonic molecular beams are used in which low rotational temperatures of about 1 K are typically achieved. At such low temperatures, large molecules are

mostly in their electronic and vibrational ground states ( $S_0 = 0, v = 0$ ) and, therefore, all higher lying electronic and vibrational levels are neglected in the following. However, the population is still spread over many rotational states. The contribution of  $W_{\text{ns}}$  to the total energy is also very small (typically some MHz) and will be neglected as well.

In the following sections, the calculation of field-free rotational energy levels of asymmetric top molecules will be discussed. At first, the molecular bonds are assumed to be rigid. The distortion of molecules in high rotational states due to the centrifugal force is then introduced as a correction to the rigid-rotor Hamiltonian. In an electric field, the Stark interaction needs to be included.

### Rigid-rotor approximation

In the rigid-rotor approximation, three constant moments of inertia,  $I_a, I_b$ , and  $I_c$ , are associated with the principal axes,  $a, b$ , and  $c$ , of the molecule. By definition the principal moments of inertia follow  $I_a < I_b < I_c$  and the rotational constants (in MHz) are

$$A, B, C = \frac{h}{8\pi^2 I_{a,b,c}}. \quad (2.4)$$

Introducing the angular momentum operators associated with the principal axes,  $\hat{J}_{a,b,c}$ , the rotational Hamiltonian becomes

$$\hat{H}_{\text{rot}}^{\text{rigid}} = \frac{4\pi^2}{h} \left( A\hat{J}_a^2 + B\hat{J}_b^2 + C\hat{J}_c^2 \right). \quad (2.5)$$

$\hat{H}_{\text{rot}}$  commutes with  $\hat{J}^2$  and  $\hat{J}_z$  in the laboratory frame.  $J$ , the quantum number of the total angular momentum, and  $M$ , the projection of  $J$  onto the space-fixed  $z$ -axis, remain therefore "good" quantum numbers.  $\hat{H}_{\text{rot}}$ , however, does not commute with the components  $\hat{J}_{a,b,c}$  in the molecular frame. The quantum number  $K$  is the projection of  $J$  onto the symmetric-rotor figure axis. Unlike for symmetric top molecules,  $K$  is not a "good" quantum number for asymmetric top molecules. Instead the  $(2J + 1)$  sublevels for each  $J$  are labeled with the two pseudo quantum numbers  $K_a$  and  $K_c$ . These describe the projection of  $J$  in the limit of prolate ( $B = C$ ) and oblate ( $A = B$ ) symmetric top molecules, respectively. Furthermore, each  $J$ -level is  $(2J + 1)$ -fold degenerate in  $M$ .

The asymmetry of a molecule can be described by Kay's asymmetry parameter  $\kappa$  which is calculated from the rotational constants [48]:

$$\kappa = \frac{2B - A - C}{A - C} \begin{cases} \kappa = -1 \text{ for } B = C \text{ (prolate)} \\ \kappa = +1 \text{ for } A = B \text{ (oblate)} \end{cases}. \quad (2.6)$$

Therefore,  $K_a$  and  $K_c$  are the  $K$  values of the limiting symmetric top energy levels for  $\kappa = -1$  and  $\kappa = 1$ . Benzonitrile is near-prolate, as indicated by its  $\kappa$  value of  $-0.85$ . For the benzonitrile-argon complex  $\kappa = -0.09$ , indicating a much higher asymmetry.

Energy levels of asymmetric top molecules are obtained by solving the Schrödinger equation through numerical diagonalization of the rotational Hamiltonian. The Schrödinger equation cannot be solved directly when  $H_{\text{rot}}$  is set up in the basis of the asymmet-

Symmetry	E	$C_2^a$	$C_2^b$	$C_2^c$	$K_a K_c$
A	1	1	1	1	ee
B <sub>a</sub>	1	1	-1	-1	eo
B <sub>b</sub>	1	-1	1	-1	oo
B <sub>c</sub>	1	-1	-1	1	oe

**Table 2.1:** Character table of the  $V(abc)$  symmetry group – the Four-group. In the right column the symmetry of the asymmetric rotor wavefunctions are given as function of even-/oddness of  $K_a$  and  $K_c$  (e-even, o-odd).

ric top wavefunctions  $|J, K_a, K_c, M\rangle$ , but these can be expressed as linear combination of the symmetric top wavefunctions  $|J, K, M\rangle$ :

$$|J, K_a, K_c, M\rangle = \sum_{J, K, M} a_{JKM} |J, K, M\rangle \quad (2.7)$$

with scalar coefficients  $a_{JKM}$  and

$$|J, K, M\rangle = \left( \frac{2J+1}{8\pi^2} \right)^{1/2} \mathcal{D}_{K, M}^{J*}(\phi, \theta, \chi). \quad (2.8)$$

$\mathcal{D}_{K, M}^{J*}$  are the Wigner rotation matrices expressing the molecular rotation in the laboratory frame through the Euler angles  $\phi, \theta, \chi$  [48]. From the six possible assignments of the principal axes of inertia  $a, b$ , and  $c$  to the molecule-fixed cartesian coordinates  $x, y$ , and  $z$ , representation  $I^\gamma$  is used in this work (see reference 48).

The Hamiltonian belongs to the symmetry group  $V(abc)$  [48], the Four-group, for which the character table is shown in Table 2.1. The Four-group has the symmetry character of the ellipsoid of inertia, that is symmetric with respect to the identity operation  $E$  and under rotation around any of the  $a, b$ , and  $c$  principal axes by  $180^\circ$ , i. e., under the rotation operations  $C_2^a$ ,  $C_2^b$ , and  $C_2^c$ , respectively.

The resulting Hamiltonian is block diagonal in  $J$  and  $M$  and its elements are [51]

$$\begin{aligned} \langle J, K, M | \hat{H}_{\text{rot}}^{\text{rigid}} | J, K, M \rangle &= \frac{B+C}{2} (J(J+1)) - K^2 + AK^2 \\ \langle J, K \pm 2, M | \hat{H}_{\text{rot}}^{\text{rigid}} | J, K, M \rangle &= \frac{B-C}{4} \sqrt{J(J+1) - (K \pm 1)(K \pm 2)} \\ &\quad \times \sqrt{J(J+1) - (K \pm 1)}. \end{aligned} \quad (2.9)$$

## Centrifugal distortion

For real molecules the rigid-rotor approximation can break down, because their structure is not truly rigid as assumed in the previous considerations. Especially in higher rotational states, molecules are subject to the centrifugal force distorting their structure.

As a result, the moments of inertia associated with the principal axes of a molecule, and, therefore, the rotational constants, change. To incorporate these effects, a centrifugal term is added to the rotational Hamiltonian

$$\hat{H}_{\text{rot}} = \hat{H}_{\text{rot}}^{\text{rigid}} + \hat{H}_{\text{rot}}^{\text{centr.dist.}} \quad (2.10)$$

with the matrix elements of  $\hat{H}_{\text{rot}}^{\text{centr.dist.}}$  and correction terms  $\Delta_J$ ,  $\Delta_{JK}$ ,  $\Delta_K$ ,  $\delta_J$ , and  $\delta_K$ , following Watson's A-reduction [52],

$$\langle J, K, M | \hat{H}_{\text{rot}}^{\text{centr.dist.}} | J, K, M \rangle = -\Delta_J J^2 (J+1)^2 - \Delta_{JK} J (J+1) K^2 - \Delta_K K^4 \quad (2.11)$$

$$\begin{aligned} \langle J, K \pm 2, M | \hat{H}_{\text{rot}}^{\text{centr.dist.}} | J, K, M \rangle &= \left( -\delta_J J (J+1) - \frac{\delta_K}{2} ((K \pm 2)^2 + K^2) \right) \\ &\cdot \sqrt{J(J+1) - K(K \pm 1)} \\ &\cdot \sqrt{J(J+1) - (K \pm 1)(K \pm 2)}. \end{aligned} \quad (2.12)$$

### Stark effect

Molecules with a permanent electric dipole moment,  $\vec{\mu}$ , interact with an electric field,  $\vec{E}$ , through the so-called Stark effect. It induces a splitting and shift of the energy levels by mixing closely spaced rotational energy levels of the same symmetry, and with  $\Delta M = 0$  and  $\Delta J = 0, \pm 1$ . The states, which are degenerate in  $M$  in the absence of an electric field, split into  $J+1$  subcomponents which are non-/two-fold degenerate for  $M = 0 / M \neq 0$  and  $M$  remains as the only "good" quantum number.

In the electric field, directed along the space-fixed  $z$ -axis, the field-free rotational Hamiltonian from Equation 2.5 has to be corrected to include the Stark-effect contribution:

$$\hat{H} = \hat{H}_{\text{rot}} + \hat{H}_{\text{Stark}} \quad (2.13)$$

$$\hat{H}_{\text{Stark}} = -\vec{\mu} \cdot \vec{E} = -E \sum_{g=a,b,c} \mu_g \Phi_{zg}. \quad (2.14)$$

Here, the components of  $\vec{E}$  in the laboratory frame are connected to the components of  $\vec{\mu}$  in the molecular frame through the direction cosine matrix elements  $\Phi_{zg}$  [48]. In the basis of the prolate symmetric top wavefunctions  $|J, K, M\rangle$ , the non-zero matrix elements of  $\hat{H}_{\text{Stark}}$  for the  $a$ -axis component of  $\vec{\mu}$ ,  $\mu_a$ , for example, can then be written as

$$\langle J, K, M | \hat{H}_{\text{Stark}}^a | J, K, M \rangle = -\frac{MK}{J(J+1)} \mu_a E \quad (2.15)$$

$$\begin{aligned} \langle J+1, K, M | \hat{H}_{\text{Stark}}^a | J, K, M \rangle &= \langle J, K, M | \hat{H}_{\text{Stark}}^a | J+1, K, M \rangle \\ &= -\frac{\sqrt{(J+1)^2 - K^2} \sqrt{(J+1)^2 - M^2}}{(J+1) \sqrt{(2J+1)(2J+3)}} \mu_a E. \end{aligned} \quad (2.16)$$

### 2.1.2 Numerical calculation of energy levels

From the matrix elements of the rotational Hamiltonian given above, the energy levels of asymmetric top molecules can be calculated as a function of the electric field via numerical diagonalization of the Hamiltonian. In the field-free case, the assignment of the obtained energy levels to the  $J_{K_a K_c} M$  states is straightforward. In an electric field, however, the energetic order of the states can be different from the order without field, because crossings between states belonging to different symmetry groups can occur. To classify the states, the so-called Wang-transformation can be applied to the Hamiltonian before the actual diagonalization is performed. Thereby, the Hamiltonian is split into four submatrices that each aggregate the states belonging to one of the four symmetry species of the Four-group [53]. These submatrices are diagonalized independently and the  $J_{K_a K_c} M$  labels can be correctly assigned to the states. As a side effect, the diagonalization of the smaller matrices takes less computation time compared to the diagonalization of the full Hamiltonian.

Calculated energies as a function of the electric field of benzonitrile molecules in all rotational levels (of the electronic and vibrational ground state) with  $J \leq 4$  are shown Figure 2.1. The calculation is performed using the home-built software package *libcoldmol* [54] and, as for all calculated energies in this work, the basis set for benzonitrile includes all rotational states with  $J \leq 25$  (for the complex the basis set includes  $J \leq 30$ ). The electric field strength is varied from 0 kV/cm to 200 kV/cm in steps of 0.5 kV/cm.

For each  $J_{K_a K_c} M$ -state, the energy as a function of the electric field strength is stored in a text file, which is then used for the trajectory calculations using the *libcoldmol* program (see Subsection 3.2.2).

### 2.1.3 Transitions and excitation spectra

The electric dipole transitions of an asymmetric rotor molecule from the initial state  $J$  to the final state  $J'$  obey the selection rule  $\Delta J = J' - J = -1, 0, \text{ or } +1$  [48]. The corresponding transitions are called the P, Q, and R branch, respectively. If the electric dipole transition moment is oriented along the principal  $a$ -axis in the body frame, the transition is called  $a$ -type and accordingly  $b$ - and  $c$ -type when the transition moment is oriented along the other axes. Usually, the dipole transition moment is not oriented along one principal axis and the transitions are of mixed type, given by the magnitudes of the projections of the transition dipole moment onto the  $a$ ,  $b$ , and  $c$  axes. Additional selection rules for  $K_a$  and  $K_c$  are summarized in Table 2.2.

The line positions in an electronic fluorescence excitation spectrum are obtained from the energy difference between the initial and final rotational states. Several contributions to the relative transition intensities have to be considered in order to calculate the experimentally observed line strengths. The strength of a rotational transition in an excitation spectrum,  $I$ , depends on several factors:

$$I = I_0 \cdot (2J + 1) \cdot N(T_{\text{rot}}) \cdot g_{ns}. \quad (2.17)$$

Here,  $I_0$  is a constant that includes, among other contributions, the vibrational and

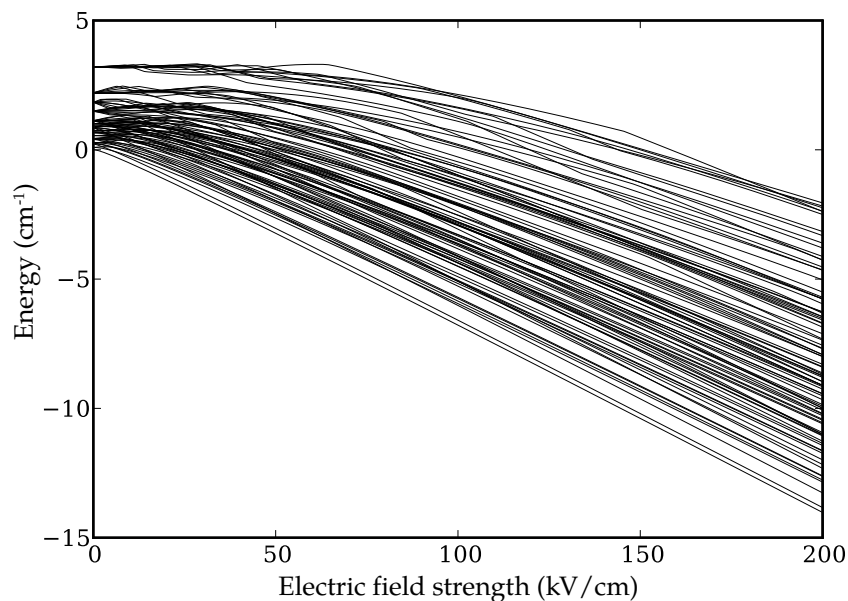


**Figure 2.1:** Calculated Stark curves of benzonitrile molecules in rotational states with  $J \leq 4$ .

Transition type	Allowed transitions	Selection rules
a-type	$eo \leftrightarrow eo$	$\Delta K_a = 0 (\pm 2, \pm 4, \dots)$
	$oe \leftrightarrow oo$	$\Delta K_c = \pm 1 (\pm 3, \pm 5 \dots)$
b-type	$ee \leftrightarrow oo$	$\Delta K_a = \pm 1 (\pm 3, \pm 5 \dots)$
	$oe \leftrightarrow eo$	$\Delta K_c = \pm 1 (\pm 3, \pm 5 \dots)$
c-type	$ee \leftrightarrow eo$	$\Delta K_a = \pm 1 (\pm 3, \pm 5 \dots)$
	$eo \leftrightarrow oo$	$\Delta K_c = 0 (\pm 2, \pm 4, \dots)$

**Table 2.2:** Dipole transition selection rules for asymmetric top molecules (in addition to  $\Delta J = 0, \pm 1$ ). Middle column: even- and oddness of  $K_a$  and  $K_c$  (e-even, o-odd). Right column: Transitions in parenthesis are weaker than the main transitions that are listed first.

rotational contributions to the electronic transition strength, and the square of the matrix element of the electronic transition dipole moment. In the field-free case, each  $J$  level is degenerate in  $M$  and weighted by its  $(2J + 1)$  sub levels. The population of initial  $|J, K_a, K_c, M\rangle$ -states is proportional to the Boltzmann factor:

$$N(T_{\text{rot}}) = e^{-E/kT_{\text{rot}}} \quad (2.18)$$

with the rotational temperature,  $T_{\text{rot}}$ , the state's energy relative to the ground energy,  $E$ , and the Boltzmann constant,  $k$ .

The relative population of rotational levels is additionally influenced by nuclear spin statistics, expressed through the weights  $g_{\text{ns}}$  [49]. A permutation operation, that interchanges the positions of two identical and symmetry-equivalent nuclei in a molecule, must commute with the Hamiltonian. Only then physical observables do not change upon the exchange. By interchanging two fermions, the sign of the wave function is changed, while it remains unchanged under the exchange of two bosons. Therefore, for an even (odd) number of permutations of identical fermions, the total wave function, as shown in Equation 2.2, must be symmetric (antisymmetric) whereas it will always be symmetric for any number of permutations of bosons.

When an asymmetric rotor has at least  $C_2$  symmetry, its total wave function must be antisymmetric with respect to the exchange of a pair of identical protons, i. e., fermions with spin 1/2. Benzonitrile has two such pairs of identical protons with  $C_{2v}$  symmetry as shown in Figure 2.2, which are labeled with numbers 1,5 and 2,4. The symmetry of the wave function depends on the evenness and oddness of  $K_a$  and  $K_c$  [55]. Values of  $g_{\text{ns}}(ee, eo) = 5$  and  $g_{\text{ns}}(oe, oo) = 3$  are calculated for benzonitrile (e=even, o=odd) [38]. The benzonitrile-argon complex is unaffected by these considerations as it has a symmetry lower than  $C_2$ .

## 2.2 Molecular properties of benzonitrile and the benzonitrile-argon complex

Both benzonitrile and the argon complex were subject to a range of studies because they are model systems for aromatic molecules. The most important molecular constants are summarized in Table 2.3. Using Fourier transform microwave spectroscopy, Wohlfart *et al.* and Dahmen *et al.* studied the properties of the electronic ground states [56, 57]. High-resolution fluorescence excitation spectroscopy was performed by Borst *et al.* and Meerts *et al.* to obtain the rotational constants of the first electronically excited state [57, 58]. From the spectra the positions of the atoms in the molecules were calculated and a visualization is shown in Figure 2.2. From calculations based on their spectra Dahmen *et al.* concluded that the argon atom in the complex is placed 3.6 Å above the ring plane, slightly shifted from the ring center towards the nitrile group. Helm *et al.* observed that, in the electronic  $S_1$  state, the argon atom approaches the ring plane by about 0.06 Å and the nitrile group by about 0.08 Å [38, 59].

As the argon atom is placed outside the benzonitrile plane, the center of mass is shifted out-of-plane as well in the direction of the argon atom. Due to the altered mass

	benzonitrile	vdW complex
$m$ (amu)	103	143
$\nu_0$ ( $\text{cm}^{-1}$ )	$36512.74^b$	$36489.0^e$
$\mu$ (D)	$4.52^a$	$4.52^*$
$(\mu_A, \mu_B, \mu_C)$ (D)	$(1,0,0) \cdot \mu$	$(0.22,0.98,0) \cdot \mu$
A (MHz)	$5655.27^a$	$1347.79^c$
B (MHz)	$1546.88^a$	$1006.02^c$
C (MHz)	$1214.40^a$	$719.88^c$
A' (MHz)	$5474.7^b$	$1314.71^d$
B' (MHz)	$1510.2^b$	$1026.16^d$
C' (MHz)	$1183.9^b$	$725.65^d$

**Table 2.3:** Selected molecular constants of benzonitrile and the benzonitrile-argon complex.  $m$  is the mass,  $\nu_0$  is the band origin of the  $S_1 \leftarrow S_0$  transition.  $\mu$  is the electric dipole moment with its components  $\mu_{A,B,C}$ , A,B,C are the rotational constants. <sup>\*</sup>[60], <sup>a</sup>[56], <sup>b</sup>[57], <sup>c</sup>[61], <sup>d</sup>[58], <sup>e</sup>[38]

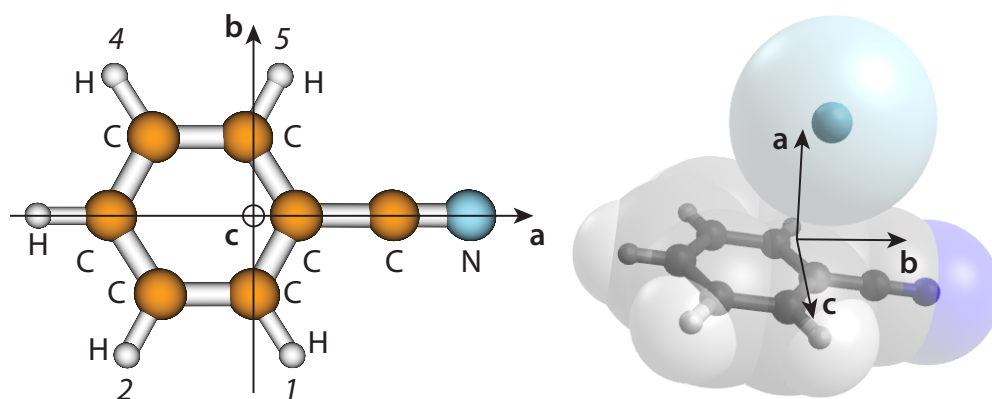


**Figure 2.2:** Molecular structure of benzonitrile (left, adapted from reference 47) and the benzonitrile-argon van der Waals complex (right). Van der Waals spheres are drawn around the atoms of the complex as an illustration.

distribution the roles of the principal axes change from A,B,C for the monomer to B,C,A in the complex and the B axis of the complex is tilted from the monomer's A axis by  $12.8^\circ$  towards the argon atom [38].

The fluorescence excitation spectrum of the benzonitrile monomer shows a typical b-type structure with a missing Q-branch. The direction of the transition dipole moment is maintained in the complex but, due to the changed role of the principal axes, it is mainly oriented along the *c*-axis [58]. This is reflected in the excitation spectrum of the complex that has a c-type structure with a strong Q-branch between the P- and R-branches. The density of lines is much lower in the P- and R-branches than in the Q-branch where many lines overlap.

Given the rotational temperature, the population of the rotational levels in the electronic ground state can be calculated from the Boltzmann distribution. The population as a function of the quantum number  $J$  is shown Figure 2.3 for three different temperatures. (Calculations were performed using the *Pgopher* program [62].) A rotational temperature of 1.8 K (1.2 K) is seen in the molecular beam when the nozzle is heated (not heated) and the curve for a temperature of 0.5 K is included for comparison. The total population, i. e., the sum for all values of  $J$ , is normalized to 1. At the same rotational temperature, the maximum population for the complex is seen at higher  $J$ -values than for benzonitrile, because the complex has a higher density of states.

The electric dipole moment of the complex has not been studied previously. However, the atom positions inside the benzonitrile monomer do not change upon the attachment of the argon atom. Therefore, the dipole moment of the complex is expected not to change from that of benzonitrile, an assumption strengthened by the observed transmission characteristics of the selector for the monomer and the complex shown in Chapter 6.

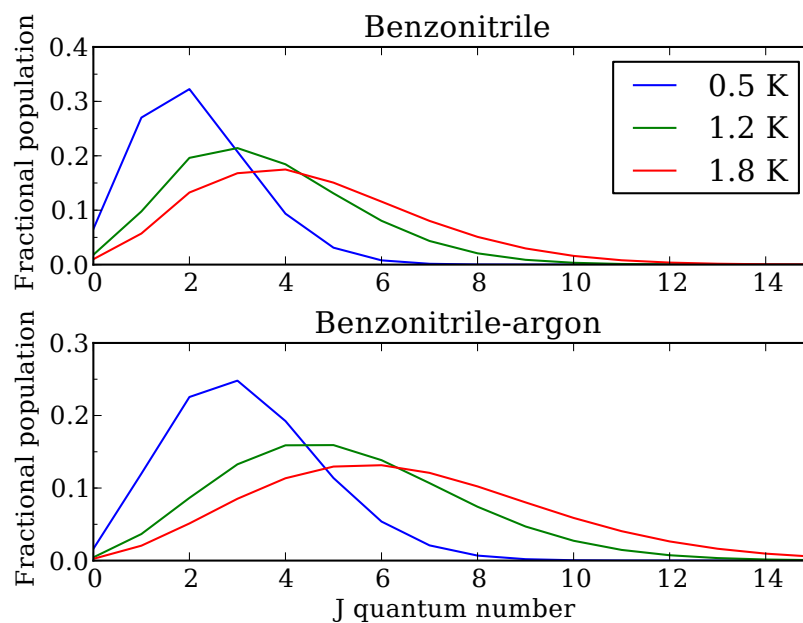


**Figure 2.3:** Fractional population of rotational states in the  $S_0$  electronic level as a function of the quantum number  $J$  and rotational temperature. At the same rotational temperature, the population of the benzonitrile-argon complex is spread over more states than for benzonitrile.

# Chapter 3

## Alternating-gradient focusing

In this chapter, the theory of the alternating-gradient (AG) focusing technique is introduced which is used to focus a beam of large molecules in the ac selector. The derivation is largely based on references 63, 64 and, with respect to stability and resolution, on reference 65. The analogy to the quadrupole mass spectrometer for ions is drawn and it is described how the trajectories of molecules through the device can be simulated from the calculated Stark energies and the electric fields. At the end of the chapter it is discussed how AG focusing can be exploited to enable the deceleration of beams of large molecules in the so-called AG decelerator.

### 3.1 General principles of alternating-gradient focusing

In the following, the manipulation of polar molecules using electric fields is described. First, the case of a linear Stark shift is discussed, followed by the more complicated case of asymmetric top Stark energy curves.

Particles can be confined to stable trajectories around a point  $\vec{r} = \vec{r}_0 = 0$  in three dimensional space when a force field  $\vec{F}(\vec{r})$  is applied that vanishes at  $\vec{r}_0$  and that tends to restore the particle towards  $\vec{r}_0$  for small displacements, fulfilling the necessary condition for confinement

$$\vec{\nabla} \vec{F}(\vec{r}) < 0. \quad (3.1)$$

Molecules with Stark energy  $W_{\text{Stark}}(E)$  that are in an inhomogeneous electric field of magnitude  $E$  experience a force

$$\vec{F}(\vec{r}) = -\vec{\nabla} W_{\text{Stark}}(E). \quad (3.2)$$

In the case of a linear Stark shift, the Stark energy can be written as  $W_{\text{Stark}}(E) = -\mu_{\text{eff}}E$ , where the effective dipole moment,  $\mu_{\text{eff}}$ , is defined as

$$\mu_{\text{eff}}(E) = -\frac{\partial W}{\partial E}. \quad (3.3)$$

Auerbach *et al.* [26] showed that the force field, written in components, becomes

$$F_j = \frac{\mu_{\text{eff}}}{E} \sum_{i=1}^3 \left( \frac{\partial \phi}{\partial x_i} \right) \left( \frac{\partial^2 \phi}{\partial x_i \partial x_j} \right) \quad (3.4)$$

and the divergence of the force is

$$\vec{\nabla} \vec{F} = \frac{\mu_{\text{eff}}}{E^3} \sum_{i,j,k=1}^3 \left[ \left( \frac{\partial \phi}{\partial x_k} \right)^2 \left( \frac{\partial^2 \phi}{\partial x_i \partial x_j} \right)^2 - \left( \frac{\partial \phi}{\partial x_k} \right) \left( \frac{\partial \phi}{\partial x_i} \right) \left( \frac{\partial^2 \phi}{\partial x_i \partial x_j} \right) \left( \frac{\partial^2 \phi}{\partial x_k \partial x_j} \right) \right] \quad \text{for } x_i, y_i \in \mathbb{R}. \quad (3.5)$$

From Schwartz's inequality

$$\left( \sum_{i=1}^n x_i y_i \right)^2 \leq \left( \sum_{i=1}^n x_i^2 \right) \left( \sum_{i=1}^n y_i^2 \right) \quad \text{for } x_i, y_i \in \mathbb{R} \quad (3.6)$$

it was concluded that the sum in Equation 3.5 is greater or equal to 0, and, therefore, the sign of the divergence is determined by the sign of the effective dipole moment. As a result, Equation 3.1 is fulfilled for molecules in quantum states with  $\mu_{\text{eff}} < 0$ . In these so-called low-field-seeking (lfs) quantum states, the energy of the molecules increases with the electric field, resulting in a force on the molecule in the direction of lower field. For high-field-seeking (hfs) states the energy decreases with increasing electric field and  $\mu_{\text{eff}} > 0$ . For these states, Equation 3.1 is not fulfilled and focusing and trapping is not achieved easily.

This situation is the same for charged particles that are manipulated, for example, in ion guides, accelerators and storage rings. Stable trajectories for ions with charge  $q$  can not be achieved using static electric fields alone as the divergence of the electric field vanishes in free space:  $\vec{\nabla} \vec{F} = q \vec{\nabla} \vec{E} = 0$ . Under these conditions trapping is not possible, in accordance with Earnshaw's theorem [66].

Trapping can be achieved, however, when dynamic focusing fields are introduced. As an example for the implementation of such a technique Paul traps and quadrupole mass filters for ions shall be mentioned [35, 67]. The working principle and theoretical description of the latter is directly transferable to the selector for neutral polar molecules that is presented in this work (see Subsection 3.1.2). The notable difference between the manipulation of ions and neutral polar molecules is that the effective dipole moment,  $\mu_{\text{eff}}$ , is quantum-state dependent and, moreover, is not necessarily constant in an inhomogeneous electric field as assumed above, whereas the charge of ions does not depend on the internal quantum state nor on the electric field.

### 3.1.1 Electrode geometries

Efficient AG focusing requires a suitable electric field geometry. In the ideal case of a linear Stark shift and harmonic electric field close to the molecular beam axis, an AG lens that focuses molecules in one direction and defocuses them in the perpendicular direction has a harmonic interaction potential and exhibits only minimal aberration effects. In the limit of strong electric fields the Stark shift of large molecules is indeed linear and the effective dipole moment is constant. Then the ideal electric field is harmonic with  $E(x, y) \propto (x^2 - y^2)$ .

Following the approach taken by Kalnins *et al.* in reference 68, the multipole expansion of the electric potential in cylindrical coordinates ( $r = \sqrt{x^2 + y^2}$  and  $\theta = \tan^{-1}(x/y)$ ) can be written as

$$\phi(r, \theta) = \phi_0 \left[ \sum_{n=1}^{\infty} \frac{a_n}{n} \left( \frac{r}{r_0} \right)^n \cos(n\theta) + \sum_{n=1}^{\infty} \frac{b_n}{n} \left( \frac{r}{r_0} \right)^n \sin(n\theta) \right], \quad (3.7)$$

where  $a_n, b_n$  are dimensionless constants, whereas  $r_0, \phi_0$  are characteristic scaling factors for electrode size and applied electric potentials. These are connected through the electric field on the molecular beam axis  $E_0 = (\phi_0/r_0)\sqrt{a_1^2 + b_1^2}$ .

An electric field which is suitable for an AG lens should be non-zero in the origin and symmetric under reflection in the  $x$  and  $y$ -axis. Such a field is obtained when  $\phi$  is symmetric under reflection about the  $x$ -axis and antisymmetric under reflection about the  $y$ -axis. This can be achieved by setting all  $b_n=0$  and keeping only the odd  $a_n$ -terms in Equation 3.7. Furthermore, by truncating higher-order terms in the expansion which are expected to introduce nonlinearities in the focusing force, the potential can be expressed as

$$\phi(x, y) = \phi_0 \left( a_1 \frac{x}{r_0} + a_3 \frac{x^3 - 3xy^2}{3r_0^3} + a_5 \frac{x^5 - 10x^3y^2 + 5xy^4}{5r_0^5} \right). \quad (3.8)$$

The magnitude of the electric field is calculated from  $\phi(x, y)$ :

$$E(x, y) = \sqrt{\left( \frac{\partial \phi}{\partial x} \right)^2 + \left( \frac{\partial \phi}{\partial y} \right)^2}. \quad (3.9)$$

Under the assumptions  $r < r_0$ , i. e., small deviations from the molecular beam axis, and  $a_1 \gg a_3 \gg a_5$ , the electric field can be expanded as a power series in  $a_3$  and  $a_5$ :

$$E(x, y) = E_0 \left( 1 + \frac{a_3}{a_1} \frac{(x^2 - y^2)}{r_0^2} + 2 \left( \left( \frac{a_3}{a_1} \right)^2 - 3 \frac{a_5}{a_1} \right) \frac{x^2 y^2}{r_0^4} + \frac{a_5}{a_1} \frac{(x^4 + y^4)}{r_0^4} + \dots \right). \quad (3.10)$$

The first two terms in the expansion take the desired harmonic form while higher terms lead to focusing aberration effects. The harmonic focusing term, the second term in the expansion, is of order  $a_3/a_1$ . The first three anharmonic terms are of orders  $(a_3/a_1)^2$  and  $a_5/a_1$ . Therefore, in order to achieve minimal aberration effects, an electrode geometry has to be chosen that minimizes  $a_5$  while  $a_3$  is large enough to achieve sufficient focusing and small enough to minimize the aberration [64]. These requirements are fulfilled for cylindrical electrodes with their centers placed on the corners of a square. Values of  $a_3/a_1 = -0.34$  and  $a_5/a_3 = -0.172$  are found from fits of the generated electric field to the multipole expansion when the following geometry is chosen: electrode radius  $R = 2r_0$ , closest distance between opposing electrodes is  $3r_0$  and the closest distance between the surfaces of adjacent electrodes  $0.94r_0$  (see Figure 3.3, for example) [63].

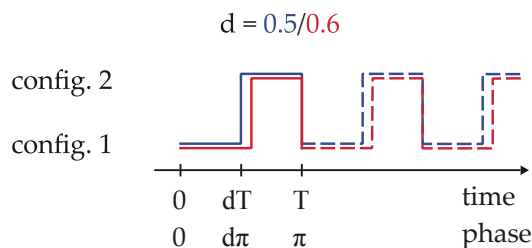


**Figure 3.1:** Time dependence of the applied field configuration. The duty cycle  $d$  is defined as the fraction of the period, of length  $T$  in the time picture or  $\pi$  in the phase picture, during which configuration 1 is applied.

### 3.1.2 Stability and the duty cycle

The working principle of the ac electric selector for neutral molecules is based on selective guiding of molecules with a certain range of  $m/\mu$ -ratios. This resembles the working principle of the quadrupole mass filter (QMF) for ions, which is based on the  $m/q$ -ratio of atoms and molecules with charge  $q$  [34, 35, 69]. The QMF has evolved into a standard tool and compact, efficient devices with very high  $m/q$ -resolution are commercially available. They are used, for example, for analyzing the residual gas in a vacuum or as a mass filter to select atomic or molecular species from a beam. The theoretical description of the QMF includes the application of a bias potential to increase the  $m/q$ -resolution of the device, albeit at the cost of transmission. Here, the transfer of the description to the selector for neutral molecules will be introduced, following the approach in references 65, 70.<sup>1</sup>

In a standard QMF, an oscillating electric quadrupole field is generated by applying a sinusoidal RF voltage  $\Phi$  of amplitude  $V$  and frequency  $\omega$  to the electrodes. By applying a DC voltage  $U$  the  $m/q$ -resolution can be optimized [69]:

$$\Phi = U + V \cos \omega t. \quad (3.11)$$

A square waveform as shown in Figure 3.1 that alternates between two electric field configurations can be used as well. Then the resolution is changed with the duty cycle,  $d$ , as Richards *et al.* pointed out [71, 72]. The duty cycle is defined as fraction of the period of the switching cycle,  $T$ , during which one of the two field configurations is applied, i. e.,  $0 \leq d \leq 1$  (for the ac selector, configuration 1 in Figure 3.3 is taken).

The implementation of this scheme is advantageous over sinusoidal waveforms when using high voltages, because fast high-voltage switches are readily available. The generation of a sinusoidal waveform with an amplitude of 20 kV (peak-to-peak) and variable frequency is non-trivial although it has recently been implemented in our group for the traveling-wave decelerator [13].

Close to the molecular beam axis the electric field generated by the high voltage

<sup>1</sup>The parameters introduced here, which are labeled  $f$  and  $d$ , should not be confused with the parameters with same labels introduced in Section 3.3 in the context of AG deceleration.

electrodes can be approximated as  $E(x,y) = E_0 + \eta(y^2 - x^2)$  by neglecting higher order terms in Equation 3.10 and introducing  $\eta = (E_0 a_3)/(a_1 r_0^2)$ . In a lens that focuses the molecular beam in the  $x$ -direction and defocuses it in the  $y$ -direction, i. e., high-field-seeking molecules in electric field configuration 1 in Figure 3.3, the equations of motion are

$$\begin{aligned} m \frac{\partial^2 x}{\partial t^2} &= -\frac{\partial W_{\text{Stark}}}{\partial x} = -2\mu_{\text{eff}} \eta x \\ m \frac{\partial^2 y}{\partial t^2} &= -\frac{\partial W_{\text{Stark}}}{\partial y} = 2\mu_{\text{eff}} \eta y. \end{aligned} \quad (3.12)$$

We may call the switching frequency of the square wave  $\omega$  and introduce the dimensionless time  $\tau = \omega t/2$ .<sup>2</sup> With these the equations of motion can be written as

$$\frac{d^2 x}{d\tau^2} + \frac{8\mu_{\text{eff}} \eta}{m\omega^2} x = 0 \quad \text{and} \quad \frac{d^2 y}{d\tau^2} - \frac{8\mu_{\text{eff}} \eta}{m\omega^2} y = 0. \quad (3.13)$$

Considering a  $\pi$ -periodic function  $f_u(\tau) = f_u(\tau + \pi)$  in the dimensionless time  $\tau$ , Equation 3.13 takes the form of Hill's differential equation:

$$\frac{d^2 u}{d\tau^2} + f_u(\tau)u(\tau) = 0, \quad u = x, y. \quad (3.14)$$

For a square wave, that consists of subintervals in which  $f_u(\tau)$  is constant, Equation 3.14 can be solved analytically [70]. In a subinterval that corresponds to a focusing lens  $f_u(\tau) = f > 0$  applies whereas in a defocusing lens  $f_u(\tau) = f < 0$ . Then, with the molecule's position  $u_s$  and velocity  $v_s$  at the time  $\tau_s$  when the subinterval begins, the solutions to Equation 3.14 are

$$\begin{aligned} u(t) &= u_s \cos[(\tau - \tau_s)\sqrt{f}] + \frac{v_s}{\sqrt{f}} \sin[(\tau - \tau_s)\sqrt{f}] && \text{for } f > 0 \\ u(t) &= u_s \cosh[(\tau - \tau_s)\sqrt{-f}] + \frac{v_s}{\sqrt{-f}} \sinh[(\tau - \tau_s)\sqrt{-f}] && \text{for } f < 0. \end{aligned} \quad (3.15)$$

Equation 3.15 can be written in matrix form, with the position and velocity of the molecule  $u_0$  and  $v_0$  at the beginning of the first lens, as

$$\begin{pmatrix} u_{n+1} \\ v_{n+1,u} \end{pmatrix} = M_u \begin{pmatrix} u_n \\ v_{n,u} \end{pmatrix} = M_u^{n+1} \begin{pmatrix} u_0 \\ v_{0,u} \end{pmatrix}. \quad (3.16)$$

$M_u$  is the so-called transfer matrix with which the phase-space position of a molecule can be calculated for any time  $\tau$  after the initial time  $\tau_0$  by applying  $M_u$   $n$  times to the initial-state vector, i. e., the initial position at the beginning of the first lens. During the subintervals the  $f$ -function for the  $x$ -coordinate,  $f_x$ , takes the values

<sup>2</sup>The  $m/\mu$ -selector is operated by switching between two field configurations with equal magnitudes of electric field strength. When the voltages applied to the electrodes are different, two parameters  $\eta_1$  and  $-\eta_2$  need to be defined.

$$f_x = \frac{8\mu_{\text{eff}}\eta}{m\omega^2}. \quad (3.17)$$

From Equation 3.13 follows for the  $y$ -coordinate that  $f_y = -f_x$ . The transfer matrices for the  $x$ - and  $y$ -coordinates for a complete switching cycle,  $M_x$  and  $M_y$ , are the products of the transfer matrices of a focusing lens,  $F$ , and a defocusing lens  $D$ . With the durations of the two subintervals  $\Delta_1 = d \cdot \pi$  and  $\Delta_2 = (1 - d) \cdot \pi$ , it follows for a switching cycle starting with focusing in  $x$ -direction and defocusing in  $y$ -direction

$$M_x = D(-f, \Delta_2) \times F(f, \Delta_1) \quad (3.18)$$

$$M_y = F(f, \Delta_2) \times D(-f, \Delta_1). \quad (3.19)$$

For a square waveform, Equation 3.14 can be solved analytically and the transfer matrices  $F$  and  $D$  can be derived. The period length of a lens  $\Delta = \tau_e - \tau_s$ , where  $\tau_s$  and  $\tau_e$  are the times at which the molecule is at the beginning and end of the lens, respectively. It follows

$$F(f, \Delta) = \begin{bmatrix} \cos(\Delta\sqrt{f}) & \frac{1}{\sqrt{f}} \sin(\Delta\sqrt{f}) \\ -\sqrt{f} \sin(\Delta\sqrt{f}) & \cos(\Delta\sqrt{f}) \end{bmatrix} \quad \text{for } f > 0 \quad (3.20)$$

$$D(f, \Delta) = \begin{bmatrix} \cosh(\Delta\sqrt{-f}) & \frac{1}{\sqrt{-f}} \sinh(\Delta\sqrt{-f}) \\ \sqrt{-f} \sinh(\Delta\sqrt{-f}) & \cosh(\Delta\sqrt{-f}) \end{bmatrix} \quad \text{for } f < 0. \quad (3.21)$$

Stable trajectories are obtained for an array of  $n$  lenses when all elements of the transfer matrices remain bounded as  $n$  goes to infinity. This condition is fulfilled for  $|\text{Tr}(M_u)| < 2$  which restricts the possible combinations of the independent parameters  $f$  and  $d$  [73].

The quadrupole mass filter for ions is usually characterized by the parameters  $a$ , related to the dc amplitude, and  $q$ , related to the rf amplitude.  $a$  and  $q$  describe the average force constant over one rf period and the change of the force constant during one period, respectively. As the stability of the equations of motion solely depend on  $a$  and  $q$  the stability can be visualized by drawing ( $a$ - $q$ )-maps [34, 67]. Such maps can also be drawn for the  $m/\mu$ -selector when  $a$  and  $q$  parameters are introduced as follows:

$$\begin{aligned} a &:= a_x = -a_y = (2d - 1)f \\ q &:= q_x = -q_y = 2fd(1 - d). \end{aligned} \quad (3.22)$$

With  $a$ ,  $q$  defined this way the transfer matrices can be written as

$$\begin{aligned} M_x &= D\left(a - \frac{q}{1-d}, \Delta_2\right) \times F\left(a + \frac{q}{d}, \Delta_1\right) \\ M_y &= F\left(-a + \frac{q}{1-d}, \Delta_2\right) \times D\left(-a - \frac{q}{d}, \Delta_1\right). \end{aligned} \quad (3.23)$$

The panels on the left side of Figure 3.2 show  $(a-q)$ -maps for the two duty cycles  $d = 0.5, 0.4$ . In the maps regions of stable trajectories are indicated for the  $x$ -coordinate (dark grey) and the  $y$ -coordinate (light grey). They are obtained for each point on the  $a-q$ -surface by evaluating the condition  $|\text{Tr}(M_u)| < 2$  for the traces of the two transfer matrices as a function of  $a$ ,  $q$ , and  $d$ . The region in which the motion is stable in both the  $x$  and  $y$ -coordinates is drawn in black. Red lines indicate the work lines, i. e., lines that connect the points in the parameter space as the ac frequency is scanned. The stable regions for the  $x$  and  $y$ -coordinates in the maps are point symmetric with respect to the origin and for  $d = 0.5$  they are symmetric with respect to a reflection across the  $q = 0$  line.

A work line goes through the origin and its slope  $s$  is only a function of the duty cycle.

$$s = \frac{2d - 1}{2d(1 - d)}. \quad (3.24)$$

For constant values of  $\omega$ ,  $d$ , and  $\eta$ , each  $m/\mu_{\text{eff}}$  value is connected to a specific point  $(a, q)$  in the stability diagram. It is seen from the map drawn for  $d = 0.5$  that the work line is inside the region of stable motion from  $q = 0$  up to 0.715. When the duty cycle is changed to  $d = 0.4$ , the work line crosses the stable region only in a small region between  $q = 0.5$  and 0.6. In this case, the range of  $m/\mu_{\text{eff}}$  ratios which are transmitted is reduced. When the magnitude of the applied voltages is the same in both focusing and defocusing lenses, e. g., for the present  $m/\mu$ -selector,  $a$  and  $q$  can not be varied independently. In this case, in order to describe the device's stability with only one diagram for all duty cycles, it is more convenient to draw the regions of stable motion onto a  $(f-d)$ -map as shown in the right panel of Figure 3.2. There, the stable regions of the  $x$  and  $y$ -coordinate are symmetric with respect to each other across the  $d = 0.5$  line and the work lines, i. e., the points sampled during an ac frequency scan, are vertical lines. As expected the largest range of stable conditions is seen for  $d = 0.5$  as the work line lies in the stable region up to  $f = 1.4$ . It is seen from the width of the stable region along the  $d$ -axis that stable conditions exist for  $0.38 < d < 0.62$ .

## 3.2 Numerically simulating the ac electric quadrupole selector

In this section, the numerical description of the quadrupole selector is discussed that has been set up in this work. It is detailed how the selector can be described using the *libcoldmol* computer program. In principle, the AG decelerator is described in the same way and specific details are given in Section 3.3.

### 3.2.1 Numerical simulation of the electric field

Electric field configurations suitable for the implementation of an ac electric quadrupole selector are discussed in reference 63. The ideal field geometry is obtained using hyperbolically shaped electrodes, but such electrodes are challenging to build given the requirements of high electric field strength and precise mechanical alignment. A practical

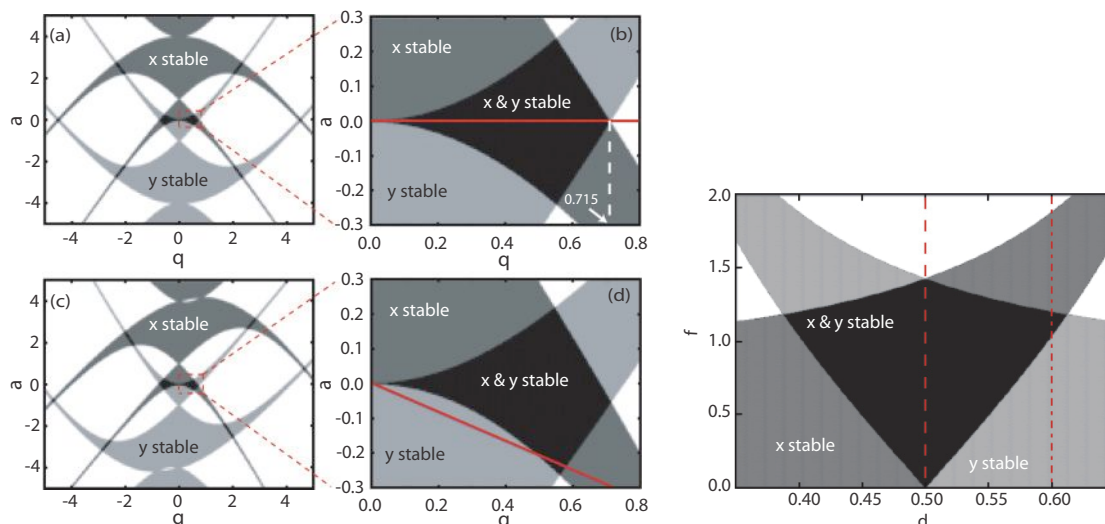


**Figure 3.2:** Left side:  $(a-q)$ -maps for  $d = 0.5$  (top) and  $d = 0.4$  (bottom). Middle panels: area close to the origin of the panels on the left side shown on an enlarged scale. Work lines, corresponding to ac frequency scans, are drawn as solid red lines. Right side:  $(f-d)$ -stability diagram; the region of stable motion in both transverse coordinates is shown in black. Work lines in the current operation mode (sweeping the ac frequency) are drawn as red vertical lines. Figure reproduced from reference 65, see text for details.

solution is the approximation of the fields using cylindrical electrodes, but the resulting fields can not be described by exact equations anymore and, therefore, numerical simulations are needed.

In Figure 3.3 the outcome of such a simulation is visualized. It has been conducted with the *Comsol* program package [74] using the finite-element method. Following the design described later in Subsection 4.2.1 four circles represent the electrode surfaces in the  $(x, y)$ -plane. This structure is placed inside a grounded, 100 mm diameter circle and any contribution from the ends of the electrodes in the longitudinal direction is neglected. In the central region around the molecular beam axis a mesh layout is chosen that is fine enough such that the electric field strength and its gradient are smooth functions of  $x$  and  $y$ . The central  $4.5 \text{ mm} \times 4.5 \text{ mm}$  of the electric field norm and its gradient are exported on a grid with a  $100 \mu\text{m}$  spacing and stored in a compressed text file which is used as an input for the trajectory simulations.

The cross-shaped overlay in Figure 3.3 depicts the typical area in the  $(x, y)$ -plane to which benzonitrile molecules stay confined inside the selector. It is obtained from Monte-Carlo trajectory calculations for molecules that reach the end of the selector. A switching frequency of  $3.8 \text{ kHz}$  is taken for the highest transmission and high voltages of  $\pm 9.5 \text{ kV}$  are chosen. The length (in space) of the packet corresponds to a full switching cycle such that molecules reach the end of the electrodes during every possible phase during the switching cycle. The final positions in the  $(x, y)$ -plane of all molecules are plotted together and contour lines are drawn in steps of 10% of the maximum density.

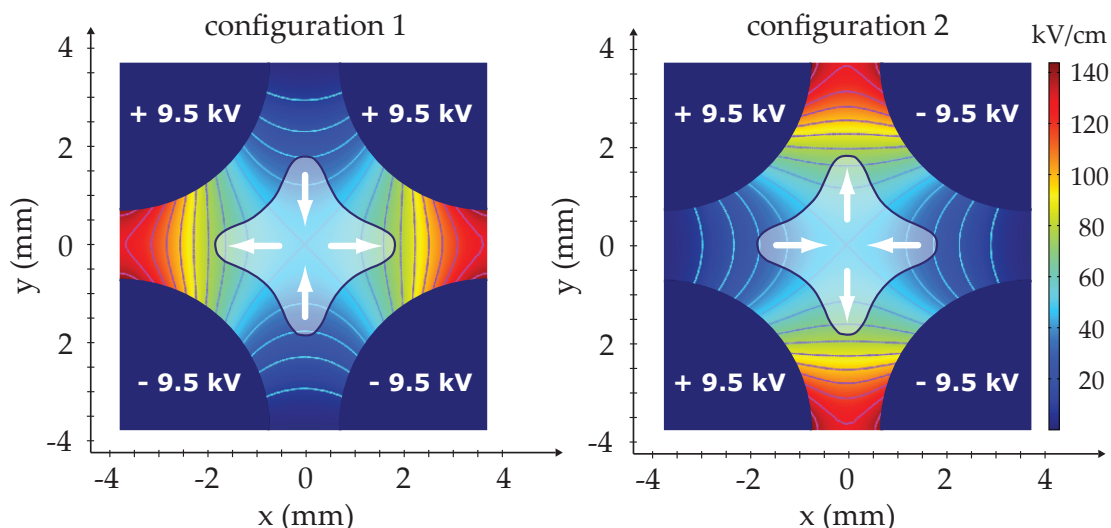


**Figure 3.3:** Numerically simulated electric fields as used in trajectory simulations. The electric field at the center is 48 kV/cm and contour lines are drawn every 10 kV/cm. Arrows indicate the direction of acceleration for molecules in hfs states and the cross-shaped overlay depicts the area to which the transmitted molecules are typically confined. See text for details.

The lines in the two plots in Figure 3.3 are drawn at 10% of the maximum density. Molecules transmitted on stable trajectories, that are confined to within the contour lines, are seen to sample electric field strengths in the range of 25 to 77 kV/cm. At  $\pm 9.5$  kV on the electrodes the field strength on the molecular beam axis is 48 kV/cm.

### 3.2.2 Numerical trajectory simulations

All Monte-Carlo trajectory simulations presented in this work were performed with the home-built *libcoldmol* software package [54]. Using the software, trajectories of molecules through switched electric fields can be calculated.

The simulation involves several steps. First a molecular packet is generated with a seven-dimensional initial phase-space distribution. The actual position of a molecule is defined by a time and three spatial as well as three velocity coordinates and the initial values are chosen from a random distribution, usually Gaussian. The initial time spread of the molecular packet can be expressed as a spatial distribution in the longitudinal  $z$ -direction. In this case, the start time is the same for all molecules and we start with a six-dimensional distribution.

In the next step the selector is modeled.<sup>3</sup> A skimmer is placed at the appropriate position and only molecules that pass through its orifice are allowed to enter the virtual selector, otherwise they are neglected. The selector itself is described by the two 2D field

<sup>3</sup>The *libcoldmol* program is very flexible in implementing different molecular beam machines and several types of decelerators and traps are readily available.

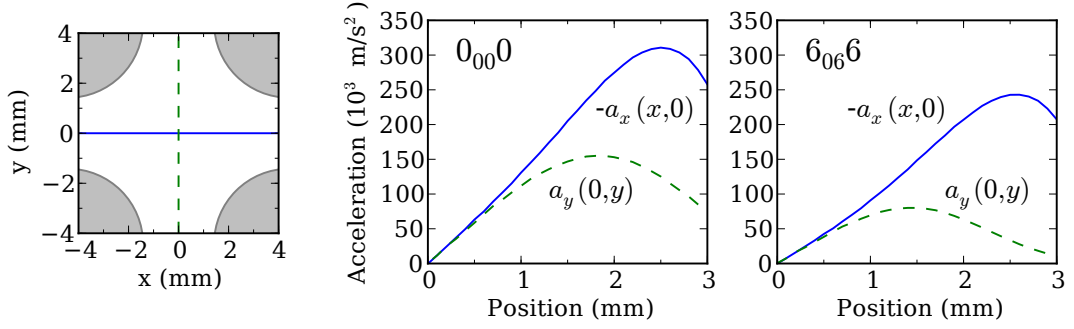


**Figure 3.4:** Left: cut through the electrodes, which are depicted by grey circles, along the  $(x, y)$ -plane. The solid and dashed line represent the  $x$  and  $y$ -axis, respectively. Middle and right panel: Acceleration of benzonitrile molecules in the  $0_{00}0$  and  $6_{06}6$  state along the  $x$  and  $y$ -axis when field configuration 2 is applied (e.g., during a horizontal focusing phase). For illustration the acceleration along the  $x$ -axis is inverted.

configurations shown in Figure 3.3. The actual switching sequences from the experiment are used in the simulation to alternate between the two electric field configurations.

Then an acceleration field is calculated from the Stark energy of a molecule in the desired quantum state in the electric field. The acceleration at a point in space is calculated from the norm of the electric field and its first derivative in combination with the quantum-state specific Stark energies. In Figure 3.4 the resulting transverse accelerations along the  $x$  and  $y$ -axis are illustrated for field configuration 2, e.g., a horizontal focusing phase for hfs molecules (see Figure 3.3). For direct comparison, the acceleration in  $x$ -direction for molecules on the  $x$ -axis is multiplied by  $-1$ . The obtained curves are point symmetric with respect to the origin which is chosen at the molecular beam axis (shown in the left panel). In the middle and right panels the accelerations calculated for the  $0_{00}0$  and  $6_{06}6$  states of benzonitrile are shown. It is seen from the plots that  $a_x = -a_y$  for small displacements from the molecular beam axis. Further away from the beam axis, the defocusing acceleration along the  $y$ -axis is always smaller than the focusing acceleration along the  $x$ -axis.

In order to obtain the trajectories of molecules on their way through the selector the two-dimensional equations of motion are solved numerically using a Runge-Kutta algorithm with adaptive step size. The integration process is stopped when a molecule crosses either a defined maximum  $z$ -coordinate or a maximum integration time. Then, a molecule's final phase-space position is determined by its 7-dimensional coordinate (three spatial coordinates  $\vec{s}_{\text{final}}$ , three velocity components  $\vec{v}_{\text{final}}$  and the final (arrival) time  $t_{\text{final}}$ ). The molecule is translated back from the final coordinate such that its  $z$ -coordinate is the same as that of the intersection point of the laser beam, i. e., where it would be detected in the experiment. This way all translated molecules have the same  $z$ -position but different  $(x, y)$ -values and detection times just as in the experiment. In order to simulate the experimental detection, the time axis is divided into bins with the same length as in the experiment, typically  $20 \mu\text{s}$ , and the weights (explained below) of

all molecules within a bin are summed up to obtain the bin's relative signal. This way a time-of-flight profile is obtained that mimics the time resolved detection.

In order to take other detection effects into account, statistical weights are calculated for each detected molecule before the summation. The following contributions are considered:

- *Natural linewidth:* To model the natural line shape of the induced transition, the velocity distributions along the  $x$ -axis at a given arrival time are convoluted with a Lorentzian profile with a FWHM of 2.2 m/s.
- *Doppler effect / detection laser bandwidth:* The Doppler shift a molecule experiences is determined by its velocity component in the direction of the detection laser beam. When the laser frequency is set to the center of a transition, only molecules with a small Doppler shift can be detected, because the laser bandwidth is very small in the experiment – less than 2 MHz. Typically, only molecules within a 0.5 m/s interval centered around 0 m/s are accepted, unless the natural line width is larger than this (which is the case for benzonitrile).
- *Spatial overlap:* The detection-laser beam is modeled as a cylindrical detection volume that is oriented parallel to the  $x$ -axis. Assuming a flat beam profile, i. e., the laser intensity is homogeneous inside the cylinder, the path length through the cylinder is taken as weight for each molecule. Experimental saturation effects are neglected.

The transmission through the selector is defined as the fraction of molecules initially passing through the skimmer that reach a defined detection region. For better comparison with the experiment the transmission can be given relative to the intensity obtained in free flight. A transmission curve is obtained by calculating the transmission as function of the switching frequency.

### 3.3 Alternating-gradient deceleration

A beam of polar molecules cannot only be focused but also decelerated in inhomogeneous electric fields, for example, in a so-called Stark decelerator. The "regular" type Stark decelerator (in the following referred to as "Stark decelerator" for simplicity) can only decelerate beams of lfs molecules because molecules in hfs states are not transversely focused in this device. By combining the alternating-gradient technique with the Stark deceleration technique, such focusing can be achieved for both lfs and hfs molecules. For example, deceleration of OH molecules in hfs as well as in lfs quantum states has been demonstrated with the predecessor of the present design [45]. The focusing and deceleration parameters introduced in this section are commonly labeled  $f$  and  $d$  and it must be noted that these should not be confused with the parameters introduced in the description of the AG selector in Subsection 3.1.2.

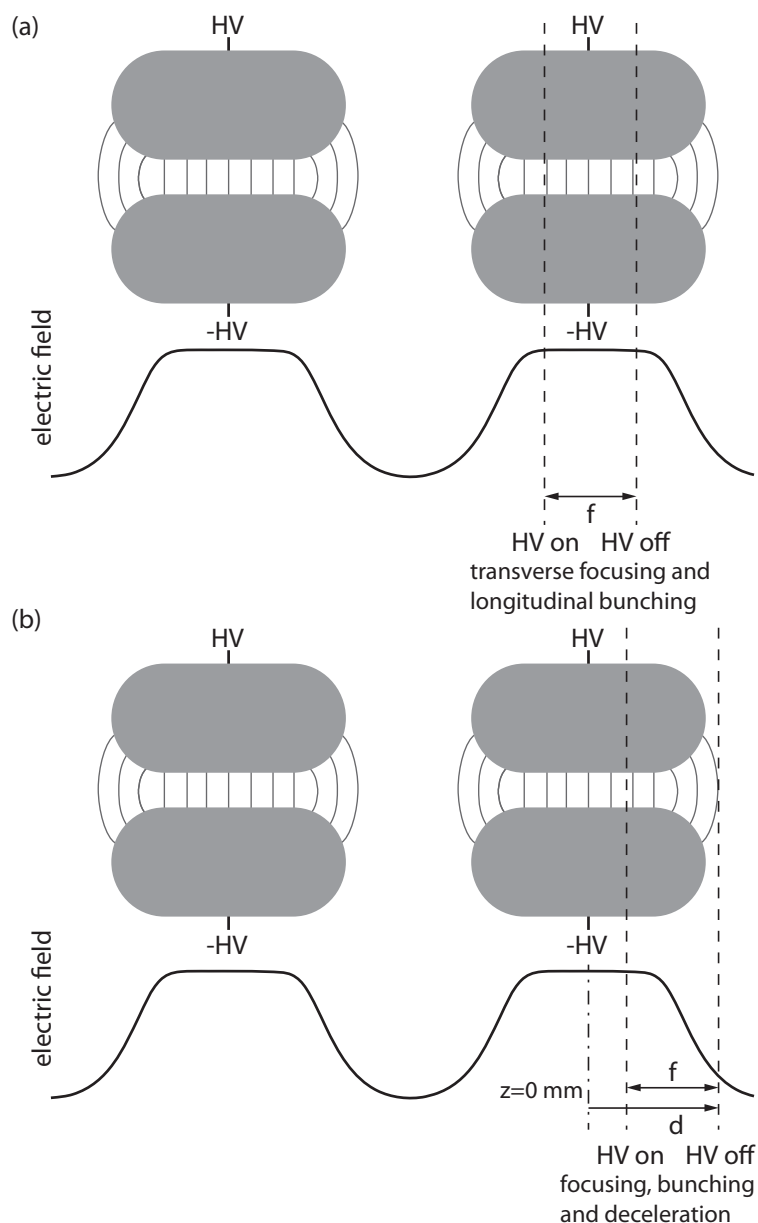


**Figure 3.5:** Schematic depiction of two adjacent electrode pairs and the created electric field along the molecular beam axis in the AG decelerator. Dashed lines indicate the position of the synchronous molecule when the high voltage (HV) is switched on and off in the case of (a) focusing and (b) deceleration.  $f$  is the traveling distance inside the fields and determines the focusing strength,  $d$  is the deceleration parameter that denotes the position at which the deceleration fields are switched off relative to the center of the deceleration stage at  $z=0$  mm.  $f$  and  $d$  should not be confused with the equally labeled parameters defined in Subsection 3.1.2 for the theoretical description of the AG selector. (Figure adapted from reference 47.)

## Working principle

The electric field created on the molecular beam axis of the present AG decelerator is depicted schematically in Figure 3.5. While the field is at a constant maximum near the center of a stage, it is at a minimum in the middle between two deceleration stages. Hfs molecules flying through the device can be decelerated by switching the electric field on when the molecules are inside the constant-field region of a focusing lens. Kinetic energy is removed while the molecules fly out of the stage into the region of lower field, because the hfs molecules feel a force opposing their motion, i. e., in the direction of higher field inside the stage. The final velocity depends on the initial kinetic energy and the difference in potential energy in the electric field the same way as in a Stark decelerator for lfs molecules [39]. As the maximum removable kinetic energy per deceleration stage is relatively small, Stark decelerators are composed of many stages, with their number depending on the desired final velocity and the dipole-moment-to-mass ratio of the molecule. Typically, 100 or more stages are needed to decelerate beams of small molecules from initial velocities on the order of 300 m/s to almost standstill.

To generate the switching sequences applied in the experiment, the flight of a single molecule, the so-called synchronous molecule, through the decelerator is considered. The synchronous molecule is flying along the molecular beam axis, the  $z$ -axis ( $x=y=0$  mm), where it is not subject to transverse accelerations. As indicated in Figure 3.5, the focusing parameter,  $f$ , denotes the distance that the synchronous molecule travels inside the electric field. The deceleration parameter,  $d$ , is the distance from the center of a stage to the position of the synchronous molecule at which the field is switched off.  $f$  and  $d$  define the amount of kinetic energy removed per deceleration stage for a given molecular quantum state. When  $f=2d$  is chosen, i. e., when the field is switched symmetrically around the center of a stage, the AG decelerator is operated in guiding mode in that the mean kinetic energy of the synchronous molecule is not changed. In a real molecular packet, molecules are distributed over a certain longitudinal range and the applied switching sequences are arranged such that the (hypothetical) synchronous molecule is located in the middle of the packet and its moving at the mean velocity of the packet. There is a longitudinal focusing effect (bunching) when guiding at  $f=2d$ , because molecules that fly ahead (behind) of the synchronous molecule are decelerated (accelerated) so that the packet is focused towards its center.

The main difference between the two decelerator types is the transverse focusing of the molecular packet. While lfs molecules are effectively focused to the beam axis in a Stark decelerator, hfs molecules are defocused towards the high fields at the electrodes surface. This defocusing can be compensated by using the saddle potential in the constant-field regions for AG focusing. While, close to the beam axis, the focusing and defocusing forces in the two transverse directions are equally strong inside a deceleration stage, the defocusing force is dominating over the focusing force in the fringe fields in between two adjacent stages. These end effects are discussed in detail for the specific electric fields of the present decelerator in reference 47.

For efficient deceleration, the obtainable electric field gradients along the molecular beam axis are important. In the quadrupole geometry of the ac selector, for example,

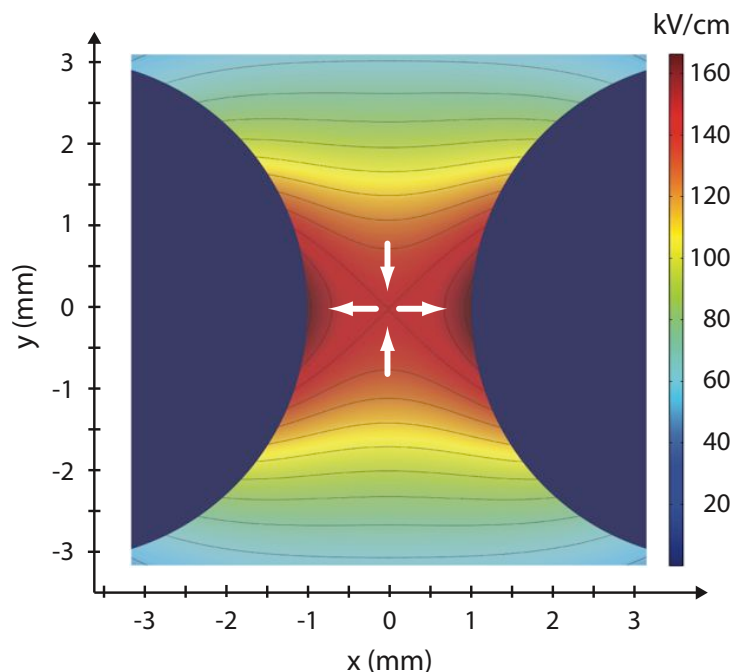


**Figure 3.6:** Numerically simulated electric fields in the middle of an AG deceleration stage. Electrode cross-sections are depicted by blue circles and arrows indicate the direction of acceleration. The electric field at the center is 142.5 kV/cm and contour lines are drawn every 10 kV/cm.

the field strength on the beam axis is only 41% of the maximum field strength [64], but higher fields on the beam axis can be created by choosing an asymmetric electrode geometry. In Figure 3.6, the electric field is shown that is created in the  $(x, y)$ -plane in the middle of a deceleration stage (a quantitative specification of the field is given in reference 47). White arrows indicate the directions of the resulting de-/focusing forces for hfs molecules.

For the AG principle to work, the saddle potentials need to be rotated after a certain time to interchange the de-/focusing directions. Whereas the quadrupole geometry implemented in the selector allows to switch the focusing direction arbitrarily, the period of the focusing lenses in the AG decelerator is fixed because of the gaps introduced in the longitudinal direction. Therefore, the layout of the individual asymmetric lenses needs to be chosen carefully for the considered molecular quantum states. A single lens is used at the beginning of the lens array for an increased transverse acceptance and starting from the second lens the focusing direction is rotated by  $90^\circ$  after every two lenses. The focusing directions in the decelerator can be sufficiently labeled by considering only one transverse direction in that a (de-)focusing lens is called  $F$  ( $D$ ) analogously to the transfer matrices introduced in Equation 3.16. The field-free drift region between two lenses is denoted as  $O$ . Using this nomenclature, the present AG decelerator can be written as an array of lenses:  $(FO)((DO)^2(FO)^2)^{13}(DO)$ .

## Numerical trajectory simulations

Using the *Comsol* program [74], the 3-dimensional electric fields inside the AG decelerator were calculated and subsequently stored in the *libcoldmol* program for trajectory simulations. By taking advantage of the translational and rotational symmetries in the decelerator, only three segments of the electric fields need to be simulated and arbitrary combinations of focusing and defocusing lenses can be arranged in the simulated decelerator. Available are the fields between (a) two adjacent focusing lenses ( $F$ )<sup>2</sup>, (b) between two adjacent focusing and defocusing lenses ( $FD$ ) and (c) the field at the end of a single lens ( $FO$ ), corresponding to the beginning/end of the decelerator. In the  $z$ -direction, each field segment stretches from the center of one stage to the center of the next stage or, i. e., case (c), from the center of a stage for 20 mm into the field-free space.

The switching sequences that are used in the experiments and simulations are generated by simulating the flight of the synchronous molecule introduced in Section 3.3 along the  $z$ -axis of the decelerator. An array of desired  $f$  and  $d$  values for each deceleration stage is passed to the *libcoldmol* program together with the forward velocity. During the simulated flight of the synchronous molecule, the applied field configuration is changed at the appropriate  $z$ -positions defined by the  $f$  and  $d$  values. A visualization of the switching sequences for guiding and deceleration of ground-state benzonitrile molecules at a 385 m/s forward velocity is given in Figure 3.7. Each trace of a pair depicts the trigger signal sent to the HV switches connected to one of the two arrays of deceleration stages which are either focusing or defocusing. High voltages are applied during times the signal is high and ground potential is applied when the signal is low. In the sequence calculated for  $f=8$  mm,  $d=4$  mm, the mean forward velocity of the molecular beam remains unchanged while flying through the decelerator and the pulse width and rate is the same for all pulses. For  $f=8$  mm,  $d=8$  mm, however, the beam is decelerated and the decreasing velocity is considered by increasing the pulse widths and adapting the switching rate as the beam progresses. A final velocity of 220 m/s is predicted from the calculation of the sequence. Due to the lower velocity when decelerating, the beam arrives notably later in the last deceleration stage compared to guiding as can be seen in the visualization. As for the ac selector, the list of switching times is saved in a text file that can be loaded into the *KouDA* program to run the burst unit for triggering the high-voltage switches in the experiment (see Subsection 4.2.2).

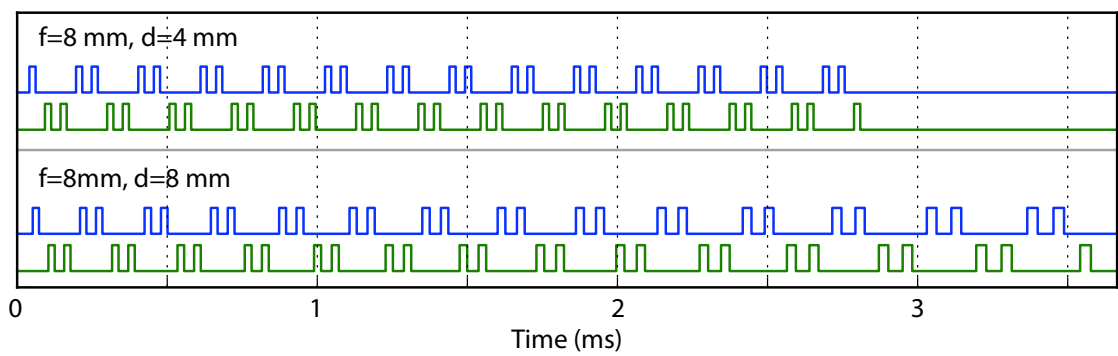


**Figure 3.7:** Visualization of two switching sequences at an initial velocity of 385 m/s. High voltages are applied to the two arrays of AG lenses, corresponding to the blue and green traces, during times the signal is high and ground potentials are applied when the signal is low. A guiding sequence with  $f=8$  mm,  $d=4$  mm is shown in the upper part and a deceleration sequence with  $f=8$  mm,  $d=8$  mm in the lower part.

# Chapter 4

## Setup

This chapter describes the design of the new alternating-gradient (AG) selector for large neutral molecules. The selector, as shown in Figure 4.1, is scaled up relative to its predecessor, which has previously been set-up in our group [33, 63]. By employing a new mechanical construction and an increased overall size, the transmission and selectivity for the dipole-moment-to-mass ratio of the studied molecules is enhanced.

A significant improvement of the mechanical alignment has been achieved by taking special care to reduce the variation of the electrode-to-electrode distances to achievable machine accuracy (about  $\pm 0.02$  mm). Together with the increased electrode spacing, a substantially smaller relative error, about an order of magnitude, in the inter-electrode distance is achieved.

Experimental details are given in the following sections. In brief, a pulsed nozzle is used to produce a molecular beam. Benzonitrile is seeded in argon gas and co-expanded into vacuum, passing through a skimmer placed 40 mm behind the nozzle. At 32 mm downstream from the tip of the skimmer, the beam enters the selector, which consists of four straight, parallel, 1.64 m long electrodes. High voltages are connected to the electrodes. Switches are used to rapidly ( $< 0.5 \mu\text{s}$ ) alternate between two voltage configurations.

The transmitted molecules are monitored behind the end of the  $m/\mu$ -selector via quan-

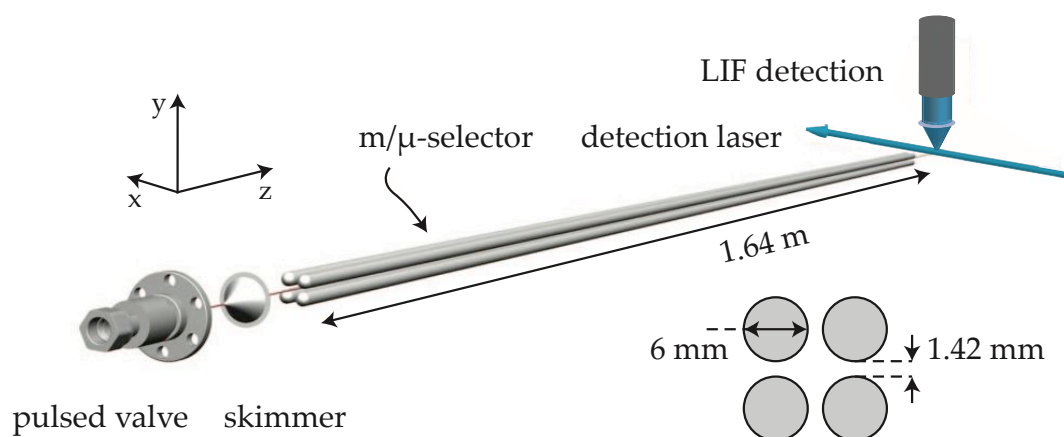


**Figure 4.1:** Schematic view of the experimental setup and a cut through the electrodes along the  $(x, y)$ -plane.

tum state selective laser induced fluorescence (LIF) detection. Narrow bandwidth 274 nm laser radiation from a frequency doubled ring-dye laser is used to excite the vibrationless  $S_1 \leftarrow S_0$  transition at rotational resolution for both the benzonitrile monomer and its van der Waals complex, which is formed with argon atoms from the seed gas. The transmission of molecules in single rotational quantum states is studied as a function of the applied waveforms.

## 4.1 Molecular beam setup

### 4.1.1 Vacuum system

The vacuum system that houses the molecular beam source and the selector, shown in Figure 4.2, has previously been used for the AG decelerator [32, 45]. The system is divided into two main chambers, the source and experimental chambers, each consisting of a 235 mm inner diameter tube with CF 250 flanges at both ends. A home built gate valve [75] separates the two chambers, allowing one chamber to be vented while maintaining high vacuum in the other. A 1.5 mm skimmer (Beam Dynamics, model 2) is mounted directly on the gate valve, forming a differential pumping stage when the gate valve is opened.

The pressure is monitored by pressure gauges (Pfeiffer Vacuum, IKR 270) that are installed on both chambers. Typical base pressures of  $< 10^{-7}$  and  $< 10^{-9}$  mbar are achieved in the source and detection chambers, respectively. When the nozzle is operated under normal conditions at a repetition rate of 40 Hz, these pressures rise to  $< 5 \times 10^{-5}$  mbar and  $2 \times 10^{-7}$  mbar. A turbo molecular drag pump (TMP) (Pfeiffer Vacuum, TMU1601 P, 13801/s) is attached to the source chamber.

The experimental chamber is a combination of a 1.62 m long chamber, in which the selector is placed, and a chamber for the LIF detection zone (see Subsection 4.3.2 for details). Three identical 530 mm long chambers are combined to form the selector chamber with a TMP (Pfeiffer Vacuum, TMU 261 P, 2301/s) attached to each of them. A larger TMP (Pfeiffer Vacuum, TMU 1001 P, 9201/s) is attached to the detection chamber.

Two oil-free piston pumps (Pfeiffer Vacuum, XtraDry 150-2) are used on a fore-vacuum line. They provide a pressure of  $5 \times 10^{-2}$  mbar to the TMPs.

### 4.1.2 Source

In all experiments with pulsed molecular beams presented here, the same pulsed solenoid valve (General Valve, Series 99, orifice 0.8 mm) is used. The seed gas, typically argon, is bubbled through liquid benzonitrile (Fluka,  $\geq 99\%$ , used without further purification) in a heatable container. The exit of the container is connected to the nozzle by stainless steel tubes with an inner diameter of 4 mm. Container and nozzle are mounted on a 3-axis translation stage to allow precise alignment under vacuum conditions in all three spatial directions. A home-built nozzle driver is used to operate the nozzle at a repetition rate of 40 Hz with electrical pulses of 300 V. The pulse duration can be adjusted between 60 and 300  $\mu\text{s}$  by a potentiometer. Typically, the duration of a pulse is set to about 200  $\mu\text{s}$ .

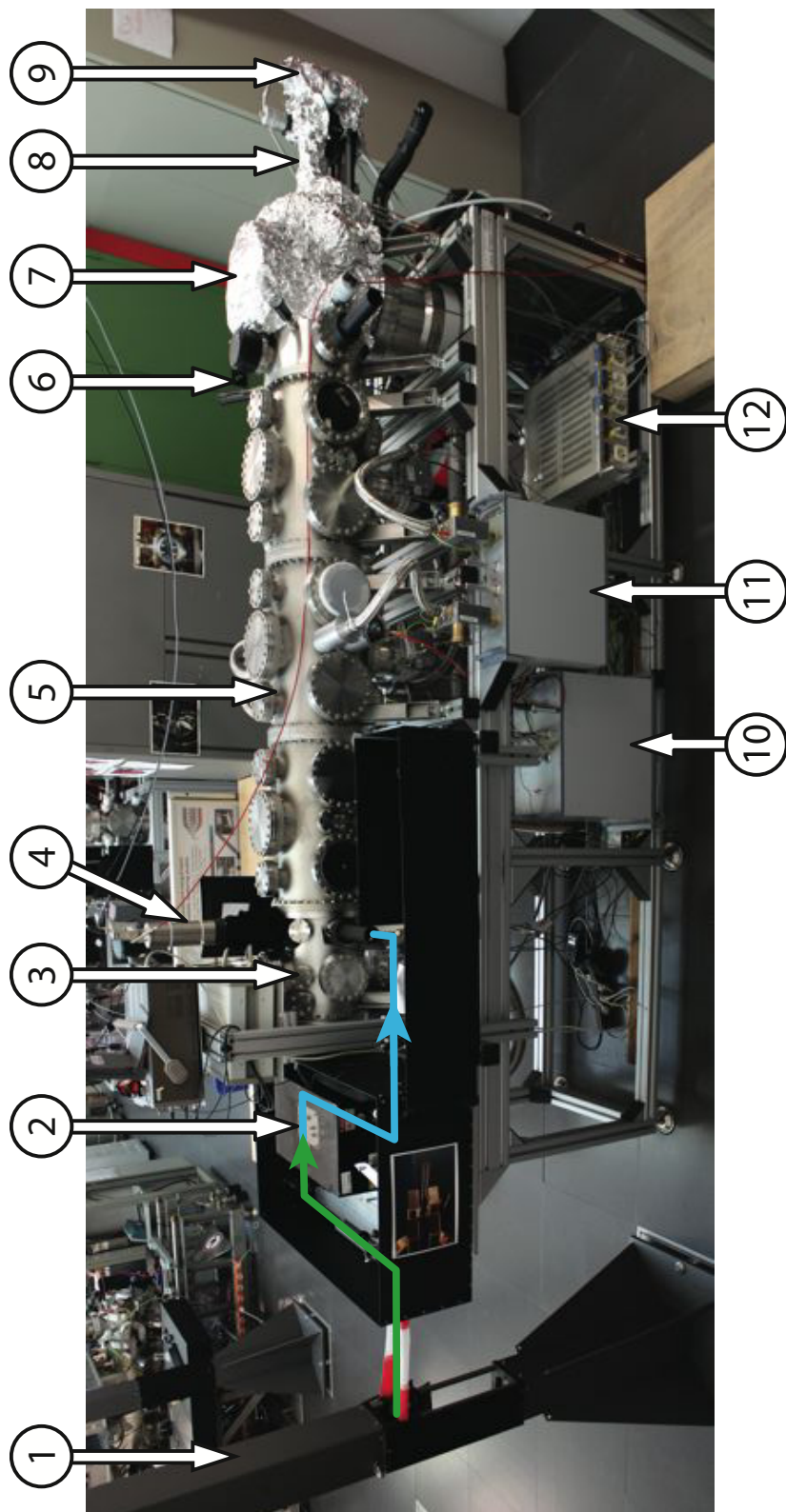


**Figure 4.2:** Photograph of the molecular beam setup. Laser paths are indicated as colored lines. (1) laser periscope, (2) laser-frequency-doubling unit, (3) detection chamber, (4) photo-multiplier tube, (5) selector chamber, (6) gate valve, (7) source chamber, (8) manipulator, (9) benzotrinitrile reservoir, (10) HV capacitor, (11) HV switches, (12) heating controller

By heating nitrogen gas outside the source chamber and letting it flow through a copper block that surrounds the nozzle, temperatures of up to 80 °C can be achieved.

At room-temperature and 2.5 bar argon pressure, the gas mixture contains 0.04% benzonitrile in argon. The resulting beam of benzonitrile molecules has a rotational temperature of about 1 K and a mean forward velocity of around 570 m/s. The value for the most probably velocity is not precisely known but is expected to be close to, but probably slightly higher than, that for a mono-atomic ideal gas expanding from a room-temperature valve [3]; with  $v_p = \sqrt{5k_B T_0/m}$  with  $k_B$  the Boltzmann constant,  $m$  the mass of the Ar atoms and  $T_0=295$  K, a lower limit of  $v_p = 552$  m/s is obtained. For a detailed analysis of the experimental results, the initial length of the gas pulse and the width of the velocity distribution are other important parameters. These are not known independently, but the relative spread in the arrival time distribution at the end of the beam machine can be accurately determined as being 4.8% (see Section 5.1). This is mainly attributed to the width of the velocity distribution, which is assumed to have a full-width-at-half maximum (FWHM) of about 25 m/s, corresponding to a relative velocity spread of about 4.4%; the gas pulse is assumed to have an initial length of about 4 cm, i. e., an initial duration of about 70  $\mu$ s. This narrow velocity distribution corresponds to a longitudinal translational temperature of 0.5–0.6 K.

## 4.2 The ac electric selector

### 4.2.1 Design

The selector consists of four 1.64 m long and 6 mm diameter stainless steel electrodes that are centered at the corners of a square with a diagonal of 10.5 mm and an edge length of 7.42 mm. This implies that the shortest distance of the surface of each of the four electrodes to the molecular beam axis, referred to as the  $z$ -axis, is 2.25 mm. The closest spacing between two adjacent electrodes is 1.42 mm.

The highly polished electrodes (AWU Precision Slovakia) are made of magnetic stainless steel (X90CrMoV18, 1.4112). One electrode consists of two identical 820 mm long pieces that are rounded off at one end, with a radius of curvature of 3 mm, to suppress discharges toward the grounded vacuum chamber and toward adjacent electrodes. Polishing the electrode surfaces is of great importance as a low surface roughness is needed to withstand the applied electric fields. The electrodes are manufactured with a specified surface roughness of  $R_a < 0.1$   $\mu$ m and are subsequently polished by hand with sandpaper of increasing grade up to 4000.

A mounting scheme is employed that ensures that the distance between neighboring electrodes is kept as constant as possible over the full length of the device. Each of the electrodes is attached to one of four 1400 mm long rigid aluminum holders (Pink GmbH), as shown in Figure 4.3. Starting from a long edge of a polished ( $R_a = 0.3$ ) 24  $\times$  50  $\times$  1400 mm cuboid, a tapering extends toward the molecular beam axis, ending in a trough with circular curvature ( $\varnothing$ 6 mm, tolerance H7), which matches the shape of the electrodes (tolerance g6).

Each of the four backbone holders is attached to an aluminum baseplate via two

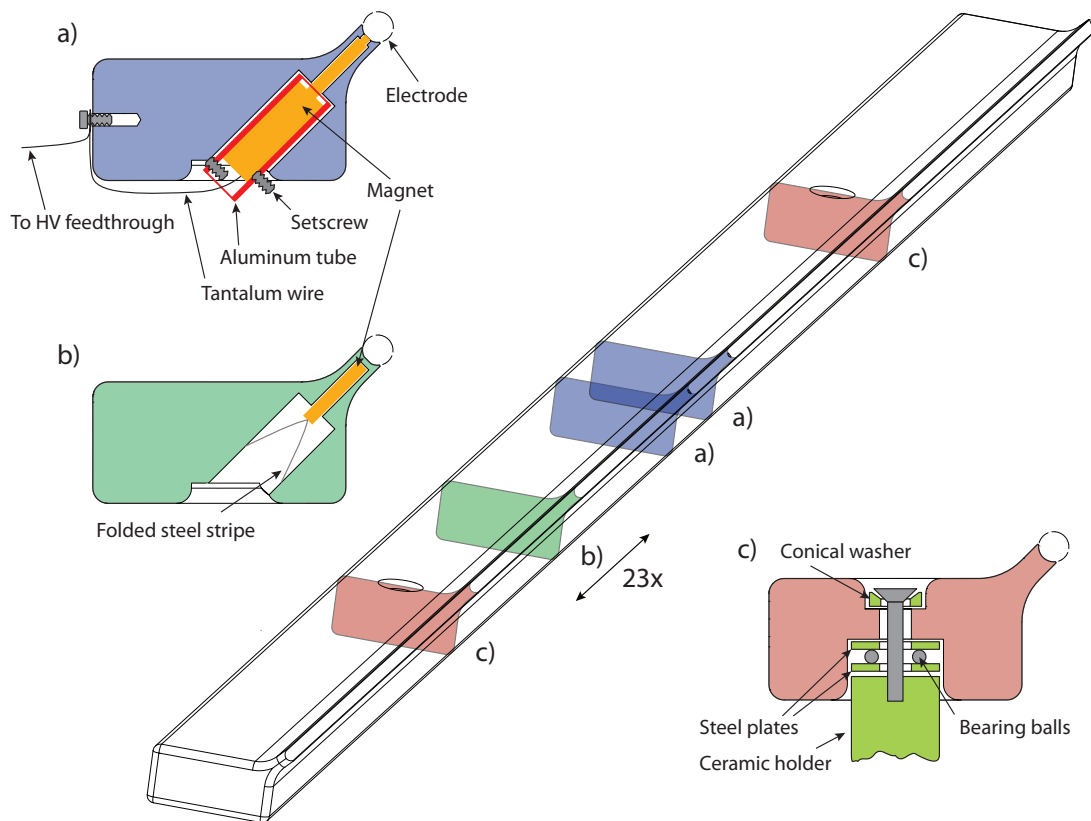


**Figure 4.3:** Drawing of the rigid aluminum holders used as backbones of the electrodes. Three representative cross sections through the holder are shown. a) High-voltage connection to the holder and electrode, b) placement of holding magnets, repeated 23 times over the full length of the holder, c) attachment to a ceramic holder/isolator. The setscrews in a) are used to fix the aluminum tube inside the large hole and to fix the magnet insides the aluminum tube.

ceramic electric isolators as can be seen in Figure 4.4. The isolators are placed 750 mm apart symmetrically around the center of the longest edge of each holder. These subunits, consisting of an electrode, holder, ceramics, and baseplate, are mounted in a rigid outer frame; two subunits are standing, two hanging from above.

Structural simulations were performed using a finite-element method (Unigraphics NX 5) to optimize the length of the aluminum holders for smallest overall bending of the electrodes due to gravity. Rigid connections were defined between electrode and holder as well as between holder and the fixed ceramic isolators. A shorter length leads to less bending of the holder itself, but the free standing part at the ends of the electrodes is longer. Thus the free standing part of the electrodes, which are relatively floppy compared to the holders, are effectively bend further downwards. In the case of longer holders, the additional weight toward the ends of the holders results in increased bending,

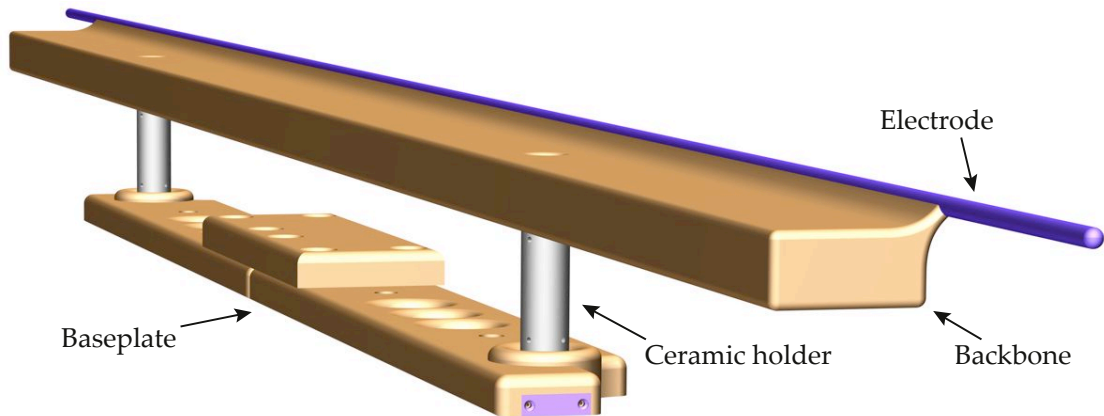


**Figure 4.4:** One of four subunits of the AG selector. Ceramic holders serve as mounts and as electric isolators between the baseplate and the backbone. The cylindrical electrodes are attached to the backbones by small magnets (see Figure 4.3). The individual subunits are aligned inside a rigid holding frame.

while the free standing part of the electrodes is shorter.

In Figure 4.5, the outcome of such a simulation is shown for a 1400 mm long holder, for which the smallest overall displacement at the ends of the electrodes of about 0.02 mm is seen. An exaggerated vertical scale is chosen to visualize the resulting bending together with a false-color representation. In the inset, the maximum bending at the electrode ends is shown for different holder lengths. Corresponding simulations indicate that the absolute bending is equal in both the standing and hanging holder configurations

Special care has been taken to keep the deviation of the trough position from the perfectly straight design to within machine accuracy ( $\pm 0.015$  mm) in the  $x$ - and  $y$ -directions over the full length of the holders. To achieve such high straightness, the machining and polishing of all surfaces has been performed before finally milling the trough surface. The mounting scheme has been accounted for during the manufacturing process by mounting the holders onto standing/ hanging mounts that resemble the ceramics used in the final setup.

When screwing a holder to the two ceramics, the contact surfaces are usually neither perfectly parallel nor perfectly flat. In both cases great mechanical stress is induced. To compensate for this possible imperfection, two mechanical measures are taken. First, small stainless steel bearing balls are inserted between the aluminum holder and the ceramics, one ball onto one ceramic and two onto the other. This way each holder is fixed at three points. Stainless steel disks are placed above and below the balls to avoid compression into the surfaces of the aluminum holder and the titanium caps. Secondly, conical screws and washers are used for the attachment.

The electrodes are inserted into the troughs, and are attached magnetically. This eliminates the unavoidable bending of the electrodes when screw holes are drilled into them and the mechanical stress that would occur when the electrodes are screwed to the holders. From the backside of each holder, 25 holes spaced by 57 mm are drilled toward

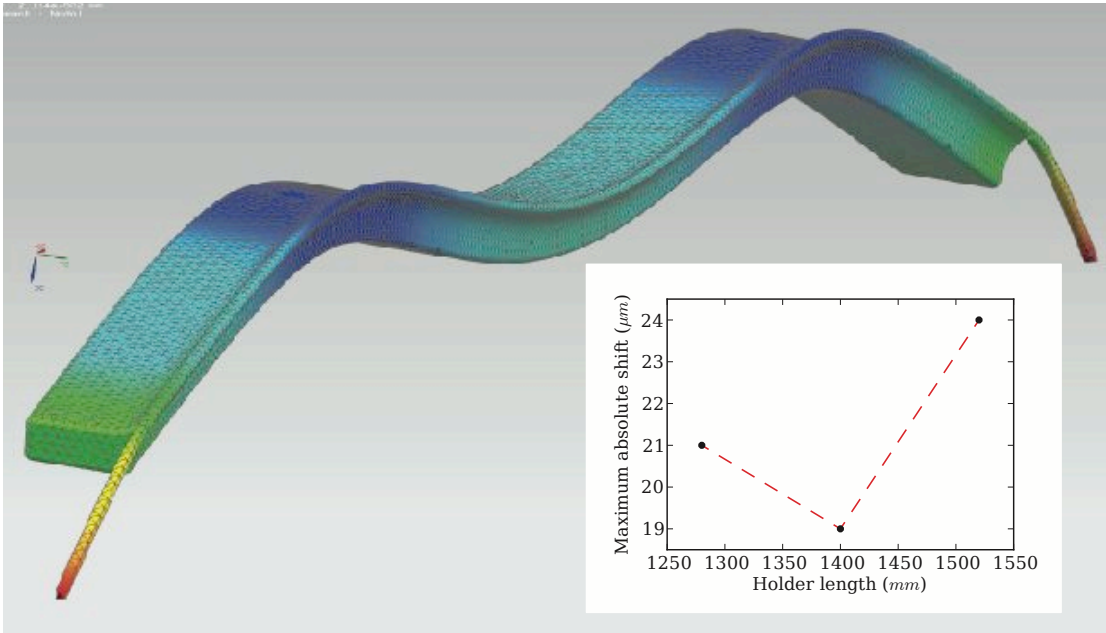


**Figure 4.5:** Simulation of gravitation acting on the model of an 1400 mm long aluminum holder with an electrode rigidly attached (screenshot of the Unigraphics program). The bending in the vertical direction is exaggerated and is also shown in a false color representation that ranges from blue to red to visualize displacements between 0 and 19  $\mu\text{m}$ . The inset shows the maximum absolute shift in the vertical direction obtained from the simulations for 1640 mm long electrodes as a function of the holder length. Dashed lines are used as a guide to the eye.

the troughs. As shown in Figure 4.3 b), the holes are not drilled through, but 0.8 mm of aluminum are left to avoid contact between the electrodes and the small rare-earth magnets ( $\varnothing 3 \times 14 \text{ mm}$ ), which are inserted. Short stainless steel foil strips are pushed into the holes, in order to hold the magnets in place.

In order to connect high voltages to the electrodes, two magnet holes in the middle of each holder are drilled through the surface of the trough as shown in Figure 4.3 a). Both of the magnets inserted there have direct contact to one of the half-electrodes and are connected to the same high-voltage feedthrough using a tantalum wire. To hold them in place, the magnets are fixed inside aluminum tubes. To ensure that the electrode and the aluminum holder have the same electric potential, the wire is also attached to the holder. A similarly enforced attachment is employed at each end of an aluminum holder. There, stainless steel cylinders are glued onto the aluminum surface. Holes in the cylinders point toward the electrodes. A magnet is inserted such that it directly contacts the electrode surface and a setscrew is used to hold the magnet in place inside the steel cylinder.

The alignment of the electrodes relative to each other can only optimize the electrode-electrode distances, because it was not possible to measure the overall straightness of

such a long device at the required scale of accuracy. Micrometer screws were used to shift the subunits in the horizontal direction, whereas stainless steel foils with thicknesses between 10 and 100  $\mu\text{m}$  were used for positioning in the vertical direction. Gauge blocks of well defined thickness were used to measure the gap between adjacent electrodes during the alignment. To protect the electrodes from scratches, the blocks were wrapped in teflon tape. The distance between any two adjacent electrodes was finally maintained at  $(1.42 \pm 0.02)$  mm over the entire length of 1640 mm.

After aligning the electrodes inside the frame, the entire unit is inserted in the vacuum chamber. Using a HeNe positioning laser, an axis is defined inside the chamber that goes through the tip of the skimmer and intersects the axis defined by the light baffles in the detection chamber (see Subsection 4.3.2). Next, the assembly is aligned such that the axis defined by the laser lies between the electrodes. For this step, small cylindrical alignment tools are inserted into both ends of the electrodes. With an outer diameter of 4.5 mm and a length of 5 mm, the alignment inserts fit tightly between the electrodes. They are made from Vespel in order not to scratch the electrode surfaces. A 0.8 mm diameter hole in the middle of each tool allows precise alignment relative to the laser-defined axis on the order of 0.2 mm.

## 4.2.2 High-voltage electronics and switching scheme

### Electronics

A sketch of the electronics is shown in Figure 4.6. The four electrodes are connected to HV vacuum feedthroughs (Hositrad 16729-03-CF). The output of two fast high-voltage push-pull switches (Behlke Electronics, HTS 301-03-GSM, 30 kV) is connected to the feedthroughs of two opposing electrodes. In this way the high voltage applied to these electrodes can be switched between  $\pm 9.5$  kV in less than 0.5  $\mu\text{s}$ . The other two electrodes and the inputs of the switches are attached to two 500 nF high voltage capacitors (FHI Elab #3499) that are loaded by two 20 kV power supplies (FuG HCK 400-20000), one for each polarity. The maximum applicable high voltage that does not lead to flashovers between the electrodes is limited by the quality of the electrode surfaces.

Using a home-built burst unit with 10 ns resolution (FHI Elab #3388) the switches are triggered to alternate between two configurations. In order to compensate different signal runtimes for the switches due to different cable lengths, trigger times can be synchronized by the measurement software to within 5 ns, well below the rise and fall times of the switches of about 400 ns. In configuration 1, voltages of 9.5 kV are applied to the upper two electrodes while the lower two electrodes are at  $-9.5$  kV, creating a saddle-point of the electric field with strength of 48 kV/cm on the molecular beam axis. In the horizontal direction, the electric field increases with distance from the center whereas it decreases away from the center in the vertical direction. In going from configuration 1 to configuration 2, the voltage applied to the right upper (left lower) electrode is switched from 9.5 kV to  $-9.5$  kV ( $-9.5$  kV to 9.5 kV), effectively rotating the field configuration by  $90^\circ$ . As explained in Chapter 3, this rotation interchanges the focusing and defocusing directions for molecules inside the selector.

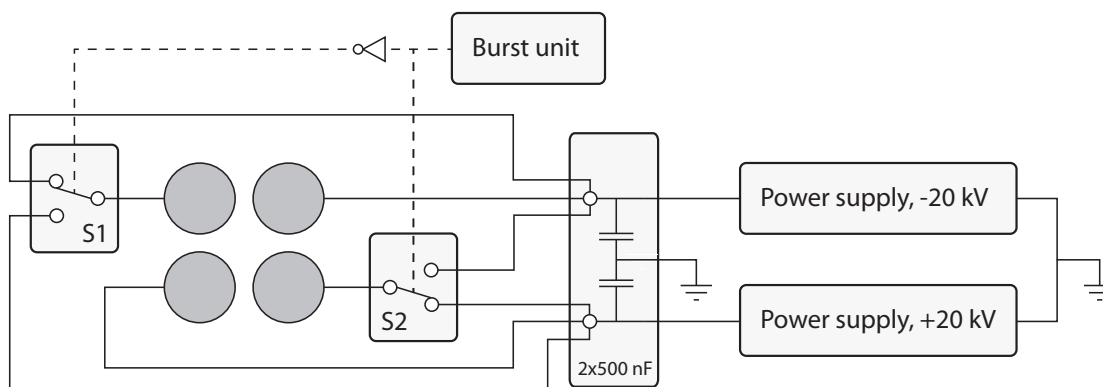


**Figure 4.6:** Schematic overview of the high-voltage switching electronics. Two power supplies provide high voltages to two fast switches (S1,S2). The output of the switches is connected to the electrodes, depicted as grey circles. The trigger signal is directly fed to one switch and inverted for the other switch.

After the initial setup and after each exposure to air, the electrodes must be "conditioned" with DC voltages to test whether the electric fields cause electric flashovers. Starting from ground potential, the voltages are increased in steps of 1 kV every 10 minutes as long as no flashover occurs. Otherwise, the voltage is held constant for 10 more minutes. Flashovers are detected by measuring the currents from the HV power supplies with digital multimeters (Fluke 87 V). The currents are limited by one 100 M $\Omega$  resistor per HV power supply. This way it can be deduced whether a flashover occurred between one electrode and another electrode or toward a part of the grounded vacuum chamber, possibly outside vacuum. The procedure ends at final voltages of  $\pm 12.5$  kV, 30% higher than the maximum switched voltages in the experiment, and is repeated for both configurations.

### Switching schemes

The alternation between the two configurations follows a rectangular waveform as shown in Figure 3.1. The waveform is characterized by the ac switching frequency ( $1/T$ ), typically in the range from 1 to 8 kHz, and the fraction of the period during which configuration 1 is applied, denoted as the duty cycle  $d$ . In the presented experiments values of  $d$  in the range 0.5–0.6 have been used (see Chapter 5 and Chapter 6).

The phase during a switching cycle is defined as the fraction of the complete cycle with length  $\pi$ . Therefore, when  $d = 0.5$  is chosen, configuration 1 is applied for phases in the range  $0-0.5\pi$  whereas configuration 2 is applied between  $0.5-1\pi$ . In this case, for example, at a phase of  $0.75\pi$ , configuration 2 is applied and the switching cycle is in the middle of the second half cycle.

A start (end) phase is defined for a molecule as the phase of the full switching cycle during which it enters (leaves) the selector. To achieve well-defined conditions when changing the switching frequency, two modes of operation are implemented: the se-

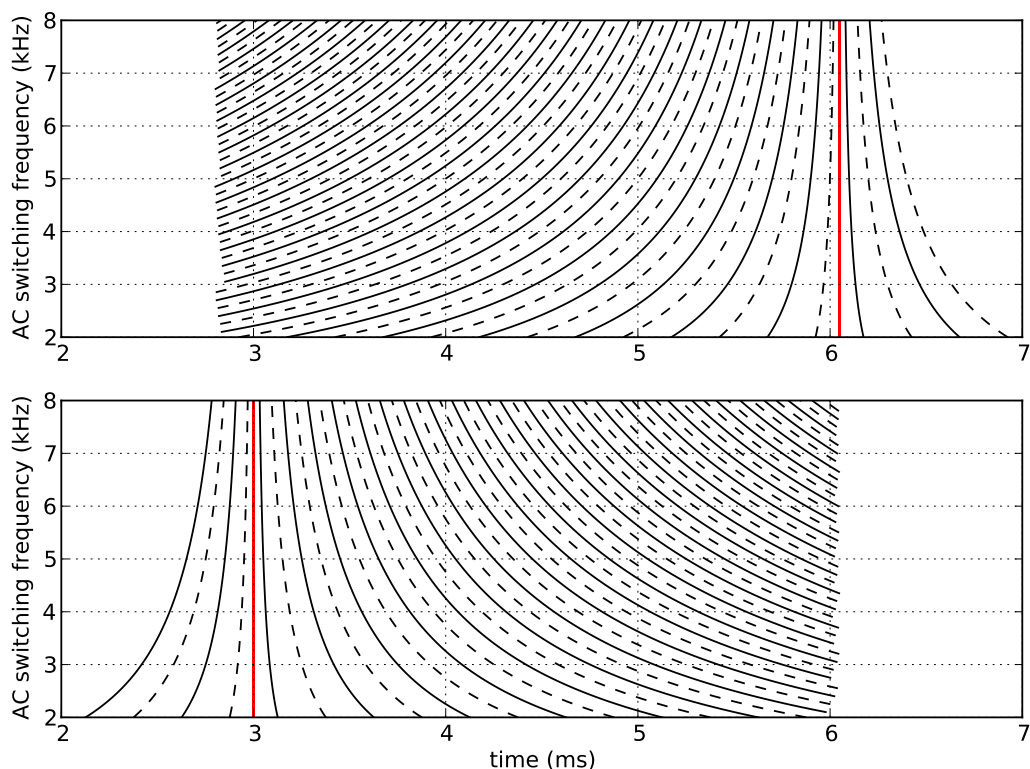


**Figure 4.7:** Schematic plot of burst sequences used in the experiment with duty cycle 0.5. Solid (dashed) lines are drawn at the times when the electric field configuration is switched from  $1 \rightarrow 2$  ( $2 \rightarrow 1$ ). Upper panel: Switching sequences with fixed end phase  $0.25\pi$  at 6.03 ms. Lower panel: Switching sequences with fixed start phase  $0.2\pi$  at 3.0 ms. Vertical red lines show the time at which the phases are held fixed.

quences are arranged to have the same start or end phase at a specific time for all frequencies. In Figure 4.7, two such arranged sequences for the experiment are visualized. For switching frequencies in the range from 2 to 8 kHz, sequences are generated with a duty cycle  $d=0.5$  in steps of 50 Hz. The solid (dashed) lines connect times at which the electric field configuration is changed from  $1 \rightarrow 2$  ( $2 \rightarrow 1$ ). In the upper panel sequences with a fixed end phase of  $0.25\pi$  are shown. The end phase appears at 6.03 ms, after which two more complete switching cycles are added to accommodate molecules longitudinally trailing the middle of a molecular packet. Corresponding sequences with a fixed start phase of  $0.2\pi$  are shown in the lower panel. Here, two more cycles are added before the beginning of the sequence, in order to accommodate molecules flying into the selector ahead of the central part of the packet.

## 4.3 Rotational-state-specific detection

The detection system for molecules in single rotational quantum states consists of a narrow bandwidth continuous wave (cw) laser system with an external active frequency control, and a computer-based time-resolved photon counting detection system [47].

### 4.3.1 Laser system

After leaving the selector, the molecular beam is crossed by a narrow bandwidth cw laser, and the molecules are monitored via laser-induced fluorescence (LIF) detection. The detection laser system, as shown schematically in Figure 4.8, is set up on a vibration-damped optical table placed below a laminar flow box that blows out filtered and temperature-controlled air. A narrow bandwidth cw ring dye laser (RDL, Coherent RDL899-21) is operated with Rhodamine 110 (Radiant Dyes) dissolved in ethylene glycol and pumped at 514 nm either by an argon ion laser (Coherent Sabre, 15 W) or a disk laser (ELS MonoDisk, modified by Dausinger und Giesen, 12 W) which are typically operated at 5 W. The pump power is adjusted between 4 and 6.5 W to compensate for the losses due to the short lifetime of Rhodamine 110 ( $\sim 250$  h/W). Typically 350 to 550 mW of continuous light around 548 nm is obtained this way. Active frequency stabilization is used to keep the center frequency stable within an interval of 2 MHz for several hours, as described in Subsection 4.3.3.

A small fraction of the output power is split off behind the RDL for frequency analysis. Using a confocal Fabry-Pérot interferometer (FPI) with a free spectral range of 150 MHz, the frequency is calibrated during scans. Simultaneously, a part of the split-off light is fed to a wavemeter (Highfinesse WS/6) that monitors the absolute laser frequency with an accuracy of  $\pm 700$  MHz and a resolution of 100 MHz. Another part of the laser light is split off into a home-built iodine cell [76]. By comparison to the known iodine absorption spectrum [77] the absolute laser frequency can be determined with an accuracy of about  $\pm 200$  MHz. Wavemeter frequency, iodine absorption signal and intensity behind the FPI are recorded during frequency scans.

Large periscopes are used to guide the laser beam over an about 15 m long elevated path to the experiment that is located in a separate laboratory. An active beam path stabilization system is used (MRC "Dynamic") to compensate for drifts and vibrations of the laser table and of the mirrors used in the beam path. The position of the laser beam at the experiment is measured using a quadrant diode detector that detects the light leaking through a highly reflective mirror behind the periscope. In a closed loop a correction signal is generated from the measured position and is fed to the first mirror of the periscope next to the laser table that is Piezo actuated. In this way the beam position at the experiment can be stabilized to within  $\approx 100$   $\mu\text{m}$ .

An optical enhancement ring cavity (Spectra Physics, LAS Wavetrain) is placed on the aluminum frame that holds the vacuum chamber. The laser light is frequency doubled using a beta barium borate (BBO) crystal placed at the focus of the cavity. The cavity length is locked to the laser frequency following the Pound-Drever-Hall method [78]. Typically, 10 to 30 mW of light is produced at 274 nm with an instantaneous bandwidth of less than 1 MHz.

### 4.3.2 Laser-induced-fluorescence (LIF) detection

In this section, the setup of the LIF detection zone in the detection chamber and the data acquisition via a dedicated computer system are described.

#### Detection chamber

The laser intersects the molecular beam inside the detection chamber at a right angle. As the transverse velocity spread of the molecular beam is very small in the direction of the laser<sup>1</sup>, the resulting Doppler broadening is small as well. Therefore, for this geometry, rotational resolution of electronic transitions can be achieved with a narrow-bandwidth laser system.

The laser light enters and exits the detection chamber through Brewster windows. Stray light is reduced by light baffles that are mounted in a tube inside the Brewster windows. The light baffles consist of blackened 5 mm diameter pinholes and skimmers. They are aligned such that the transmitted laser beam intersects the molecular beam axis at a right angle in the center of the chamber. Behind the second Brewster window the intensity of the transmitted light through the vacuum chamber is measured using a photodiode to normalize the LIF signal.

Using a lens system, LIF photons from the point of interaction are imaged onto a photo-multiplier tube (PMT) (Electron Tubes Lim., B2F/RFT). Two 50 mm diameter lenses with focal lengths of 50 and 100 mm form a telescope between the interaction point and the PMT. A concave mirror (focusing length 500 mm) focuses photons traveling downward back to the molecular beam axis so that they are imaged onto the PMT as well. The photon beam exits the vacuum chamber through a Suprasil quartz window. Above the window, at the focus of the beam, a spatial filter (opening 12 mm × 5 mm, long side aligned parallel to the laser beam) limits the acceptance angle for LIF photons. In this way, the detected stray light is reduced, because the detection volume imaged onto the detector is limited. Above the spatial filter a band pass filter reduces stray light in the visible range (Schott UG 11, thickness 2 mm).

#### Data acquisition

Data acquisition is performed on a dedicated computer that is running the VxWorks 5.5 real time operating system. A Intel Pentium 3 CPU, a delay generator, a burst unit, and a digitizer are put in a crate and connected over a cPCI bus for fast data transfer. The home-built delay generator (FHI Elab #3294.1) controls the trigger timings of the burst unit that performs the ac switching sequence, the nozzle opening trigger, and the beginning of the data acquisition of the two-channel digital oscilloscope (Acquiris, DC440, 2.4 ns resolution, 420 MSamples/s at a typical repetition frequency of 40 Hz). All components are controlled and read out by the home-built rtKouDA software. A 12 bit A/D converter records the signals from the UV-normalization diode, reference

---

<sup>1</sup>In free flight and at a forward velocity of 600 m/s only molecules with a maximum transverse velocity of  $\pm 2$  m/s can reach the detection region, thereby adding a Gaussian contribution to the line width of about 1 MHz.

150 MHz etalon, RDL power, and iodine cell. From a desktop computer running Linux, the KouDA desktop program (home-built as well) controls rtKouDA over an ethernet connection [79].

The PMT current is converted to a voltage. Using the digital oscilloscope the signal is digitized at a typical time resolution of 5 ns, which is high enough to resolve the signals from individual photons. At the highest resolution of 2.4 ns, the data processing takes too long to operate at the desired repetition rate of 40 Hz. Using rtKouDA, time-resolved photon-counting is performed on the obtained signal for 1.5 ms and the detected photons are binned into time intervals of 2  $\mu$ s.

Optionally, the signal from the photodiode that records the transmitted UV-laser intensity can be recorded simultaneously on the second digitizer channel. As implemented, the analog signal is recorded with the time resolution of the photon-counting channel and is subsequently averaged over all points inside each 2  $\mu$ s bin. The resulting signals are transferred to KouDA and the photon signal can be normalized bin-wise to the UV laser intensity. In KouDA further computations on the obtained signals can be performed. KouDA can also read out the Wavemeter to record the RDL frequency as reference during measurements, albeit at the somewhat limited resolution that itself is not sufficiently high for the spectroscopic demands of the experiment.

### 4.3.3 Laser-frequency stabilization

In this section, a detailed explanation of the laser frequency stabilization system is given. The system is built from standard components and controlled by a dedicated computer running home-built software.

Ring-dye lasers enable high-resolution spectroscopy, but are strongly coupled to their surrounding environment. Long and short time drifts are observed as well as frequency jitter, resulting in a low long-term frequency stability. In its standard setup, our ring-dye laser features an inherent line width of some 100 kHz but is subject to frequency drifts of typically more than 100 MHz/h, even in a temperature-stabilized environment.

Some experiments, however, that involve RDLs for single-rotational-state detection, e. g., AG deceleration of polar molecules [32], require laser frequencies that are stable over an entire day. The line widths of rovibronic transitions are of the order of 10 MHz, e. g., for benzonitrile. Therefore the frequency should at least be stable to within 2 MHz per day to keep it at the center of the probed transition over a long measuring period.

Generally, stabilization is based on continuously measuring the laser frequency and a feedback loop correcting for deviations from the desired frequency. An error signal is generated and the RDL cavity is tuned accordingly. Our frequency stabilization control is a home-made tabletop system built from relatively inexpensive standard components and a custom control software. The working principle that is detailed hereafter has originally been proposed by Lindsay *et al.* [80] and has also been implemented by Jaffe *et al.* [81], and for diode lasers by Burke *et al.* [82].

As shown in Figure 4.8, a fraction of the RDL beam is overlapped with the reference laser and coupled into a continuously scanned Fabry-Pérot interferometer. Independent timers measure the elapsed time between the beginning of each scan and the appearance

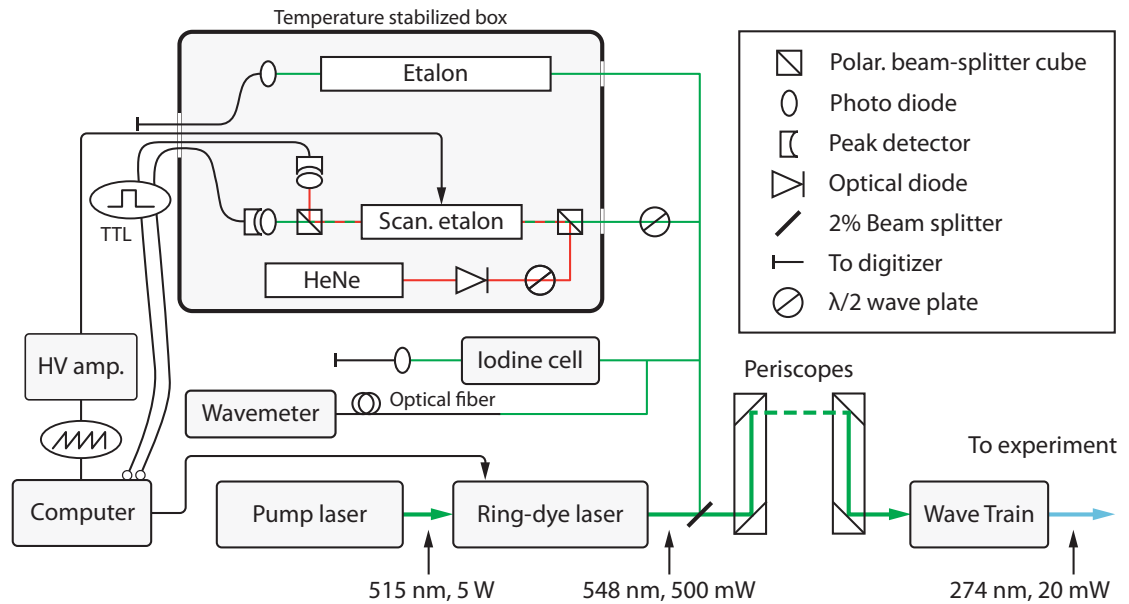


**Figure 4.8:** Main components of the frequency calibration and stabilization system. A small part of the main ring-dye laser beam is coupled into the temperature-stabilized box that contains the reference laser, the scanning FPI, and the detection units. The signals are processed by a compact control system that feeds the correction signal back to the RDL.

of transmission fringes when the FPI is on resonance with either of the two probed laser frequencies. In this way the frequency difference is expressed as a time difference that is used as input parameter for the stabilization loop. From the time difference, the software PID-controller generates a corrected voltage which is amplified and fed back to the RDL. The individual optical components are installed inside a temperature-stabilized box that is installed on the optical table next to the RDL. The RDL frequency can be stabilized this way and can be scanned by changing the controller's stabilized time difference set point.

### Optical components

The frequency-stabilization setup is shown schematically in Figure 4.8 and the components are detailed in Table A.1. Using a 2% beam splitter, a fraction of the fundamental light is split-off behind the RDL. A frequency-stabilized HeNe-laser (SIOS SL-03) serves as frequency reference. Internally, the intensity of two perpendicularly transverse polarized modes is monitored independently and the laser cavity is controlled thermally such that the two modes have the same intensity. One mode exits the laser head with a resulting frequency stability of  $\pm 1$  MHz per hour. In order to suppress back-reflected laser light an optical isolator is placed behind the HeNe laser.

The HeNe beam and the RDL beam are overlapped using a polarizing beamsplitter

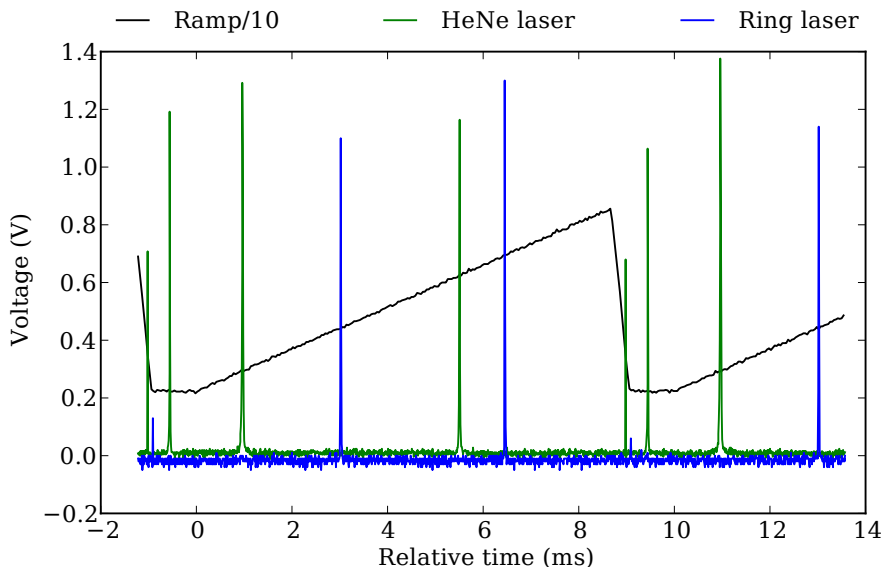


**Figure 4.9:** Time-dependent signals in the frequency stabilization. Black: voltage ramp generated by the AWG that is fed to the interferometer driver. Green and blue: transmission of light from the HeNe and RDL lasers through the interferometer (scaled up 10-fold for clarity).

cube (PBS). In order to achieve a high transmission of the laser beams, half-wave plates are installed before the beams enter the PBS. The overlapping beams are coupled into a scanning Fabry-Pérot interferometer (Toptica FPI 100) with a free spectral range of 1 GHz. The mirrors cover the range of 430 to 660 nm. One mirror is mounted on a Piezo-motor, thereby allowing tuning of the interferometer’s resonance frequency by one spectral range per 30 V applied to the motor. Typically, the FPI is driven by a 100 Hz sawtooth voltage that is generated by the control computer.

Behind the interferometer the two collinear laser beams are separated with a second polarizing beamsplitter cube. They are detected independently using two fast photodiodes (Thorlabs Det110) selected for the wide spectral range of 350 to 1100 nm. The signals from the photodiodes are shown together with the ramp that drives the interferometer in Figure 4.9 over one period of the voltage ramp. Starting at  $t = 0$  from 2.2 V, the ramp voltage is increased linearly until the maximum value of 8.6 V is reached at 8.3 ms. The voltage is subsequently driven back to the start value that is reached after 9 ms and kept constant until the next period is started at 10 ms in order to let the piezo relax back to its start position. For both lasers two peaks are observed during the rising edge of the ramp, because for the chosen ramp parameters the interferometer is scanned over more than two free spectral ranges.

The photodiode signal is fed to home-built peak detectors (FHI Elab #3398) that differentiate the signal and generate TTL pulses on each zero crossing of the differentiated

signal, i. e., the maximum of the transmission fringe (see Section A.2 for details). The TTL pulses are then passed to the computer control system that records the detection time relative to the start of the actual ramp period for the two peaks that appear during the rising edge of the ramp.

A second, confocal quasi-Fabry-Pérot-Etalon with a fixed free spectral range of 150 MHz<sup>2</sup> (300 MHz in Fabry-Pérot mode) is located in the frequency control box. From the transmitted intensity, the position of each transmission fringe can be obtained. Using these positions, a spectrum can be linearized and, because of the known free spectral range, the frequency axis can be scaled accurately to absolute frequencies. Linearizing the spectrum is necessary because the timing difference of detected peaks is proportional to the applied FPI voltage but not to the laser frequency as the timing difference is scanned.

The entire setup is embedded in a thermally isolated box which is temperature-stabilized to  $(27.00 \pm 0.02)^\circ\text{C}$ . The scanning etalon is placed in a vacuum chamber to minimize the influence of air humidity and pressure variation, e. g., sound waves created by ambient noise. After starting the FPI ramp and the reference laser, the temperature in the temperature stabilized box rises by about 0.1 K and returns to its set point after one hour. From day to day, the set point of the RDL frequency has typically to be corrected by about 2 MHz. When the system is fully warmed up after several days of continuous operation often no further correction is needed.

### Computer setup

A dedicated computer (MEN, Kahlua Box), a compact industrial control system based on a PPC processor, serves as control unit running the real-time operating system VxWorks 6.3. It is equipped with an arbitrary waveform generator (AWG) (MEN M68, resolution 16 bit, bandwidth 100 kHz) and a timer (MEN M72 M-Module, 4 independent counters).

The AWG is used to generate the sawtooth voltage shown in Figure 4.9 and Figure A.2 at a 100 Hz repetition frequency. It is amplified by a home-built HV amplifier and fed to the FPI to drive the Piezo translator. Three counters of the timer are started simultaneously with the AWG ramp during each cycle following the control logic depicted in Figure A.3. They are stopped by the TTL pulses from the first detected HeNe fringe and the two detected RDL fringes, respectively.

Two independent proportional-integral-derivative (PID) controllers are implemented in software following a standard digital PID control scheme (see Section A.4 for details). In addition to the standards, the implementation focusses on two critical aspects: rapidly finding the initial set point and changing the set point rapidly for RDL frequency scans. The PID parameters are chosen empirically and can be changed during runtime.

The detection time of the first observed HeNe transmission fringe is used as an input parameter for the first PID controller. As the etalon length, and therefore its resonance frequency, changes with temperature, the HeNe fringe position drifts significantly during warm up. A complete warm up takes several days, during which the system must operate

---

<sup>2</sup>The free spectral range of the confocal etalon at room temperature has been determined to  $(149.948\,67 \pm 0.000\,22)\text{MHz}$  by several measurements of the iodine spectrum in a well defined frequency range [47].

continuously. Even after a complete warm up, a slow drift can be caused by the aging of the Piezo, resulting in a changed elongation of the Piezo per applied voltage. To compensate for these effects, the controller adds a dc offset voltage to the ramp. The offset is calculated from the time difference between the set point and the measured fringe detection time.

The second loop generates the control signal for the RDL. From the time difference between one selected RDL fringe and the set point of the reference laser fringe, a voltage is generated. This voltage is amplified by another home-built amplifier and fed to the external frequency control input of the RDL.

Alternatively, the RDL control voltage can be set directly through a interface in the *KouDA* program (see below) for fast changes. Using the interface, all other relevant parameters can be changed as well.

### Characterization

The performance of the stabilization is characterized by recording the LIF signal (see Subsection 4.3.2) from a molecular transition over an extended period of time. Any signal loss is attributed to a frequency shift away from the center of the transition. The ramp stabilization to the reference laser was already running for several days prior to the measurements, which resulted in a full warm up thereof. In order to achieve a high signal-to-noise ratio, the detection vacuum chamber is placed directly behind the source chamber. Benzonitrile is seeded in argon at a backing pressure of 2 bar and at room temperature. The mixture expands into vacuum through a (laser-drilled) 30  $\mu\text{m}$  hole in the 0.8 mm thick wall of a Swagelok end cap. A continuous molecular beam is obtained that passes through a 1.5 mm skimmer and intersects the laser beam in the detection chamber about 20 cm behind the nozzle. The resulting steady-state pressure in the source chamber is comparable to the pressure obtained with the pulsed nozzle (see Subsection 4.1.2).

Due to its relatively short flight path, the measured LIF signal is so strong that the amplified voltage from the PMT is measured directly without the single-photon counting procedure. A photodiode is placed behind the exit Brewster window of the detection chamber and read out to normalize the molecular signal. In this way the varying UV-laser intensity can be compensated on a sub-second time scale as well as on longer time scales. At this detection position, due to a larger Doppler-contribution, the observed rotational lines exhibit an increased line width (28 MHz, FWHM, *vide infra*) compared to the experiments discussed in the later chapters. This increased width, however, it does not affect the investigation of the laser-frequency stability.

The output voltages of the PMT and photo diode are measured simultaneously on the two input channels of a digitizer. At a repetition rate of 10 Hz the signals are sampled for 90 ms at a sample rate of 100 MHz. During the remaining 10 ms in each cycle, the obtained data traces are transferred to the control computer which averages all traces obtained over a period of 1 s.

First, the rotational temperature of the benzonitrile beam is estimated from a small part of the vibrationless excitation spectrum of the electronic  $S_1 \leftarrow S_0$  transition. The

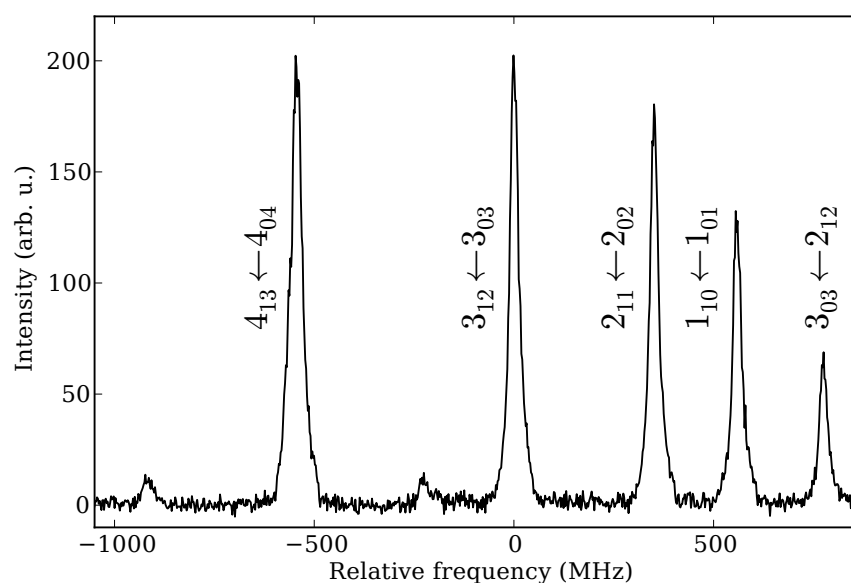


**Figure 4.10:** Rotationally resolved electronic excitation spectrum of benzonitrile obtained from the continuous molecular beam. The horizontal axis is relative to the frequency of the  $3_{13} \leftarrow 3_{03}$  transition.

spectrum, which is shown in Figure 4.10, is obtained by scanning the UV laser frequency in a small frequency range around  $36\,512\text{ cm}^{-1}$  in steps of  $2\text{ MHz}$  ( $\approx 0.000\,067\text{ cm}^{-1}$ ) and normalizing the molecular signal with respect to the laser intensity. Rotational spectra are simulated for different rotational temperatures from which the best agreement with the experimental data is seen for about  $3\text{ K}$ . The  $3_{13} \leftarrow 3_{03}$  transition is then chosen for the following measurements because it has the strongest signal in this range.

The inset in the left panel of Figure 4.11 shows a zoom in on the  $3_{13} \leftarrow 3_{03}$  transition and a Lorentzian fit. From the fit the center frequency and the linewidth ( $28\text{ MHz}$ , FWHM) are obtained. The LIF signal is then normalized to the intensity at the center of the transition. In the following discussion any change of the LIF intensity over time is attributed to a frequency shift away from the center of the transition. The absolute shift can be calculated from the "inverted" Lorentzian function.

In the left panel of Figure 4.11 the change of the LIF intensity over time is shown after setting the RDL frequency to the center of the transition. The green curve shows a  $25\text{ min}$  measurement during which the frequency stabilization is turned off after  $20\text{ s}$ . During the  $75\text{ min}$  measurement shown as blue curve the laser frequency has been stabilized continuously. When the stabilization is turned off, the LIF signal starts to fluctuate very quickly, which indicates that the laser frequency shifts away from the center of the transition. Already during the first  $10\text{ min}$ , a frequency shift of  $5\text{ MHz}$  is observed that alone would distort a state-specific measurement. After  $20\text{ min}$ , the LIF intensity decreases to  $10\%$  of the peak value and only very few molecules in the  $3_{03}$  state are

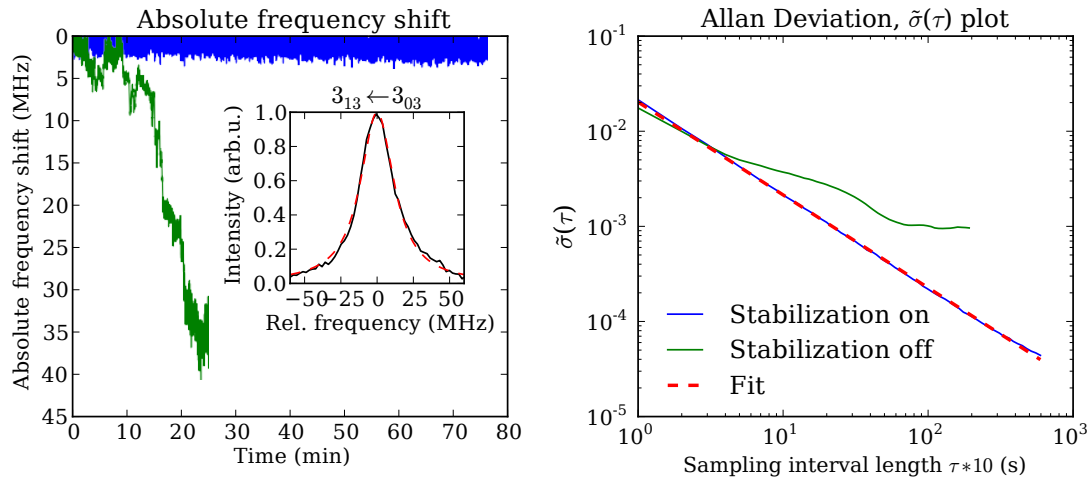


**Figure 4.11:** Absolute frequency shift in the UV over time with the stabilization on/off (blue/green curves). The inset in the left panel shows a frequency scan over the  $3_{13} \leftarrow 3_{03}$  transition, also shown in Figure 4.10, and a Lorentzian fit (dashed curve). The right panel shows a plot of the Allan Deviation,  $\tilde{\sigma}$ , as a function of the sampling interval length,  $\tau$ , see text for details. The dashed curve shows a linear fit to the stabilized measurement (dashed curve) with a slope of -0.98.

detected. At this laser frequency other transitions could already be induced that are lying close-by due to the high density of states. This would lead to a further distortion of state-specific studies.

When the laser frequency is actively stabilized, however, it remains constant during the displayed time period of more than one hour. Over the depicted time interval, the absolute frequency shift has a root-mean-square value of  $\pm 0.49$  MHz which can be regarded as the effective bandwidth of the RDL (the intrinsic bandwidth is on the order of some 100 kHz).

The time domain stability of the laser frequency is analyzed by calculating the Allan Variance (AVAR) and its square root, the Allan Deviation (ALDEV) [83]. This method is commonly used in frequency-stability analysis, e. g., for the characterization of atomic clocks [84] and for the quantization of noise in optical tweezers and their optimization [85, 86]. For calculating the AVAR, the time data is split into  $M$  sampling intervals of length  $\tau$ . Then, the average signal,  $y$ , is calculated for each interval as well as the difference of the  $y$ -values of all pairs of adjacent intervals. In its simplest form, the non-overlapped or 2-sample variance, is defined as

$$\sigma_y^2(\tau) = \frac{1}{2(M-1)} \sum_{i=1}^{M-1} (y(\tau)_{i+1} - y(\tau)_i)^2. \quad (4.1)$$

Usually the Allan Deviation  $\sigma_y = \sqrt{\sigma_y^2}$  is plotted as a function of  $\tau$  on a log-log scale. Domination by gaussian noise, for example, can be identified from the resulting curve

being a straight line with slope -1, whereas a frequency drift would result in a positive slope at long averaging times.

An improved measure is achieved with the overlapping-samples variant of the Allan Variance,  $\tilde{\sigma}$ . It involves calculating the  $y$ -values of sampling intervals which completely overlap with neighboring intervals:

$$\tilde{\sigma}_y^2(\tau) = \frac{1}{2m^2(M - 2m + 1)} \sum_{j=1}^{M-2m+1} \sum_{i=1}^{j+m-1} (y(\tau)_{i+m} - y(\tau)_i)^2. \quad (4.2)$$

Here, the averaging factor,  $m$ , is the number of overlapping intervals from which the  $y$ -values are calculated.

In the right panel of Figure 4.11 the outcome of an Allan Deviation analysis of the laser frequency is shown as a plot of  $\tilde{\sigma}(\tau)$ . Calculation of the Overlapped Allan Deviation is performed on the normalized LIF signal. For the measurement with stabilized laser frequency, an almost linear decrease of  $\tilde{\sigma}$  with increasing  $\tau$  is seen. The slope of a linear fit to the data, shown as a dashed line in the plot, yields a value close to -1. Therefore, in the studied time interval, the dominant noise is of Gaussian type and there are no indications of a frequency drift.

## Chapter 5

# Rotational-state-specific guiding of benzonitrile<sup>1</sup>

In this chapter, the  $m/\mu$ -selector is characterized in detail, using pulsed beams of benzonitrile molecules in combination with rotational quantum state selective detection. The arrival time distribution as well as the transverse velocity distribution of the molecules exiting the selector are measured as a function of ac frequency and duty cycle for low-lying rotational quantum states. It is discussed how the  $\mu/\Delta\mu$ -resolution can be controlled through the applied ac waveforms to transmit molecules in small subsets of quantum states. The operation characteristics of the selector are found to be in quantitative agreement with the outcome of trajectory simulations. Furthermore, the transmission is measured as a function of the electric potentials applied to the selector and end-phase effects are studied. It is shown how the forward velocity of a molecular beam can be obtained from ac frequency scans and corresponding trajectory simulations.

### 5.1 Fluorescence excitation spectra

In Figure 5.1, a selected part of the rotationally resolved fluorescence excitation spectrum of benzonitrile is shown. The fluorescence signal is integrated over a time-interval of 0.5 ms, thereby accumulating the signal from all benzonitrile molecules in a pulse. The spectrum shown in the middle trace is recorded in free flight, i. e., without voltages applied to the selector. A total of nine clearly separated rotational lines, originating from nine distinct low-lying rotational levels, are recognized. From this spectrum, the rotational temperature of benzonitrile in the molecular beam can be accurately determined. Taking the known molecular constants of benzonitrile in the ground state [56] and in the electronically excited state [57] in combination with the degeneracy of the levels (spin statistics) and the rotational line intensities in the electronic transition [62], the observed spectrum can be simulated with the rotational temperature as the only adjustable parameter. A simulated spectrum for a rotational temperature of 1.2 K is shown in the lower trace, and is seen to match the experimental spectrum rather well. A Voigt profile with a Lorentzian (Gaussian) contribution with a FWHM of 8 MHz (3.7 MHz) is used in the simulation. The width of the Lorentzian contribution has been taken from previous high-resolution spectroscopy experiments [57] and is consistent with our present

---

<sup>1</sup>This chapter is based on reference 87.

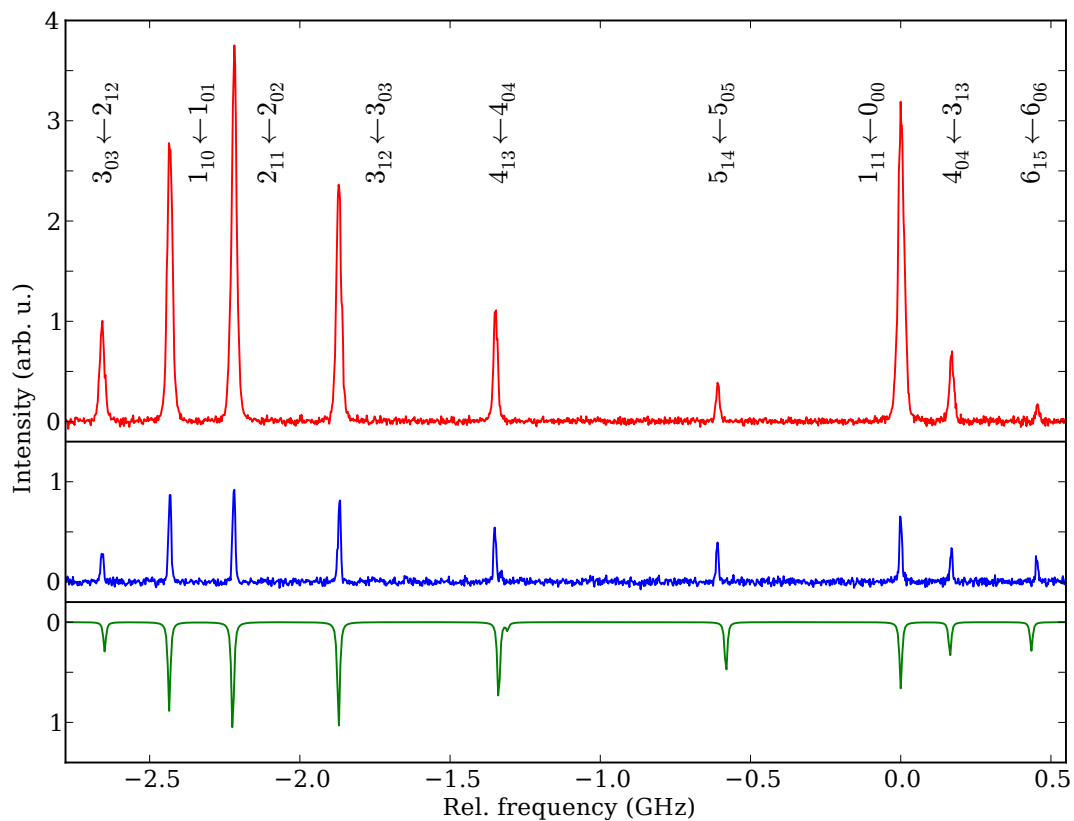


**Figure 5.1:** Rotationally resolved fluorescence excitation spectra of benzonitrile. The horizontal axis is relative to the frequency of the  $1_{11} \leftarrow 0_{00}$  transition at  $36\,512.74\text{ cm}^{-1}$ . Middle trace: Spectrum obtained without voltages applied to the selector, i.e., in free flight. Lower trace: Simulated free-flight spectrum (plotted upside down), assuming a rotational temperature of 1.2 K. The intensities are scaled to the intensity of the  $1_{11} \leftarrow 0_{00}$  transition in the middle trace and a Voigt profile with a Lorentzian contribution (FWHM) of 8 MHz and a Gaussian contribution (FWHM) of 3.7 MHz is taken. Upper trace: Spectrum obtained with the selector operating at an ac switching frequency of 3.8 kHz,  $d=0.50$ . The  $J'_{K'_a K'_c} \leftarrow J_{K_a K_c}$  assignment for each of the rotational lines is indicated.

observations. It should be noted that the radiative lifetime of the vibrationless level in the  $S_1$  state is about 70 ns [88, 89], thus contributing less than 2.5 MHz to the observed homogeneous linewidth; the remaining contribution has to result from pure dephasing, with an associated pure dephasing time of about 60 ns. In the upper trace, the spectrum obtained with the ac quadrupole selector operating at a switching frequency of 3.8 kHz, and with a duty cycle of 0.50, is shown. The fluorescence intensity is plotted on the same scale as for the spectrum recorded in free flight and an increase in peak intensity of almost a factor five is obtained for benzonitrile molecules in their rotational ground state ( $0_{00}$ ) level. For rotational transitions starting from rotationally excited levels the intensity increase upon using the selector is seen to be smaller, however, and the intensity even decreases for the transitions starting from the  $5_{05}$  and the  $6_{06}$  levels.

It is evident from the spectra shown in Figure 5.1 that the rotational transitions are broadened when the selector is switched on. This is seen more clearly in Figure 5.2 where an expanded view of the  $1_{11} \leftarrow 0_{00}$  transition, recorded with the selector on (upper trace) and off (lower trace), is shown together with the best fitting Voigt profiles. As the Lorentzian contribution to the profiles is kept fixed to 8 MHz, the width of the Gaussian contribution and the peak intensity are the only fitting parameters. A Gaussian contribution with a width of 3.7 MHz is obtained under free-flight conditions, determined by the residual Doppler broadening and the bandwidth of the laser system. When the selector is on, the width of the Gaussian contribution increases to 19.1 MHz due to the increased transverse velocity of the benzonitrile molecules exiting the selector. The spectrally integrated line intensity increases by a factor of 9.3 when the selector is switched on. As the transverse spatial distribution of the molecules exiting the selector will be larger, the overlap with the detection laser will be somewhat smaller, implying that this factor 9.3 is a lower limit for the overall increase of the transmission of benzonitrile molecules in the  $0_{00}$  level upon switching on the selector.

The spectral line-profiles shown in Figure 5.2 are recorded by accumulating the fluorescence signal from all ground-state benzonitrile molecules in the pulse. When these line profiles are measured in narrow time intervals, the time dependence of the transverse velocity distribution of the molecules exiting the selector can be measured. Such measurements are shown in two-dimensional plots in Figure 5.3. For this, the intensity of the fluorescence signal, binned in 2  $\mu$ s time-intervals, is plotted in a false-color representation as a function of the frequency of the excitation laser, which is scanned in 1 MHz steps from  $-40$  MHz to  $40$  MHz around the center frequency of the  $1_{11} \leftarrow 0_{00}$  transition. Interesting structures are observed in these two-dimensional plots, that are clearly different when the selector is operated at 3.45 kHz (left contour plot) or at 3.55 kHz (right contour plot). The panel on the left shows the time-integrated LIF signals as a function of the laser frequency. The Doppler shift on the vertical axis can be directly translated into a velocity component along the propagation direction of the laser, i.e., in the  $x$ -direction, and the corresponding velocity scale is given as well. The time on the horizontal axis is the time (in ms) since the triggering of the pulsed valve; the actual opening of the pulsed valve has a delay with respect to the trigger of approximately 0.2 ms. The panels at the bottom show the arrival time distributions integrated over the Doppler-broadened profiles that are seen to have a FWHM width of about 0.15 ms.

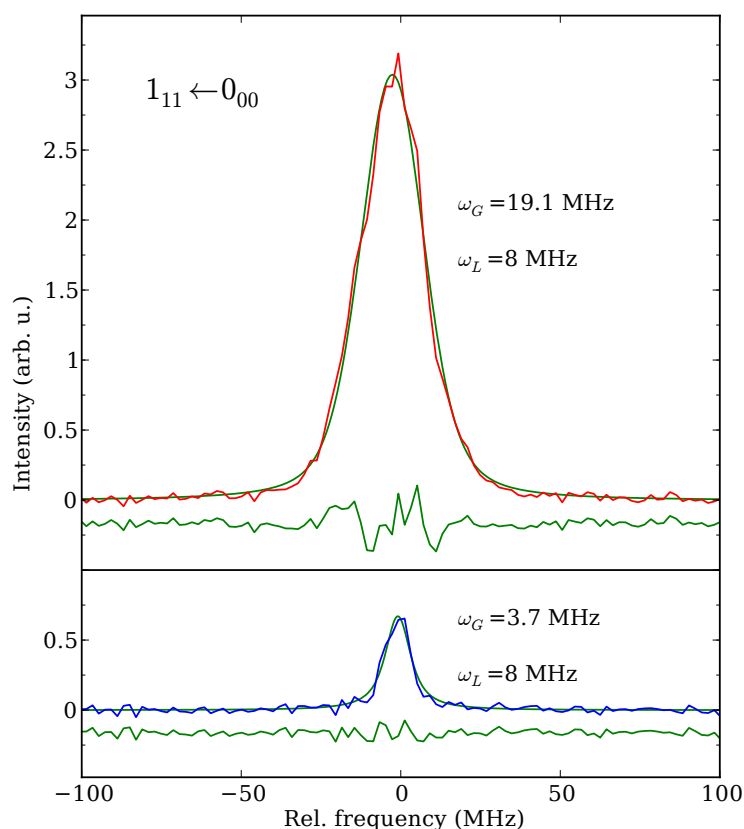


**Figure 5.2:** Expanded view of the  $1_{11} \leftarrow 0_{00}$  transition shown in Figure 5.1, measured with the selector on (upper trace) and off (lower trace). Voigt profiles fitted to the experimental data are shown and the widths (FWHM) of the Lorentzian and Gaussian contributions to the Voigt profiles are given. The difference between the observed and fitted profiles is shown underneath in green, slightly offset for clarity.

In Figure 5.4, the line profiles shown in Figure 5.3 are complemented with measurements at higher ac frequencies such that the range from 3.45 to 3.80 kHz is sampled. For comparison, the leftmost panel shows the transverse velocity distribution in free flight. This distribution is substantially narrower than those distributions in the panels to the right, i. e., when the selector is on. White arrows indicate particularly interesting arrival times in the molecular packet. The arrows pointing upwards (downwards) indicate arrival times of molecules that left the selector at the end of a horizontal defocusing (focusing) phase of the switching cycle. As the ac frequency is increased, the arrival time of molecules with a given end phase shifts to earlier times. In the distributions for ac frequencies of 3.45 kHz and 3.80 kHz, the same end phases appear at almost identical arrival times. At 3.80 kHz, however, the molecules experienced one additional switching cycle. When transmission curves are recorded, the detection laser is typically set to

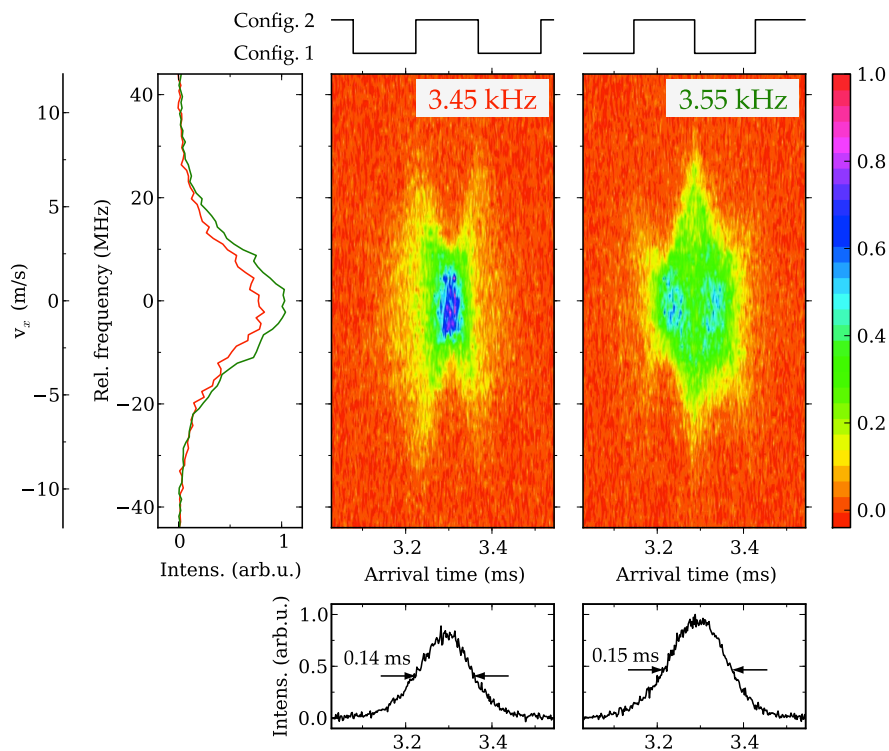


**Figure 5.3:** Intensity of the LIF signal, plotted in a false-color representation, as a function of the frequency of the excitation laser and as a function of arrival time for two different ac switching frequencies. The vertical axis is also given in terms of the velocity in the  $x$ -direction. Above the contour-plots, the phase in the switching cycle at which the molecules exited the selector is indicated. The panel on the left shows the time-integrated LIF signals as a function of the laser frequency and as a function of  $v_x$ . The panels at the bottom show the arrival time distributions integrated over the Doppler-broadened profiles.

the center of the probed transition, i. e., at the position corresponding to 0 m/s on the vertical axes in the figure, where a strong modulation of the signal as a function of the arrival time is seen.

In the experiments the switching sequence is started before the molecules enter the selector. The transverse velocity distribution that the molecules have in the detection region is mainly determined by the forces that the molecules experience near the end of the selector. For this reason, the end phase is schematically shown above the contour-plots in Figure 5.3. As the detection of the molecules is performed only 40 mm from the end of the selector and as the width of the longitudinal velocity distribution is sufficiently narrow, the arrival time of the molecules in the detection region can be directly mapped to an end phase.

In the measurements recorded with an ac switching frequency of 3.45 kHz, the molecules

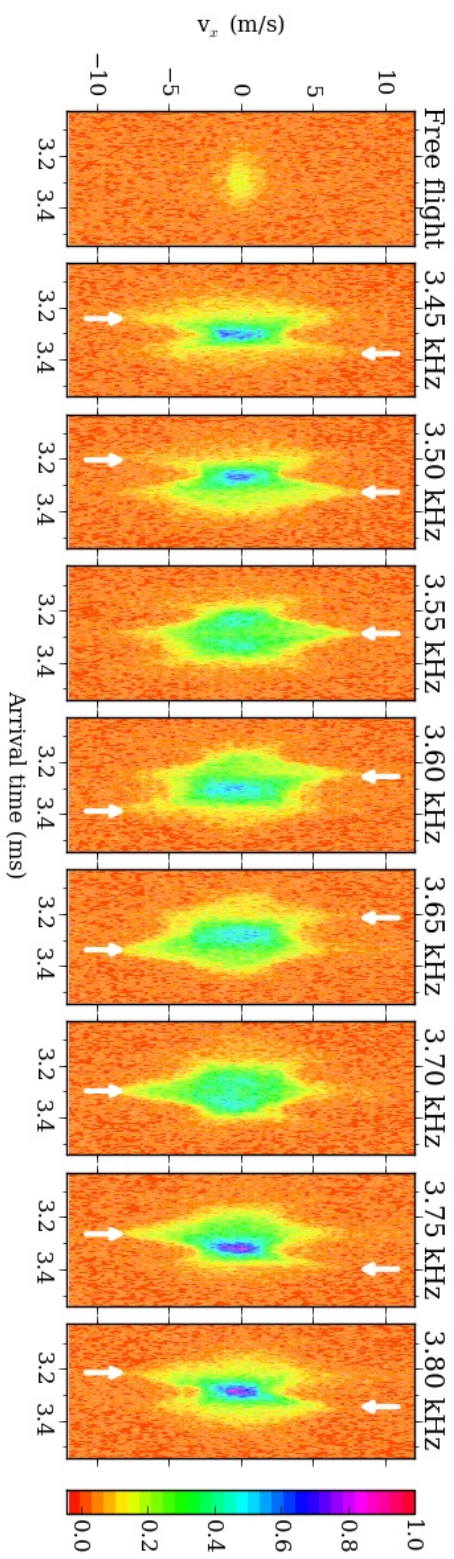


**Figure 5.4:** LIF signal intensity for eight different ac switching frequencies and for free flight, plotted to the same axes and in the same false-color representation as in Figure 5.3. The arrival time of molecules that exited the selector at the end of a horizontal defocusing (focusing) phase are indicated by white arrows pointing upwards (downwards).

arriving at 3.3 ms exited the selector in the middle of configuration 2, i.e., during the middle of a horizontal focusing phase. This is actually at a turning point of the micro motion in the selector, and thus results in a rather parallel beam and a correspondingly narrow spectral line-profile. In the measurements recorded at the slightly higher frequency of 3.55 kHz, the molecules arriving at 3.3 ms exited the selector at the end of a horizontal focusing phase. These molecules therefore have the maximal velocity components along the  $x$ -direction, leading to the broadest line-profile; benzonitrile molecules exiting the selector at the middle of either configuration 2 or configuration 1 again have a narrow spectral profile. Related experiments to visualize the motion of dynamically confined neutral particles have been performed on metastable CO molecules passing through an alternating gradient decelerator [64] as well as on Rb atoms in an ac electric trap [90].

## 5.2 AC frequency scans

In the upper panel of Figure 5.5, the time-integrated LIF signal of benzonitrile molecules in the  $0_{00}$  level is shown as a function of the ac switching frequency in the range from 2 to 8 kHz. The ac frequency is scanned in steps of 50 Hz for all curves except for the one at a duty cycle of 0.59, which is recorded in 10 Hz steps; the latter curve is shown once more on an expanded scale in the inset. The excitation laser is kept fixed to the center of the  $1_{11} \leftarrow 0_{00}$  transition and the signal intensity is normalized to the signal that is obtained when no high voltages are applied to the selector. To have well-defined conditions in the experiment, the timing of the ac switching sequence was arranged such that 0.2 ms after the trigger to the pulsed valve, i.e., at the moment that the pulsed valve opens, there is a fixed phase for all ac frequencies. Although this implies that the phase that a benzonitrile molecule experiences at the entrance of the selector, the so-called start phase, is different for different ac frequencies this start phase can be precisely calculated once the position of the molecule in the pulse and its velocity is known. The end phase is in this situation different for different ac switching frequencies as well, leading to the observed intensity modulation on the individual curves. All the different curves show no transmission of the selector below a certain cut-off frequency, followed by a steep onset of the transmission around 3 kHz, a maximum at frequencies between 3–4 kHz and a gradual decrease in transmission for higher frequencies. This general behavior has been described before [30], and is similar to a typical transmission curve in a quadrupole mass filter, for instance. At low ac switching frequencies the trajectories of the molecules are unstable, whereas at high frequencies the effective potential well in which the molecules are confined becomes very shallow. Only in an intermediate frequency range good transmission on stable trajectories is achieved. The transmission of the  $m/\mu$ -selector can be strongly modified when an asymmetric switching cycle is applied, e.g., when values of  $d \neq 0.50$  are chosen [65]. Transmission curves for six different duty cycles are shown to illustrate this. For a duty cycle of 0.50 the FWHM of the transmission curve for benzonitrile molecules in their ground-state level is about 1 kHz. With increasing duty cycle, the width of the transmission curve gets considerably narrower while the transmission intensity decreases. At a duty cycle

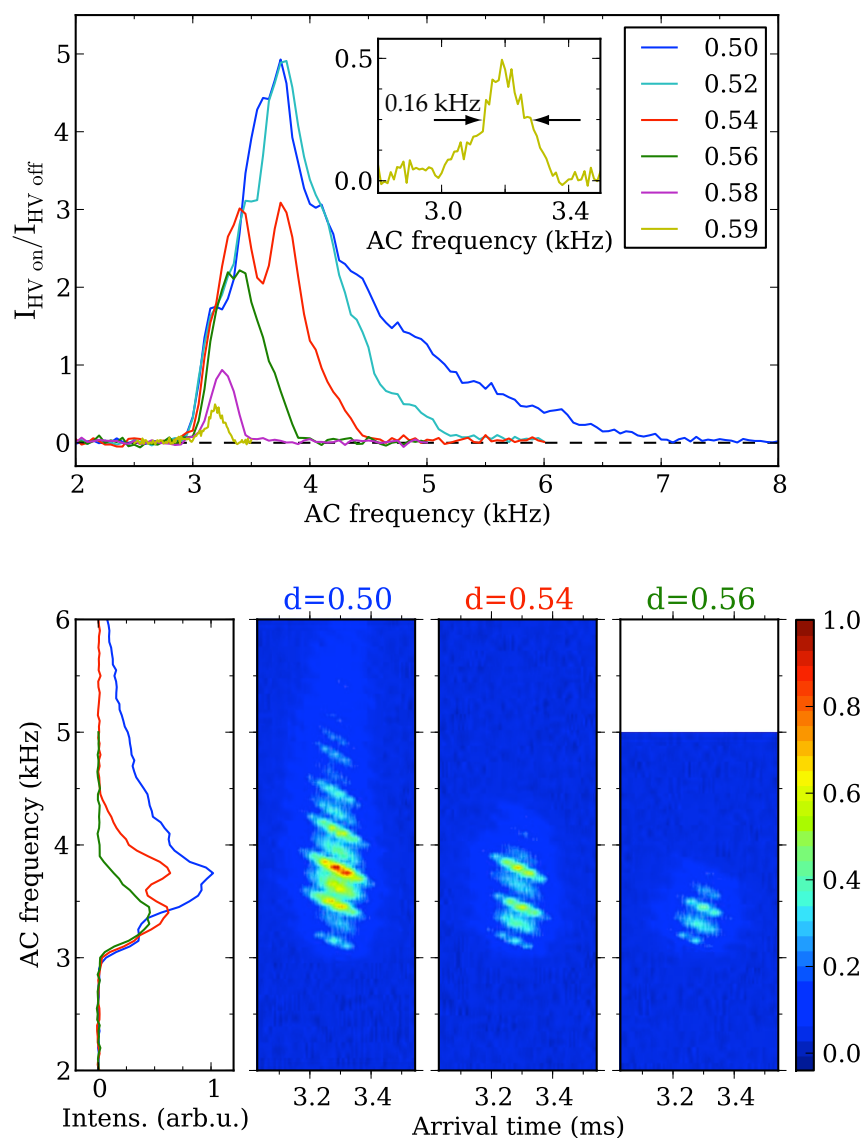


**Figure 5.5:** Upper panel: Time-integrated LIF signal intensity as a function of the ac switching frequency. Transmission curves are measured at six different duty cycles, indicated in the inset, while the laser frequency is kept fixed to the center of the  $1_{11} \leftarrow 0_{00}$  transition. The transmission curve for  $d=0.59$  is also shown on an expanded scale. The signal is normalized to the LIF intensity obtained in free flight. Lower panel: Measured intensity of the LIF signal, plotted in a false-color representation, as a function of the ac switching frequency and as a function of arrival time for three different duty cycles. The panel on the left shows the corresponding time-integrated LIF signals as a function of ac switching frequency.

of  $d=0.59$ , the FWHM of the transmission curve has decreased to 0.16 kHz, while the peak transmission of the selector is then reduced by about a factor ten.

In the lower panel of Figure 5.5, the intensity of the measured LIF signal is shown in a false-color representation as a function of ac switching frequency and as a function of the arrival time for three selected duty cycles. The transmission curves shown in the upper panel have been obtained by time-integrating these signals, and three of these are shown again in the lower panel on the left. To understand the two-dimensional plots, one has to realize that at a given ac frequency and with the excitation laser at the center of the rotational transition, thereby only probing molecules with small velocities in the  $x$ -direction, the most strongly peaked arrival time distribution is obtained for molecules exiting the selector in the middle of configuration 2. This is directly evident from inspecting the plots shown in Figure 5.3. As shown there, at an ac frequency of 3.45 kHz, these benzonitrile molecules produce a narrow arrival time distribution, peaked at 3.3 ms. With increasing ac frequency, the corresponding peak in the arrival time distribution shifts to earlier times, explaining the slopes of the intensity profiles observed in the lower panels of Figure 5.5. When the molecules exit the selector during the middle of configuration 1, i.e., during a vertical focusing phase, the overall intensity of the LIF signal is less. This can be understood from simple arguments: at the middle of either focusing phase, the beam coming out of the selector will be most parallel and its spatial distribution at the end of the selector will be maintained in the detection region. In the middle of a vertical focusing phase (configuration 1) the cloud of molecules is necessarily larger in the  $y$ -direction than in the middle of a vertical defocusing phase (configuration 2); this is actually the underlying operation principle of alternating gradient focusing. The spatial overlap with the laser beam will thus be smaller in the middle of configuration 1. Moreover, the velocity spread in the horizontal direction is larger in the middle of configuration 1 than in the middle of configuration 2. Both the decreased overlap in the vertical direction and the increased velocity spread in the horizontal one lead to a lower LIF intensity in the middle of configuration 1 than in the middle of configuration 2. This explains the occurrence of maxima with alternating intensity with increasing ac frequency, for a given arrival time. Of course, the profile of the arrival time distribution at any ac frequency is weighted by the intensity profile of the pulse, which is peaked around 3.3 ms and has a (FWHM) width of 0.15 ms. It is clear from these two-dimensional plots that when these are integrated over time to obtain the transmission curves as a function of the ac frequency, some remnants of the structure originating from the varying end phases remain.

The transmission curves shown in Figure 5.5 are for benzonitrile molecules in the  $0_{00}$  level. The overall transmission profile shifts to lower ac switching frequencies when the forces on the molecules are weaker, i.e., for benzonitrile molecules in rotational levels with smaller effective dipole moments. Transmission curves for other low-lying rotational states measured under the same experimental conditions as before are shown in Figure 5.6. For comparison, the ground-state transmission curves from Figure 5.5 are also shown in the uppermost panel. It is apparent from these measurements that the widths of the transmission curves can be reduced – just as for the ground state – by changing the duty cycle. Furthermore, the onset of the curves is shifted towards lower

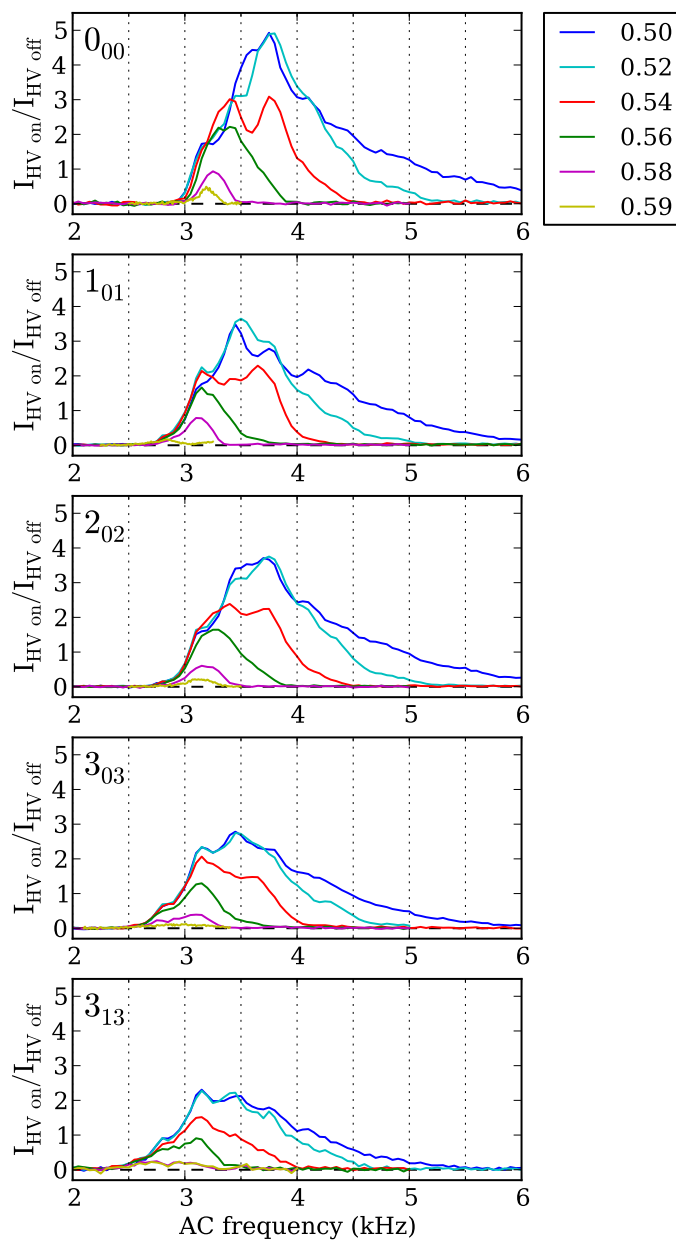


**Figure 5.6:** Time-integrated LIF signal intensity as a function of the ac switching frequency. Transmission curves are measured at six different duty cycles for benzonitrile molecules in five different rotational states that are indicated in the upper left corner of each panel. The signal is normalized to the LIF intensity obtained in free flight.

ac frequencies, relative to the ground state. Again the varying end phases imprint a structure on all transmission curves. For example, all curves show local maxima of the intensity at 3.15 kHz and 3.5 kHz switching frequency and local minima at 3.25 kHz and 3.95 kHz. From the transmission curves we see that the maximum relative intensity drops by about 50% in going from  $J=0$  to  $J=3$ . As discussed in more detail in Section 5.6, this is a result of the  $2J+1$   $M$ -components of every  $J_{K_A K_C}$ -state which exhibit very different transmission characteristics. (See Section 5.6 for further discussion.)

### 5.3 Rotational-state-selective transmission

The shift of the transmission curves along the ac frequency axis as a function of the effective dipole moment can be used to selectively transmit benzonitrile molecules in specific (subsets of) rotational quantum levels, as shown in Figure 5.7. The upper spectrum shows the part of the rotationally resolved fluorescence excitation spectrum recorded without the use of the selector, i. e., the free-flight spectrum, already shown in Figure 5.1. The spectrum in the center panel demonstrates that molecules in the  $0_{00}$ ,  $1_{01}$  and  $2_{02}$  rotational levels are not transmitted at all when the selector is operated at an ac switching frequency of 2.70 kHz and a duty cycle of 0.50. This switching frequency is below the abrupt low-frequency cut-off shown in Figure 5.5 and it is evident from the spectrum that only molecules in higher lying rotational levels are transmitted under these conditions. To create a beam containing only ground-state benzonitrile molecules, the selector has to be operated at ac switching frequencies above those of the transmission maximum, under conditions where the transmission curve has a rather steep frequency cut-off on the high-frequency side as well. This has been done in the recording of the lower spectrum, during which the selector was operated at an ac switching frequency of 3.8 kHz and at a duty cycle of 0.565. In this case, only molecules in the  $0_{00}$  and in the  $2_{02}$  rotational levels as well as a very small fraction of molecules in the  $1_{01}$  rotational level are transmitted. The relative population of these remaining rotational states in the molecular beam can be understood from the Stark-energy calculations in Section 5.4.

### 5.4 Stark-energy calculations

To quantitatively describe the operation characteristics of the selector we have to look in detail to the interaction of benzonitrile in any of the low-lying rotational levels with electric fields. In the following, we will restrict ourselves to the  $0_{00}$ , the  $1_{01}$  and the  $2_{02}$  levels, the lowest ones of the nine rotational levels probed in Figure 5.1, whose field-free energies are schematically depicted in the inset of Figure 5.8. In general, the force that neutral polar molecules experience in the electric field is given by the negative gradient of the Stark energy of the quantum level that they are in. This force can also be expressed as the product of the gradient of the electric field strength with an effective dipole moment,  $\mu_{\text{eff}}$ . This effective dipole moment is the negative derivative of the Stark energy of the particular quantum state with respect to the strength of the electric field. In the presence of an electric field, every  $J_{K_a K_c}$  level is split into

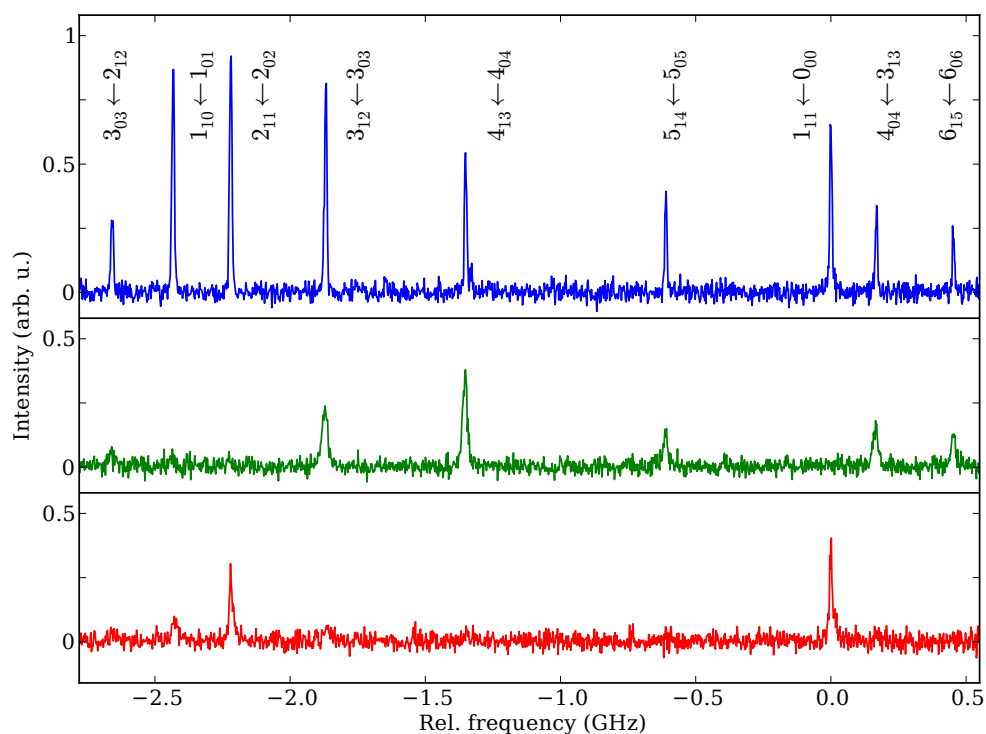


**Figure 5.7:** Rotationally resolved fluorescence excitation spectra of benzonitrile. Upper trace: Free-flight spectrum from Figure 5.1 in which the  $J'_{K'_a K'_c} \leftarrow J_{K_a K_c}$  assignment for each of the rotational lines is indicated. Middle trace: Spectrum obtained with the selector operating at an ac switching frequency of 2.7 kHz,  $d=0.50$ . Lower trace: Spectrum obtained with the selector operating at an ac switching frequency of 3.8 kHz,  $d=0.565$ .

$J+1$  different  $M$ -components, of which  $M=0$  is non-degenerate whereas all the  $M \neq 0$  components are doubly degenerate. The calculated effective dipole moments of the individual  $M$  components of the three rotational levels mentioned above are shown as a function of the electric field strength in Figure 5.8. At low electric field strengths there are several avoided crossings between levels of equal symmetry, resulting in a complicated dependence of  $\mu_{\text{eff}}$  on the strength of the electric field. At high electric field strengths, the effective dipole moments all converge to a value of  $0.0759 \text{ cm}^{-1}/(\text{kV}/\text{cm})$ , corresponding to the permanent electric dipole moment of benzonitrile of 4.52 Debye. In the selector, the molecules that are on stable trajectories experience electric fields in the range indicated by the shaded area in Figure 5.8. For benzonitrile molecules in the lowest rotational level, in particular, this implies that the value for the effective dipole moment is almost constant. It is also seen that the effective dipole moment is the largest for the ground state, explaining why it is completely absent from the transmission spectrum shown in the middle panel of Figure 5.7.

The effective dipole moment of the  $J_{K_a K_c} M = 2_{02} 2$  level is indistinguishable from that

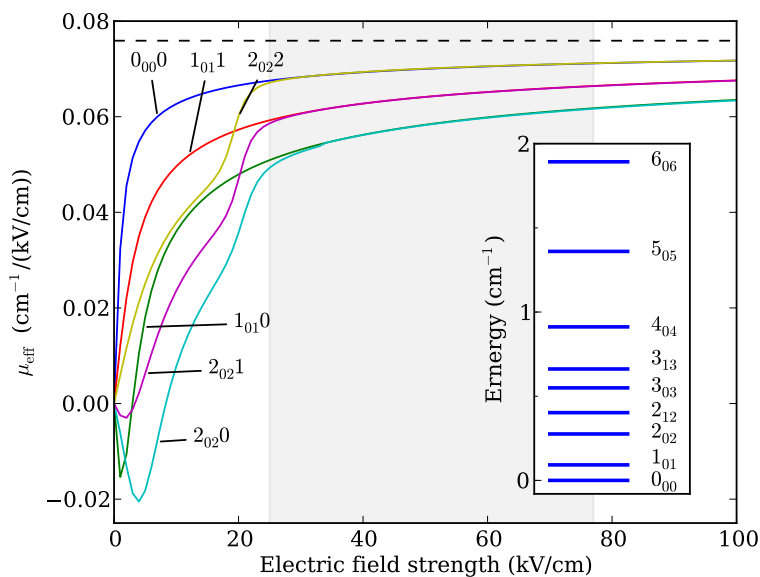


**Figure 5.8:** Effective dipole moments,  $\mu_{\text{eff}}$ , of low rotational quantum states of benzonitrile, labeled as  $J_{K_a K_c} M$ , as a function of the electric field strength. The dashed horizontal line indicates the permanent electric dipole moment of benzonitrile (corresponding to 4.52 Debye). The range of electric field strengths experienced by the molecules in the selector is indicated by the shaded area. In the inset the field-free energies of the nine rotational levels probed in the measurements shown in Figure 5.1 are depicted.

of the  $0_{00}$  ground state in the electric fields inside the selector. The value of  $\mu_{\text{eff}}$  for the  $M=1$  and  $M=0$  components of the  $2_{02}$  rotational level are lower, but are in turn almost identical to those of the  $M=1$  and  $M=0$  components of the  $1_{01}$  rotational level. This grouping of effective dipole moments originates from the electric field dependence of the Stark shifts in the so-called pendular or harmonic libration limit [91, 92]; although the grouping of effective dipole moments can be readily derived for a diatomic molecule [64] and even for a symmetric-top molecule [93], the correlation of the eigenenergies in the strong-field limit with those of the free rotor has not been rigorously analyzed for an asymmetric-top molecule like benzonitrile. Upon exiting the electric fields of the selector, the population in each of the  $M$  components adiabatically transfers to the (degenerate) field-free rotational levels. In the LIF detection zone, therefore, the summed population of all  $M$  components belonging to a certain rotational level is measured. This can nicely explain the degree of transmission of benzonitrile molecules in the  $2_{02}$  level through the selector as observed in the lower spectrum in Figure 5.7. The integrated LIF signal intensity of ground-state molecules in this spectrum is decreased to about 3/4 of its value in the free-flight spectrum, whereas this is about 1/3 for molecules in the  $2_{02}$  level. Considering that 40% of the molecules entering the selector in the  $2_{02}$  level will be in the  $M=2$  component, the observed intensity in the spectrum is as expected when only the ground-state level and the  $M=2$  component of the  $2_{02}$  level contribute to the LIF

signal behind the selector. From the weak LIF signal of benzonitrile molecules in the  $1_{01}$  level in this spectrum it can be deduced that molecules in the  $M=1$  component of this level (as well as of the  $2_{02}$  level) have at least a factor of five lower transmission than the ground state. This nicely demonstrates the degree of selectivity that can be obtained with the present selector as it is seen from Figure 5.8 that the relative difference in the "electric-field-averaged" effective dipole moment of this  $M=1$  component and the ground-state level in the grey-shaded area is less than 10%.

## 5.5 Trajectory calculations

In Figure 5.9 the experimental data shown in Figure 5.3 are compared to the outcome of trajectory calculations. Details on the implementation of the trajectory calculations are given in Subsection 3.2.1 and Subsection 3.2.2. In these calculations a pulse of molecules with an initial length of 4.0 cm (FWHM; Gaussian distribution), with a mean forward velocity of 570 m/s and a velocity spread of 25 m/s (FWHM; Gaussian distribution) is assumed. The initial transverse velocity distributions are described by Gaussian distributions, each with a FWHM of 10 m/s, centered around zero velocity. The switching sequences which are applied in the experiment are used as input and effects due to the fringe fields near the ends of the electrodes of the selector are neglected in the simulations. The voltages applied to the electrodes have been set to  $\pm 9.5$  kV, just as used in the experiment. The electric field dependent dipole moment for the  $0_{00}$  level as shown in Figure 5.8 is taken. In the detection region, molecules in a 2.5 mm high interval are accepted, weighted by the duration that they are in the 2.5 mm diameter cylindrical interaction volume, i. e., assuming that the laser excitation step is not saturated. The number of molecules are plotted as a function of their arrival time (binned in 2  $\mu$ s intervals) and as a function of their velocity component in the  $x$ -direction (binned in 0.3 m/s intervals). To enable a direct comparison with the experimentally observed patterns, the calculated velocity distributions at a given arrival time are convoluted with a Lorentzian profile with a FWHM of 2.2 m/s, thus taking the 8 MHz homogeneous broadening due to the finite lifetime of the electronically excited state, that is inherent in the measurements, into account. Figure 5.9 demonstrates that the experimentally observed patterns are quantitatively reproduced in the simulations, implying that in particular also the transverse velocity distributions of the molecules exiting the selector are correctly described.

The calculated time-integrated and time-resolved number of ground-state benzonitrile molecules transmitted through the selector as a function of the ac switching frequency is shown in Figure 5.10. Also in these calculations, the velocity distributions along the  $x$ -direction at a given arrival time are first convoluted with a Lorentzian profile with a FWHM of 2.2 m/s. Then only the molecules within a 0.5 m/s interval centered around 0 m/s are accepted, thereby mimicking the LIF detection of the molecules in the actual experiment and enabling a direct comparison to the measurements shown in Figure 5.5. In the comparison of the calculated and measured transmission curves shown in the upper row, it should be noted that the vertical scale of either set of curves,

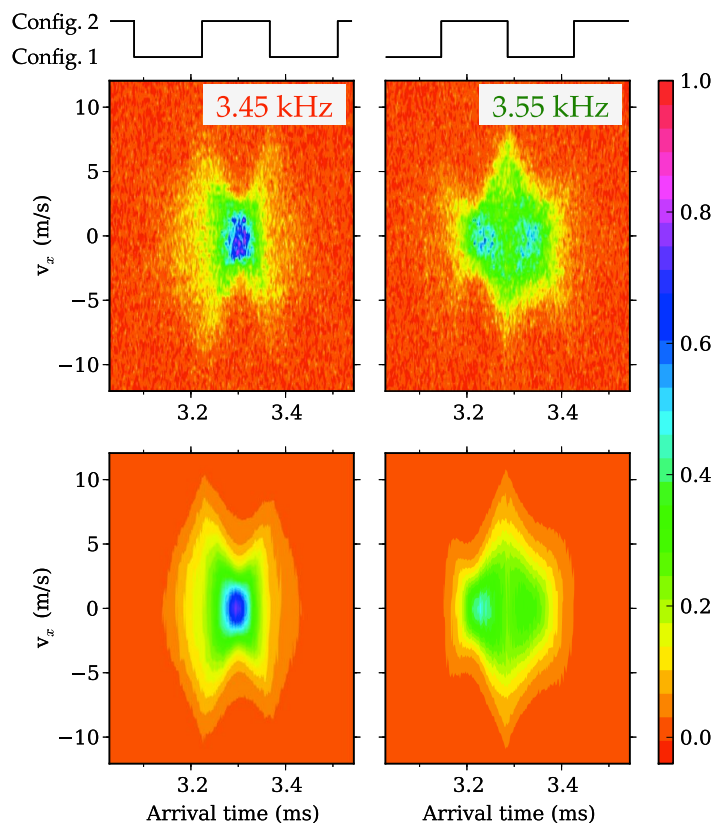


**Figure 5.9:** Upper row: Measured intensity of the LIF signal, plotted in a false-color representation, as a function of the velocity in the  $x$ -direction and as a function of the arrival time for two different ac switching frequencies. Data from Figure 5.3. Lower row: Corresponding simulated arrival time distributions. The calculated velocity distributions are convoluted with a Lorentzian profile with a FWHM width of 2.2 m/s. (See text for details.)

shown on the right and the left, respectively, is normalized to the free-flight intensity. The observed overall transmission of the selector is about a factor of three lower than expected from the calculations. The shapes of the measured and the calculated curves are in good agreement, however. The observed modulations in the transmission curves and the low-frequency onset of the transmission of the selector are well reproduced in the calculations. At the high frequency end the experimentally observed transmission curves drop slightly faster than expected from the simulations. It is well-known, however, that the transmission through the selector under these operating conditions is extremely sensitive to misalignments [32, 64]; fluctuations in the voltages applied to the electrodes might also play a role. Moreover, at these high frequencies the minute losses due to non-adiabatic transitions that might occur each time that the fields are being switched will be most notable. If we assume, for instance, that some 5% of the ground-state molecules

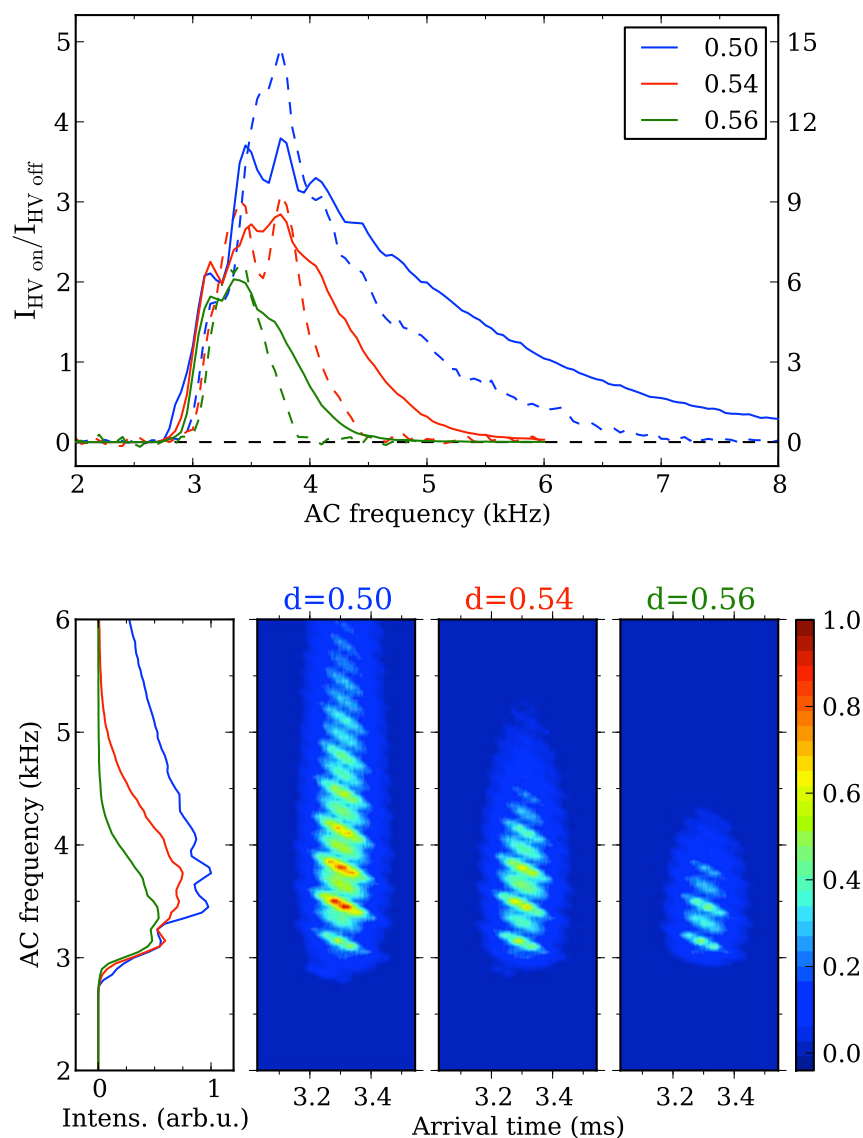


**Figure 5.10:** Upper row: Calculated time-integrated transmission curves for three different duty cycles (solid curves), compared to the corresponding measured curves (dashed curves), already shown in Figure 5.8. The vertical scale for the measured curves is on the left, while the one for the calculated ones is on the right. Lower row: Calculated number of ground-state benzonitrile molecules transmitted through the selector, plotted in a false-color representation, as a function of the ac switching frequency and as a function of arrival time for three different duty cycles. The panel on the left shows the time-integrated signals as a function of ac switching frequency, also shown in the upper row. See text for further details.

are lost to other quantum states each time that the fields are being switched while the molecules are inside the selector, we can bring both the observed overall transmission efficiency and the observed drop in transmission at high ac switching frequencies in perfect agreement with the calculations.

## 5.6 Transmission of molecules in individual $M$ -components

The effective dipole moment of benzonitrile molecules in the rotational ground state is almost constant in the electric fields of the selector, as can be seen in Figure 5.8, which simplifies the interpretation of the shape of the resulting transmission curves. For most of the higher rotational states, however, the effective dipole moment strongly varies with the electric field strength, because avoided crossings with other states of the same symmetry occur. This strongly influences the guiding properties through the selector. In the following, this effect will be exemplified by considering simulated transmission curves of benzonitrile molecules in the individual  $M$ -components of the  $J_{K_a K_c} = 6_{06}$  rotational level. It is necessary to study the transmission of the individual  $M$ -components from simulations, because their energies are degenerate in the field-free LIF detection zone. Therefore, all measured transmission curves shown in this work are in fact averaged over the  $M$ -components of the probed  $J_{K_a K_c}$  states.<sup>2</sup>

In the upper panel of Figure 5.11, simulated transmission curves for all  $6_{06}M$  states are shown. Switching sequences with a fixed end phase of  $0.75\pi$  are used with ac frequencies in the range from 1.5 to 4.0 kHz sampled in steps of 50 Hz. The laser detection is taken into account by assuming a 1 mm diameter laser beam with 2 MHz bandwidth. The weighted average of the individual curves is calculated by taking the degeneracies of the components into account. It is clearly seen in the lower panel that the onset positions of the transmission curves for the  $M=2, \dots, 6$  components appear arranged in ascending order with respect to their  $M$  quantum number at a nearly equidistant spacing of 0.17 kHz, indicating that the effective dipole moments of the states increase with  $M$  as well. This scheme evidently does not hold for the states with  $M=0, 1$ . The onset of the  $M=0$  state's transmission curve occurs at 2.5 kHz while the onset for the  $M=1$  state is located at a lower ac frequency of 1.5 kHz.

In order to investigate this behaviour, the calculated effective dipole moments of the  $J_{K_a K_c} M=6_{06}M$  quantum states are shown in the upper panel of Figure 5.12 as a function of the electric field strength. For comparison, the effective dipole moment of the ground state is depicted as dashed grey curve. The horizontal axis in the figure is chosen such as to include the minimum and maximum electric fields that are typically sampled by the molecules (see Figure 3.3). At field strengths above 48 kV/cm, that is above the electric field present on the molecular beam axis indicated by a dashed vertical line, the effective dipole moment curves of all considered states are nearly linear and run almost parallel.

<sup>2</sup>The degeneracy could, in principle, be lifted by applying a suitable electric field in the detection region. This can be achieved by placing small capacitor plates or wire grids around the interaction point of laser and molecular beam (an example may be found in reference 94). Due to the increased stray light some further modification to the detection setup would be needed, e. g., detecting the LIF photons along the forward direction of the molecular beam.

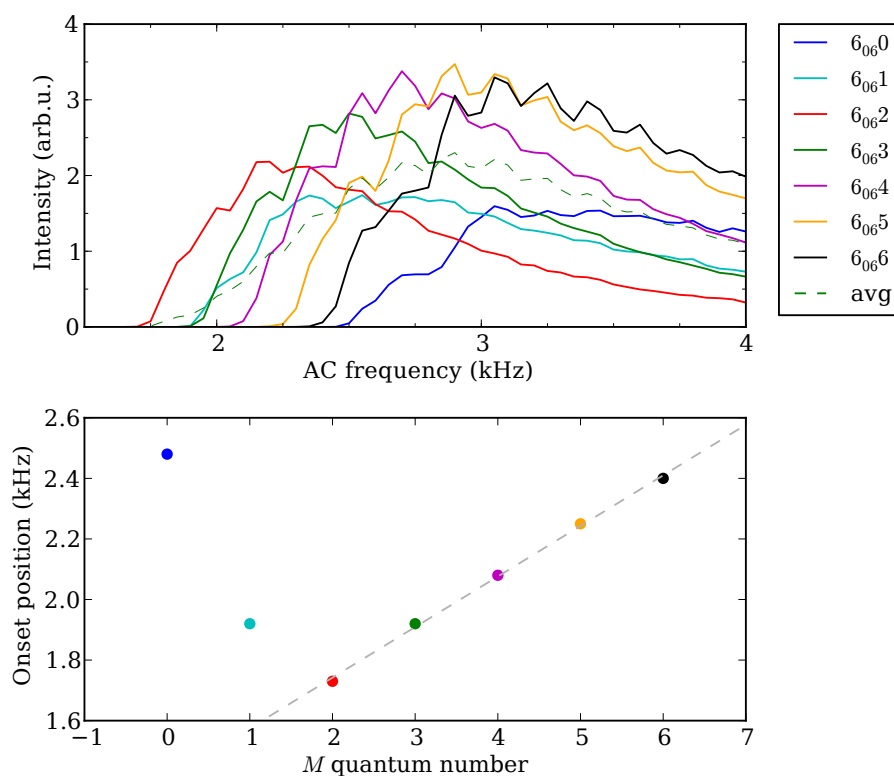


**Figure 5.11:** Upper panel: Calculated transmission curves for the  $M$ -components of the  $6_{06}$  rotational level of benzonitrile. Lower panel: Onset position of the transition curves in the upper panel as a function of the  $M$  quantum number. The dashed line is a guide to the eye.

The effective dipole moments of the states with  $M=2, \dots, 6$  increase as a function of  $M$  in this field range. This behavior extends to the fields below 48 kV/cm, but the effective dipole moments change rapidly at some different lower electric-fields values except for the  $6_{06}6$  state whose curve runs almost as smoothly as the curve for the  $0_{00}$  state. To illustrate the origin of the steps, the Stark curves of the  $6_{06}M$  states are shown in the lower panel of Figure 5.12. At the electric field strength at which a step occurs, the Stark curve is bend due to an avoided crossing between a Stark curve of same symmetry.

In the harmonic approximation for AG focusing discussed in Section 3.1, a constant effective dipole moment is assumed in the electric focusing fields. This assumption is nearly valid for the rotational ground-state and  $6_{06}6$  levels near the electric field present at the molecular beam axis, but it is clearly invalid for the other  $6_{06}M$  states because of the steps occurring on the effective-dipole-moment curves at lower electric field. The ac frequency for optimal focusing is different on both sides of a step. The ac frequency at which the highest transmission is expected can only be obtained from simulated or experimental transmission curves, in contrast to the analytical description for molecules

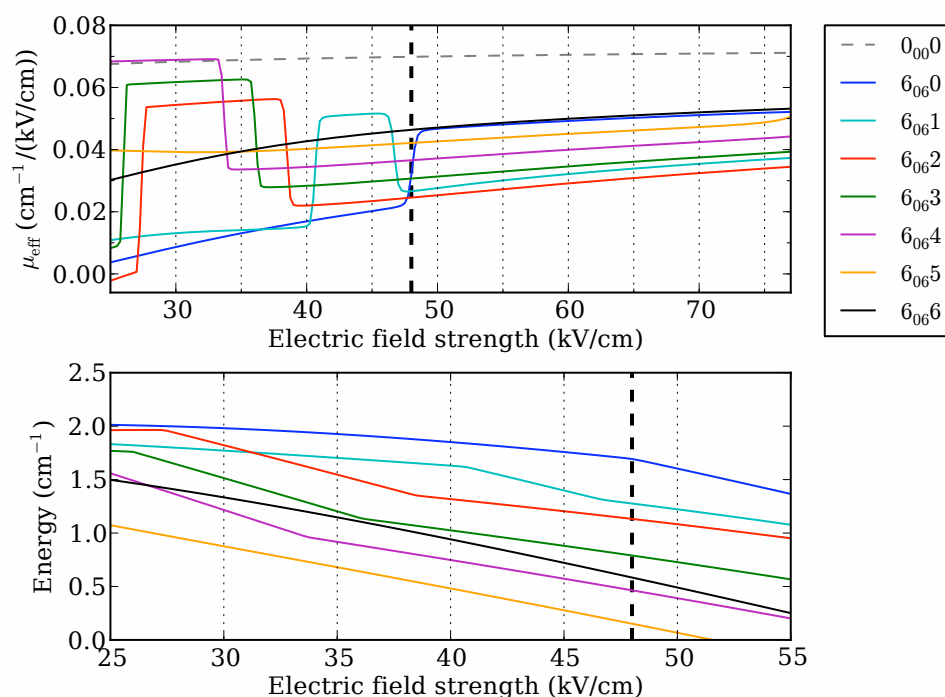


**Figure 5.12:** Upper panel: Calculated effective dipole moments of the  $M$ -components of the  $6_{06}$  rotational level of benzonitrile as a function of the electric field strength which is sampled in steps of  $0.5 \text{ kV/cm}$ . The dashed grey curve depicts the effective dipole moment of the ground state and the dashed vertical line indicates the electric field on the molecular beam axis. Lower panel: Calculated Stark energies as a function of the electric field.

which have quantum states with a linear Stark effect.

The guiding efficiency for the  $6_{060}$  state is expected to be rather low, because a step of its effective dipole moment curve occurs right at the electric field present on the molecular beam axis. At higher electric fields the curve is almost similar to that of the  $M=6$  component, while in fields below the step the effective dipole moment is the smallest among the  $6_{06M}$  states. The onset position of the transmission curve is even somewhat higher than for the  $M=6$  component, indicating that the high-field side determines the optimal ac frequency. This assumption is strengthened by considering the  $M=1$  component for which a step of the effective dipole moment occurs close to the field strength on the molecular beam axis as for the  $M=0$  component, but in the opposite direction. In the high-field region, the effective dipole moment of the  $M=1$  component is comparatively small and, as expected, the onset of its transmission curve occurs at a relatively low ac frequency.

The position of the step relative to the field strength on the beam axis also determines the highest obtained signal in the transmission curve. The peak intensity in the curve for the  $6_{060}$  state is about 50% smaller than for the curves of the  $M=5,6$  components.

By combining Figure 5.12 and Figure 5.11 it is seen that the smaller the distance from a step to the electric field on the beam axis the smaller the peak signal in the transmission curve.

## 5.7 Resolution

The good agreement between the observed and calculated performance of the  $m/\mu$ -selector is not only a testimony to the accurate mechanical design of the selector, but it also implies that trajectory calculations can be used to predict the outcome of future experiments. In the present selector, the number of full switching cycles that the molecules experience near optimum transmission is only about ten, which poses an intrinsic limitation to the attainable  $\mu/\Delta\mu$ -resolution. Nevertheless, the calculated transmission curves shown in Figure 5.13 predict that for molecules with the mass of benzonitrile and with an effective dipole moment of 4.5 Debye, the selector can be operated such that the overall transmission for levels with a constant effective dipole moment differing by 5% can be made to differ by a factor of two; when the  $\mu/\Delta\mu$ -resolution is defined in this way, a value of 20 is obtained. If a beam containing mainly the species with the lower dipole moment of the two is desired, the selector can operate below the low-frequency cut-off for the other species at a duty cycle of 0.50. A beam predominantly containing the species with the largest dipole moment of the two can only be obtained at higher frequencies and at higher (or lower) duty cycles, thereby necessarily reducing the overall transmission somewhat.

## 5.8 Transmission vs. field strength

The shape of a transmission curve depends on several parameters. Besides the Stark effect of the molecular quantum state, the duty cycle, the effects of start and end phases, and the electric field geometry, the transmission characteristics are strongly influenced by the electric potentials applied to the selector. This is demonstrated in the upper panel of Figure 5.14, where transmission curves for ground-state benzonitrile molecules are shown that are obtained at high voltages in the range from  $\pm 1.0$  to  $\pm 9.5$  kV and at a fixed end phase of the switching sequences of  $0.75\pi$ . During the measurements, the nozzle was heated to 65 °C. As seen from this graph, the curves are shifted towards lower switching frequencies when lower voltages are applied. The frequency of highest overall transmission is plotted in the middle panel of Figure 5.14 as a function of the applied high voltages. A fit using a second order polynomial is shown as well. From this the voltages needed for a certain peak frequency can be deduced.

As seen from the peak heights in the upper panel, the transmission of molecules through the selector increases with the applied high voltages. To compare the measured intensities, the spectrally integrated intensities of the  $1_{11} \leftarrow 0_{00}$  transition are shown in the lower panel for the switching frequencies that give the highest intensity. The spectral integration gives a better estimate of the number of molecules in the detection region as the transverse velocity components of the packet after leaving the selector depend on

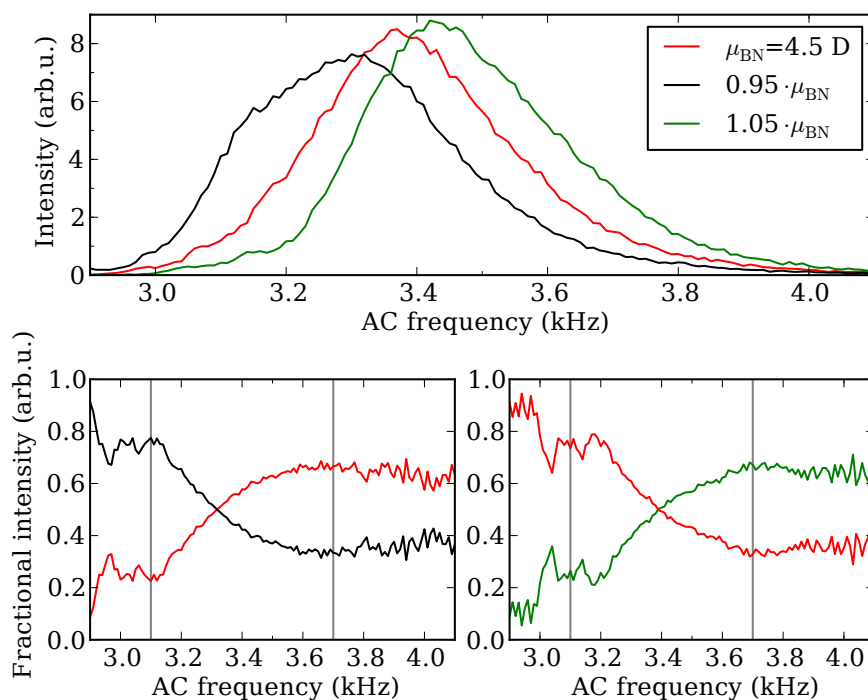


**Figure 5.13:** Upper panel: simulated transmission curves for benzonitrile molecules with a constant effective dipole moment of  $\mu_{\text{eff}}=4.5$  Debye and  $\mu_{\text{eff}}$  changed by  $\pm 5\%$ . Lower panels: fractional intensities of the curves in the upper panel for  $\mu_{\text{BN}}$  and one of the other effective dipole moments. The fractional intensity is obtained by dividing the transmission curve of a species by the sum of the transmission curves of the two compared species. Vertical lines indicate ac frequencies at which the transmission of the two species in each panel differs by at least a factor of two.

the applied field strengths. A linear dependence of the overall molecular density on the high voltages is indicated by the linear fit depicted as red line in the figure.

The obtainable intensities are limited by the applicable high voltages in the experiment. In the linear approximation, increasing the peak intensity obtained at  $\pm 9.5 \text{ kV}$  by 50% would require high voltages of about  $\pm 14 \text{ kV}$ . The resulting maximal field strength of nearly  $200 \text{ kV/cm}$  at the electrode surfaces is likely to cause flashovers in the current state of the electrodes and a better polishing/conditioning would be needed.

## 5.9 Phase effects

At a fixed beam velocity and a fixed ac switching frequency, the start and end phase cannot be changed independently. This is because the electric field can be switched *between* two configurations but not be switched *off* in the current setup. As a result, the two phases are explicitly determined by the chosen burst delay, i. e., the time between the

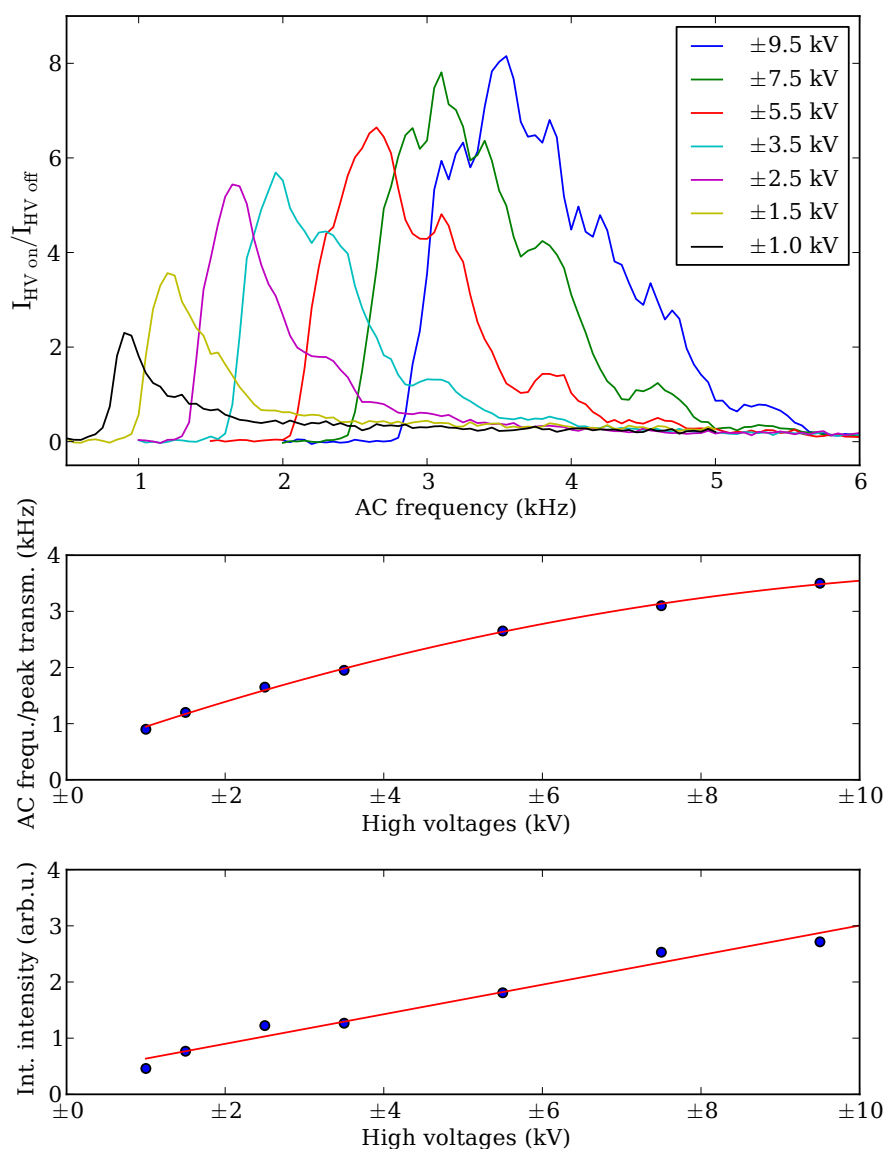


**Figure 5.14:** Upper panel: Transmission curves for ground-state benzonitrile molecules, obtained with high voltages in the range from  $\pm 1$  to  $\pm 9.5$  kV (duty cycle 0.5, end phase  $0.75\pi$ ) applied to the selector. Middle panel: switching frequencies of maximum transmission in the individual transmission curves and second order polynomial fit (red line). Lower panel: spectrally integrated intensity at maximum of individual transmission curves and linear fit (red line).

nozzle trigger and the beginning of the switching sequence. By scanning the burst delay, a combination of start and end phase can be found that gives the highest transmission. This and how the effect of the start phase on the transmission can be increased is shown

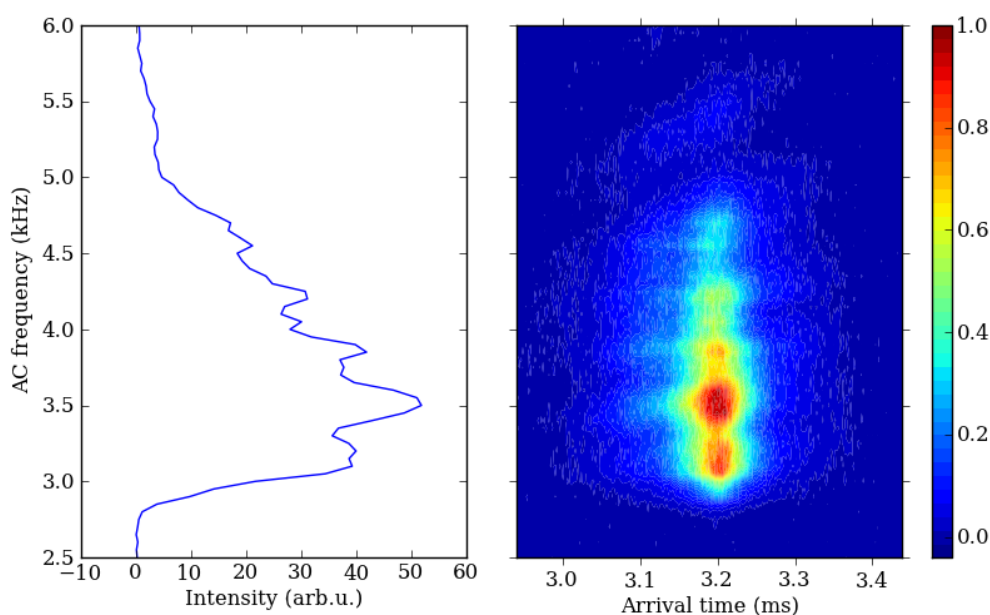


**Figure 5.15:** Left panel: Transmission curve for ground-state benzonitrile molecules measured at a fixed end phase of  $0.75\pi$  for ac frequencies between 2.5 and 6 kHz. The signal for each ac frequency is obtained by time-integrating the arrival-time distribution shown in the right panel. The arrival time is given relative to the nozzle trigger and the nozzle was heated to  $65^\circ\text{C}$  during the measurements.

in the first part of this section for benzonitrile molecules in their ground state.

In the second part, a method is presented to determine the velocity of the molecular beam using start and end phases by comparing experimental transmission curves to trajectory simulations.

### Effect of the start phase

To determine the effect of the start phase on the transmission, ac-frequency scans with a constant end phase are performed, thereby eliminating effects of the end phase on the LIF intensity. In Figure 5.15, TOF profiles are shown corresponding to the upper panel in Figure 4.7. The fact that the arrival time at which the maximum intensity is observed, 3.2 ms, coincides with the arrival time of the center of the packet during free flight, proves that the condition of a constant end phase is fulfilled for all ac frequencies. The transmission curve that is shown on the left side of Figure 5.15 is obtained by time-integrating the intensities in the right panel for each ac frequency. From that, the observed modulation on the transmission curve can be attributed to the varying start phase as the ac frequency is scanned.

The start/end-phase combination that gives the highest signal is found by scanning the burst delay, thereby scanning the time at which the molecules enter the selector. Such

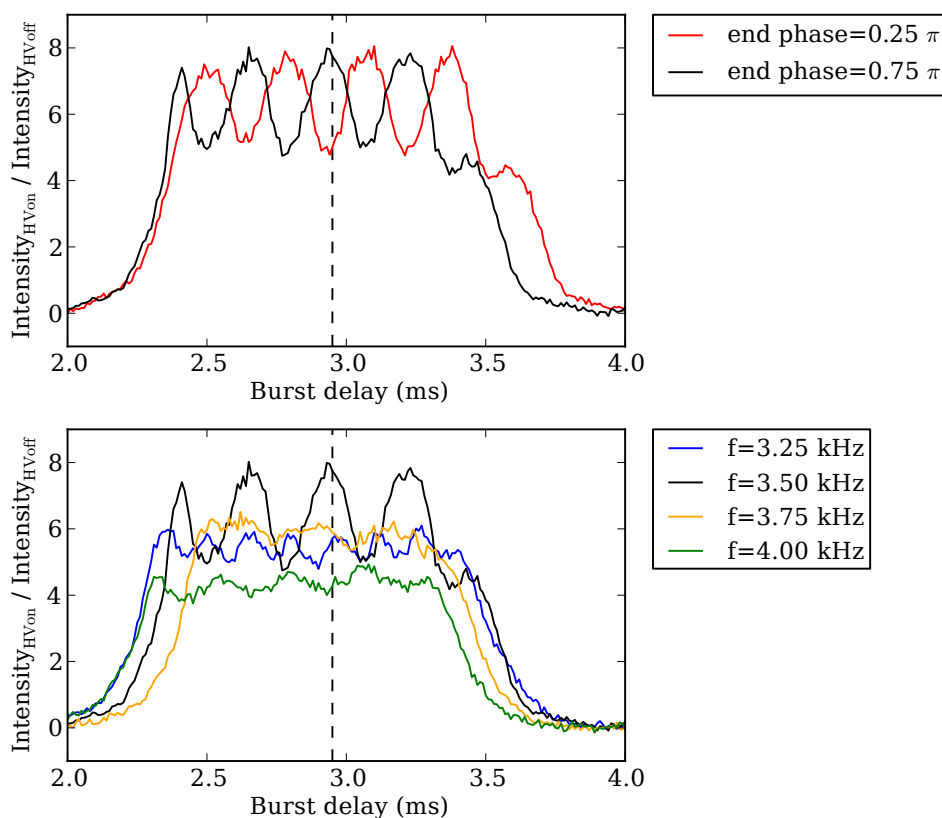


**Figure 5.16:** Time-integrated LIF intensities obtained as a function of the burst delay. Upper panel: measurements for 3.5 kHz, duty cycle  $d=0.5$ , and two different end phases,  $0.25\pi$  and  $0.75\pi$ . Lower panel: Delay scans for burst sequences with different ac switching frequencies.

measurements for ground-state benzonitrile molecules are shown in the upper panel of Figure 5.16 using the same switching sequences as before. The time-integrated LIF signal is recorded as the burst delay is scanned from 2 to 4 ms and the dashed vertical line at 2.91 ms indicates the burst delay chosen in the previous measurements in Figure 5.15 at which the central part of the molecular packet leaves the selector during the middle of a horizontal focusing phase. In all traces a sharp onset is seen at 2 ms, followed by several oscillations of the signal and a drop back to zero intensity near 4 ms. At burst delays for which no intensity is observed, the molecular packet is either already inside the selector when the switching sequence starts or is still inside the selector when the switching sequence ends. In both cases, the packet is overfocused or defocused in the constantly applied field configurations near one of the ends of the selector and no molecules in the probed quantum state reach the detection region.

The upper panel shows two measurements at  $f=3.5$  kHz which give the highest signal in Figure 5.15. While one trace is obtained at an end phase of  $0.75\pi$  occurring at

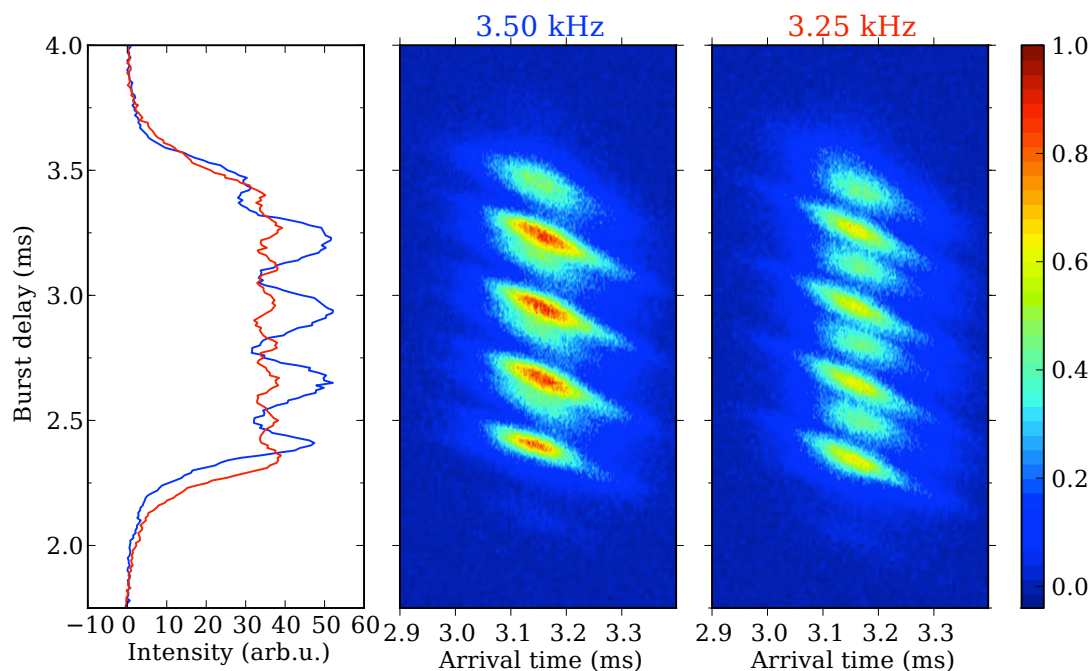


**Figure 5.17:** Middle and right panels: Burst-delay dependent arrival-time distribution of ground-state benzonitrile molecules at the indicated ac frequencies. The false-color representation is normalized to the maximum intensity in both panels. Left panel: Time-integrated intensities of the distributions in the other panels.

2.91 ms burst delay as described above, an end phase of  $0.25\pi$  is used for the other trace. Effectively, the two applied switching sequences are phase shifted relative to each other by half a period length. This becomes clear, as the maxima in the oscillations appear every  $T=286\ \mu\text{s}$ , thereby corresponding to the ac frequency ( $T=1/f$ ), and the maximum in one trace occurs at the same time as a minimum in the other. Choosing the right burst delay is important, because the molecular signal is decreased from the maximum by up to  $1/3$  for a certain start/end-phase combination. This signal difference is smaller at other ac frequencies as shown in the lower panel. As an illustration, the underlying arrival-time distributions for the measurements with end phase  $0.75\pi$  and  $f=3.5$  and  $4.0$  kHz are shown in Figure 5.17.

In the lower panel of Figure 5.16, the trace for an end phase of  $0.75\pi$  from the upper panel is shown again together with measurements obtained under similar conditions but at different ac frequencies in the range from 3.25 to 4.00 kHz. The observed modulation is clearly the highest at 3.5 kHz, indicating that the choice of the optimal phase combination for efficient focusing is most critical near the maximum of the transmission curve.

### Velocity determination

The velocity of a pulsed molecular beam mostly depends on the carrier gas. From argon gas, for example, beam velocities on the order of 600 m/s are typically obtained. Furthermore, the nozzle temperature and operation parameters influence the velocity on a smaller scale [95]. The beam velocity can be obtained directly from time-of-flight (TOF) profiles of the packet measured at different positions along the molecular beam axis of which the distance is known. Microphones have been used for this purpose [96] and LIF detection can also be performed between skimmer and entrance of the selector in addition to the LIF zone already installed near the end of the selector. As the access to the beam axis close to the skimmer is very limited, LIF detection is challenging at this position, because massive stray light from reflections on the electrode surfaces nearby are to be expected. There is also the risk of scratching the electrodes when inserting a microphone into this small space.

In this section, a method is described to determine the velocity of the molecular beam. It is based on the coupled start and end phases in the guiding process and does not require knowledge about the exact distances from nozzle and laser beam to the respective ends of the selector. The only, purely technical requirement is the movability of the nozzle in a transverse direction, for example, by mounting it to a translation stage.

The burst delay needs to be adjusted such that the center of the molecular packet leaves the selector during the middle of a focusing phase for all ac frequencies similar to Figure 5.15. In corresponding simulations the end phase can be controlled precisely, because the beam parameters are exactly known. For a more clear identification of the peaks on the transmission curves, the contrast can be increased by shifting the nozzle transversely. This way the effect of the start phase is amplified, because the conditions for the initial focusing of the beam entering the selector into the selector are more critical for an efficient incoupling and transmission. In the experiment, the nozzle is preferentially shifted in the vertical direction to avoid that the molecular packet exits the selector with a velocity component in the direction of the laser beam. In the simulations, the initial vertical position of the molecular packet is chosen accordingly.

In Figure 5.18, simulated transmission curves for beam velocities in the range from 615 to 630 m/s are shown. In each simulation the burst delay is adjusted to the velocity for a fixed end phase of  $0.75\pi$ . The ac frequency is scanned from 2 to 7 kHz in steps of 50 Hz. To achieve a modulation which compares to the experiment, the initial molecular packet is vertically centered at  $y=1.5$  mm. It is seen that the positions of the resulting peaks on the transmission curves change with the beam velocity.

The experimental transmission curve (blue trace) is shown together with the simulations. It is obtained while the nozzle is shifted upwards from the beam axis by 1 mm using the switching sequences from the simulations and a burst delay chosen for a fixed end phase of  $0.75\pi$  as in the simulations. Vertical lines indicate the positions of the peaks on the transmission curves as a guide to the eye for comparison to the simulations. The best agreement is seen for velocities of 620.0 and 622.5 m/s. The peak positions in the other simulations do clearly not match the experiment, so it can be concluded that the beam velocity is about 620 m/s with an uncertainty of less than 5 m/s

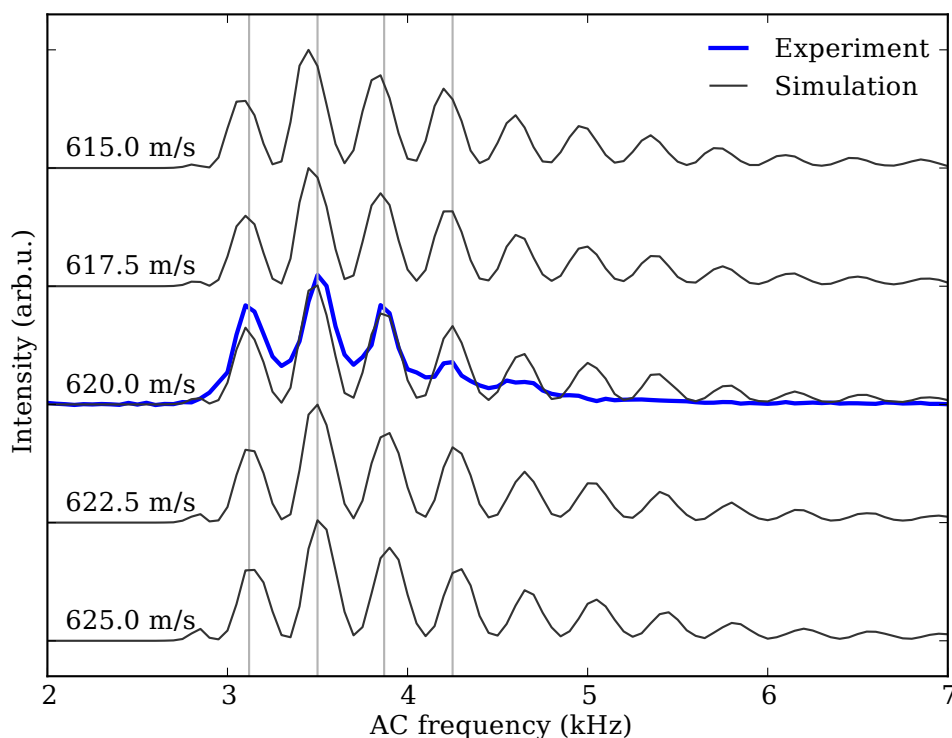


**Figure 5.18:** The thick blue trace shows an experimental transmission curve for ground-state benzonitrile molecules at a fixed end phase of  $0.75\pi$ . The ac frequencies at the center of the observed peaks are indicated by grey vertical lines. Corresponding simulations for different beam velocities are shown as grey traces (offset for clarity). To amplify the effect of the start phase the nozzle is shifted by 1 mm (1.5 mm) in the  $y$ -direction in the experiment (simulation).

or 1%. This velocity is slightly higher than what is expected for a mono-atomic ideal gas,  $v_p = \sqrt{5k_B T_0 / m_{\text{Argon}}} = 603 \text{ m/s}$  with the Boltzmann constant,  $k_B$ , and the nozzle temperature,  $T_0 = 350 \text{ K}$  [3]. However, a similar elevation over the expected mono-atomic velocity at room temperature has been assumed in Subsection 4.1.2.

## 5.10 Conclusions

A state-of-the-art  $m/\mu$ -selector for large molecules has been demonstrated and characterized using a pulsed beam of benzonitrile molecules. In combination with detection using a narrowband continuous wave laser, the quantum-state-specific transmission of the selector as well as the transverse velocity distribution of the molecules exiting the selector have been measured as a function of the ac switching frequency. It has been shown that by controlling the applied ac waveforms, a  $\mu/\Delta\mu$ -resolution can be obtained that is sufficient to exclusively transmit molecules in quantum states that have the same

$m/\mu$ -value as the rovibronic ground state of benzonitrile. The measured transmission characteristics of the  $m/\mu$ -selector are generally in good agreement with the outcome of trajectory simulations. At high frequencies the observed transmission is smaller than expected; it is well-known, however, that the transmission through the selector under these operating conditions is extremely sensitive to misalignments [32, 64]. Fluctuations in the voltages applied to the electrodes might also play a role. Moreover, at these high frequencies the minute losses due to non-adiabatic transitions that might occur each time the fields are switched will become nonnegligible. Finally, it has been demonstrated how phase effects in the guiding process can be used to obtain the velocity of the molecular beam from trajectory simulations.

## Chapter 6

# Alternating-gradient focusing of the benzonitrile-argon van der Waals complex<sup>1</sup>

In this chapter, alternating-gradient (AG) focusing of the benzonitrile-argon van der Waals complex is discussed. The dipole moment of the complex, which remained unstudied to date, is found to be the same as for the benzonitrile monomer by comparing the experimental and simulated transmission characteristics of the two species. Both species are present in the molecular beam and it is shown that selective transmission of each can be achieved. In this way,  $\mu/m$ -selective transmission is demonstrated for molecules with different *masses*,  $m$ , but the same *electric dipole moment*,  $\mu$ , whereas the separation of quantum states shown in Chapter 5 is based on different *dipole moments* of the same *molecule*.

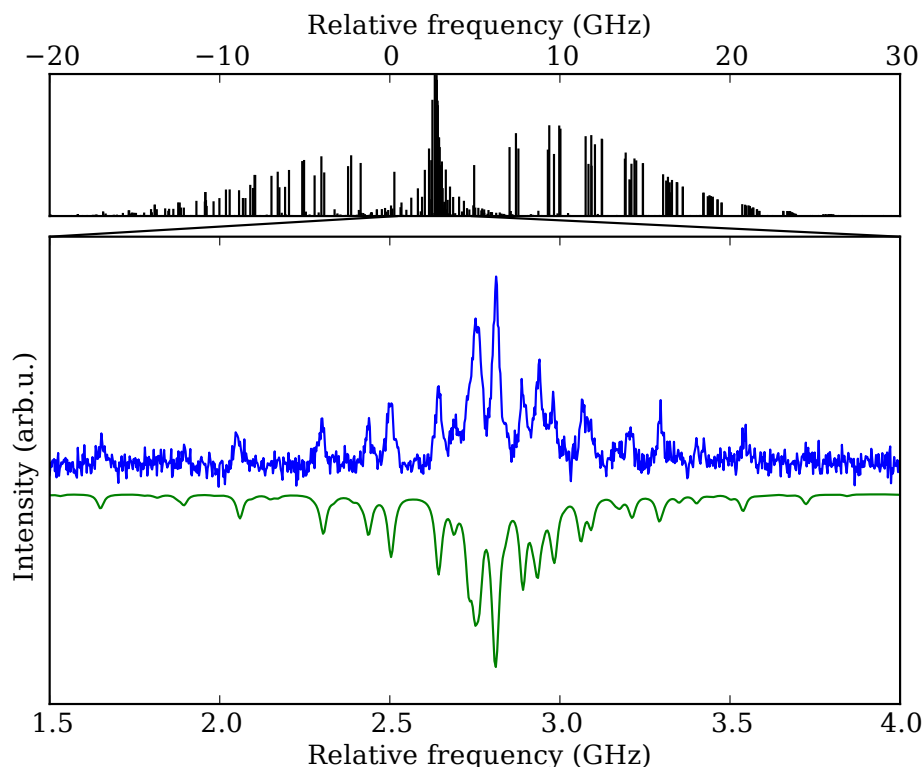
### 6.1 LIF spectra and discussion

Figure 6.1 shows part of the rotationally resolved  $S_1 \leftarrow S_0$  electronic fluorescence excitation spectrum of the benzonitrile-argon complex (the same spectrum spanning over a wider frequency range is shown Figure 6.6). The experimental spectrum in the lower panel is obtained with the selector operating at 2.8 kHz. The UV-laser frequency is scanned in steps of 2 MHz near the band origin of the electronic transition at  $36\,489.16\text{ cm}^{-1}$ . The recorded frequency range is chosen to include the strongest rotational transitions in the Q-branch. At each step, the detected LIF photons from 80 consecutive molecular beam pulses are integrated (2 s). Despite the high resolution of the laser system, not all rotational transitions can be resolved in the Q-branch because of the high density of rotational lines. A simulation of the spectrum using the known molecular constants [58, 61] with the PGopher program [62] is shown in the upper panel and a 0.8 K rotational temperature, an adjustable parameter in the simulation, is used. In the lower panel, the simulated spectrum is shown, convoluted with a Voigt profile. We assume that the natural line width of the transition is the same as for benzonitrile which results in a Lorentzian contribution of 8 MHz to the line shape. A Gaussian contribution of 21 MHz is obtained from a fit to the experimental spectrum. This Gaussian contribution is mostly due to a 15 MHz Doppler broadening resulting from the transverse velocity distribution of the molecules leaving the focuser, which is 4 m/s according to trajectory

---

<sup>1</sup>This chapter is based on reference 60.

simulations. In order to make the effect of transverse forces near the end of the device on the LIF detection similar in all measurements presented in this chapter, the applied switching sequences are arranged such that molecules in the middle of a pulse leave the selector, when the switching cycle is in the middle of a vertical focusing phase [87].



**Figure 6.1:** Upper panel: Simulation of the rotationally resolved fluorescence excitation spectrum of the complex at a rotational temperature of 0.8 K. The  $ac$ -hybrid spectrum has 93%  $c$ -type and 7%  $a$ -type contributions. Lower panel: Part of the experimental spectrum obtained at 2.8 kHz switching frequency, and, plotted upside down, simulated spectrum convoluted with a Voigt profile. See text for details.

The peak intensities in the spectrum depend on the ac frequency as can be seen from the spectra measured for different ac frequencies shown in Figure 6.2. A weak LIF signal is obtained in free flight (black bottom trace), i. e., when ground potential is applied to the electrodes of the selector and only the strongest transitions (near 2.75 GHz) are clearly observed. Here, the Doppler broadening contributes less than 4 MHz to the line width, because the maximum transverse velocity for molecules that reach the detection region is limited by the geometry of the experimental setup [87]. When the molecules are guided through the selector by applying switched high voltages to the electrodes, the signal is significantly increased. In the spectra obtained with ac frequencies in the 2.25–3.0 kHz range, several distinct peaks are seen and the overall strongest signal is observed at 2.75 kHz. Two peaks in the spectra, labeled (A,B), assigned to the  $4_{13} \leftarrow 4_{23}$  and

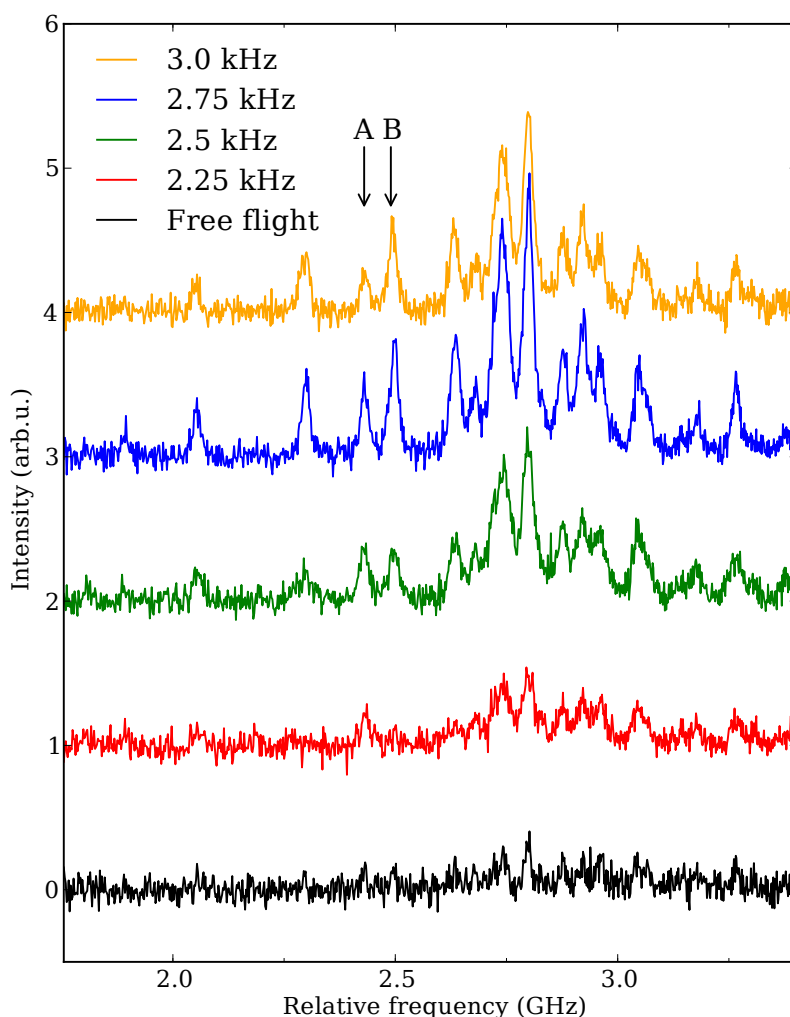


**Figure 6.2:** Rotationally resolved fluorescence excitation spectra of benzonitrile-argon (offset for clarity). The black bottom spectrum has been obtained at free flight, i.e., without high voltages applied to the selector. The other spectra have been obtained with the selector operated at the indicated ac switching frequencies. The laser frequency is given relative to the  $S_1 \leftarrow S_0$  vibronic origin transition at  $36\,489.16\text{ cm}^{-1}$ . Transitions that contribute to the indicated peaks:  $4_{13} \leftarrow 4_{23}$  and  $6_{24} \leftarrow 6_{34}$  (A) (ratio 3:1) and  $2_{02} \leftarrow 2_{12}$  (B).

$6_{24} \leftarrow 6_{34}$  transitions (peak A, contributing to the line strength at a 3:1 ratio) and the  $2_{02} \leftarrow 2_{12}$  (B) transition, illustrate the dependence of the peak height on the ac frequency. At 2.25 kHz A is strong while B is completely suppressed. In increasing the ac frequency to 3.0 kHz, B gains intensity faster than A until B is the strongest. It is evident from this behavior that molecules in the initial quantum levels contributing to A

have lower effective dipole moments than states that contribute to B (see Section 6.2). As a result, the contributions from individual  $M$ -components of the  $J_{K_a K_c}$  states to the observed transitional lines are changed in the guided beam compared to the free flight. In this regard it is remarkable that the experimental spectrum is still described well by the (free-flight) simulation at 0.8 K, albeit that the role of the rotational temperature is reduced to that of an effective parameter.

## 6.2 Frequency-dependent transmission curves and discussion

The transmission efficiency for a  $J_{K_a K_c} M$  quantum state in the guiding process depends on the ac frequency, similar to the transmission of ions in the quadrupole mass filter. This dependence is depicted in Figure 6.3, where the measured LIF intensity is shown as a function of the ac switching frequency for benzonitrile and the complex in their respective rotational ground states. To obtain these transmission curves, the laser frequency is kept fixed at the center of the  $1_{11} \leftarrow 0_{00}$  (monomer) and  $1_{10} \leftarrow 0_{00}$  (complex) transitions. The ac frequency is scanned in steps of 50 Hz in the 1.5–6 kHz range and the detected signal from 80 consecutive molecular pulses is integrated. For better comparison, the signal from the complex is scaled up 70-fold.

The relative density of benzonitrile and the complex in the molecular beam,  $\rho_{\text{BN}}/\rho_{\text{BN-Ar}}$ , can be estimated from this scaling factor under the following assumptions. The guiding efficiencies for the ground states of the two species are similar and the 1.8 K rotational temperature seen for benzonitrile for free flight is the same for the complex, resulting in a fractional population of the ground state that is 4.1 times higher for benzonitrile than for the complex. Both considered rovibronic transitions have equal line strengths, because there is only one allowed transition from each of the rotational ground states of the respective initial  $S_0, v=0$  levels. As a result, the relative density is estimated to:  $\rho_{\text{BN}}/\rho_{\text{BN-Ar}} \approx 70 / 4.1 = 17$ .

It is seen from the obtained curves in Figure 6.3 that transmission of molecules is suppressed at low ac frequencies, and, in going to higher frequencies, a steep onset occurs that is followed by a gradual decrease in intensity. The position of the onset indicates the lowest ac frequency at which the AG principle works for molecules in the corresponding quantum state, leading to stable trajectories that extend to the end of the selector. The position critically depends on the geometry and strength of the electric fields in the selector as well as on the effective dipole moment of the molecular quantum state and on the mass. In the lower two panels of Figure 6.3, the onsets of the transmission curves from the upper panel are shown on an expanded horizontal scale, and the outcome of trajectory simulations are depicted as black traces. The simulations are based on the experimental switching sequences and on Stark-energy calculations based on the rotational constants [56, 61] using the *libcoldmol* program [54]. In the calculations, the permanent electric dipole moment of benzonitrile, oriented along the monomer  $a$ -axis, is taken for both species:  $\mu_{\text{BN}} = \mu_{\text{BN-Ar}} = 4.52$  D. We assume that the dipole moment in the complex is still aligned along the symmetry axis of the benzonitrile monomer, but due to the changed mass distribution in the complex,  $\vec{\mu}_{\text{BN-Ar}}$  is not aligned along a principal

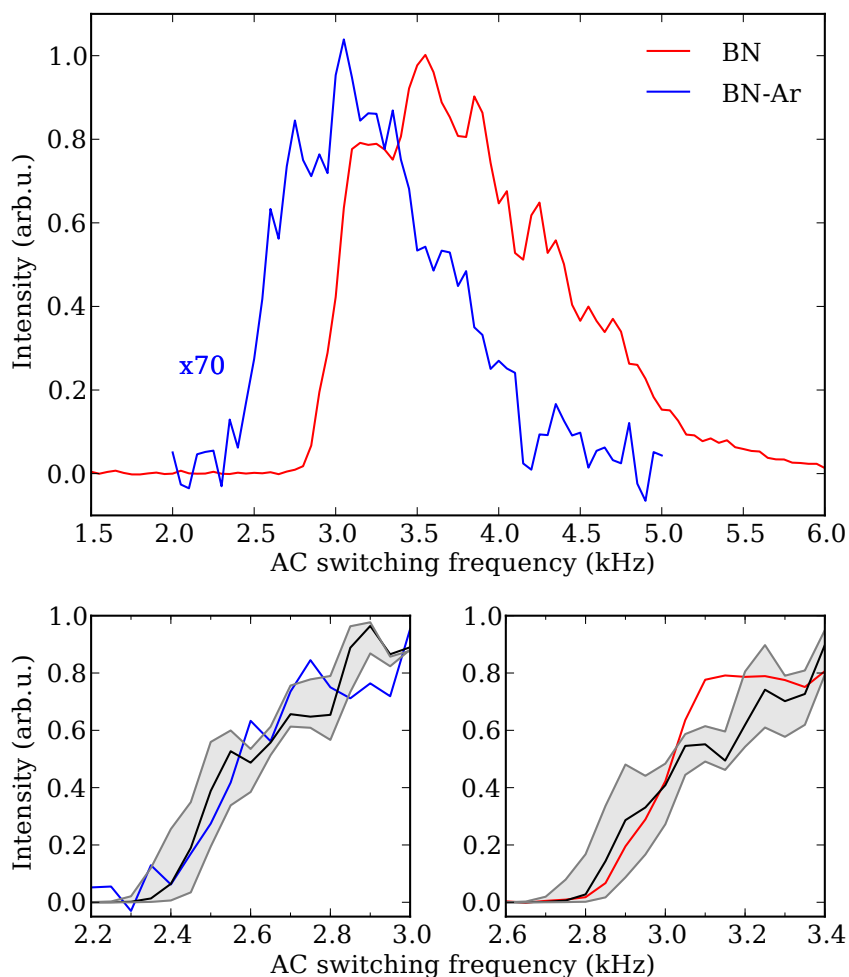


**Figure 6.3:** Time-integrated LIF signal intensity as a function of the ac switching frequency for benzonitrile (red curves) and the argon complex (blue curves). The laser frequency is kept fixed at the center of the  $1_{11} \leftarrow 0_{00}$  ( $1_{10} \leftarrow 0_{00}$ ) transitions of benzonitrile (the complex) and the complex-signal is scaled up 70-fold for better comparison. Lower panels: onsets of the curves in the upper panel, plotted on an expanded scale, together with calculated curves (black) for molecules with dipole moments of  $\mu=4.52$  D and  $\mu \pm 5\%$  (grey curves).

axis anymore. The resulting  $13^\circ$  tilt of the dipole moment relative to the  $b$ -axis away from the argon atom is included in the calculation and all rotational states with  $J \leq 25$  ( $J \leq 30$  for the complex) are considered.

For both benzonitrile and the complex, the shape of the onset is not perfectly reproduced by the trajectory simulations, but the simulated and measured cut-off frequencies agree very well. In order to study the dependence of the onset position on the magnitude of the dipole moment, the trajectory simulations are repeated with Stark energies calculated from  $\mu_{\text{BN-Ar}} = \mu_{\text{BN}}$  changed by  $\pm 5\%$ . Grey traces depict the resulting simulated transmission curves and the area between these curves is shaded in grey. Simulations in which the tilt of the dipole moment is varied by  $\pm 13^\circ$  (not shown) do not exhibit such shift of the onset position. From the shifts of the onset position that occur when changing the value and orientation of the dipole moment, we conclude that the permanent dipole moment is the same for benzonitrile and the complex to within  $\pm 5\%$ .

In Figure 6.4, the Stark energies and effective dipole moments calculated above are depicted for all rotational states of benzonitrile and the complex with  $J \leq 2$ . The upper (lower) row shows the energy (effective dipole moment) as a function of the electric field strength. Red curves are used for benzonitrile and blue curves for the complex. The grey curves in all four panels depict the species shown in the other column, and the dashed horizontal lines in the lower row show the permanent dipole moment of benzonitrile. Calculations show that at the relevant field strengths – above 20 kV/cm – the Stark energies of the complex and its density of states are larger on average than for benzonitrile. This effect is due to the smaller rotational constants of the complex and results in effective dipole moments that, in going to higher field strengths, converge more rapidly to the permanent dipole moment than for benzonitrile.

In a molecular beam that consists only of benzonitrile and the complex, both at a rotational temperature below 20 mK, only the ground states of the two species are populated. In this case, transmission through the selector can be restricted to the complex alone, when an ac frequency is chosen below the onset of the benzonitrile transmission curve in Figure 6.3, e.g., at 2.7 kHz. Alternatively, a pure benzonitrile beam is obtained by suppressing the transmission of the complex at a 4.5 kHz or higher switching frequency.

However, the typical rotational temperature in a supersonic molecular beam is on the order of 1 K at which the population of large molecules is distributed over many rotational levels. Therefore, the fraction of ground-state molecules is relatively low. As shown in Figure 6.4, the effective dipole moments  $\mu_{\text{eff}}$  of higher rotational levels are equal to or smaller than for the ground state inside the electric fields of the selector. In order to achieve the same focusing for a smaller  $\mu_{\text{eff}}$ , the time spent in each of the two field configurations must be longer, i.e., the switching frequency must be lower. This is the rationale for peak A in Figure 6.2 becoming stronger relative to peak B at low ac frequencies. As a result, the transmission curve for a rotational level either coincides with the ground-state curve or is shifted to lower switching frequencies. This implies that also in a thermal beam transmission of the complex can be suppressed by choosing a 4.5 kHz switching frequency.

Selective suppression of the monomer becomes impossible at such rotational temper-

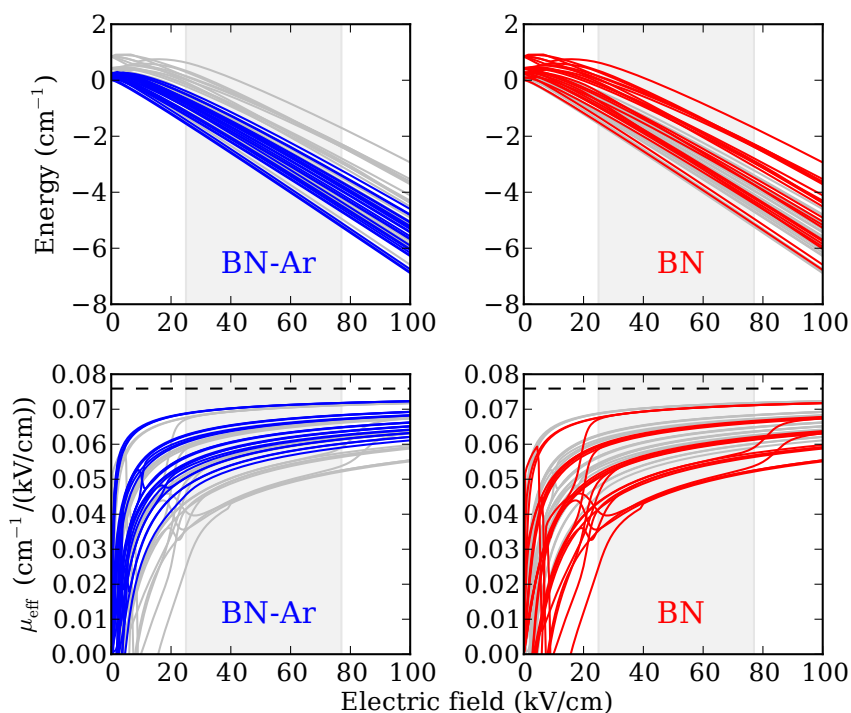


**Figure 6.4:** Upper row: Calculated Stark energies of the lowest rotational states ( $J \leq 2$ ) of the complex (blue) and benzonitrile (red) as a function of the electric field. The light grey curves depict the species shown in the respective other column for comparison. Lower row: Calculated effective dipole moments, plotted using the same color scheme as in the upper row. Dashed lines: permanent electric dipole moment of benzonitrile,  $4.52 \text{ D} = 0.0759 \text{ cm}^{-1}/(\text{kV}/\text{cm})$ . The electric field range sampled by the molecules inside the selector is depicted by the areas shaded in grey.

atures using only the selector. The transmission through the device is sensitive to the  $\mu/m$ -ratio alone and two molecular species with the same  $\mu/m$ -ratio cannot be distinguished. This is illustrated in Figure 6.5 where the calculated effective dipole moments of benzonitrile and the complex for all rotational states with  $J \leq 4$  are divided by the respective masses. The region above  $5 \times 10^{-4} \text{ cm}^{-1}/(\text{kV}/\text{cm})/\text{u}$  is solely populated by rotational states of benzonitrile. By choosing a switching frequency that is only suitable for the  $\mu_{\text{eff}}/m$ -ratios in that region, transmission of the complex can be suppressed.

For the complex, however, the curves of all states overlap with the monomer, also for states with higher  $J$ -values than shown in Figure 6.5, and, therefore, the selector cannot be operated such that the transmission of the complex is favored while the transmission of benzonitrile is suppressed.

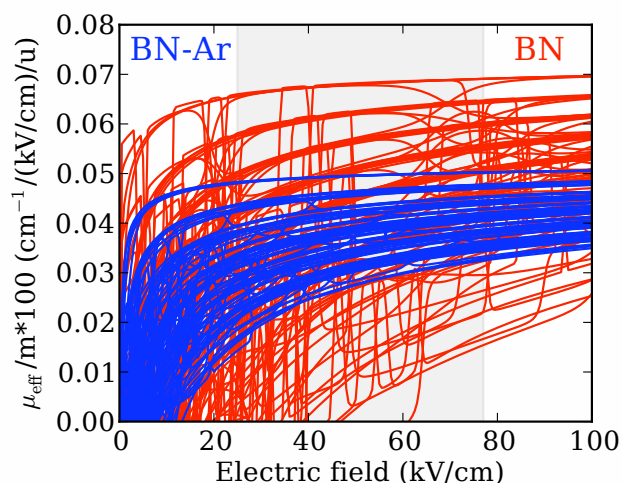


**Figure 6.5:** Calculated  $\mu_{\text{eff}}/m$ -ratios of the lowest rotational states ( $J \leq 4$ ) of benzonitrile (red) and the complex (blue). The electric field range sampled by the molecules inside the selector is depicted by the grey shaded area.

### 6.3 Conclusions

AG focusing of the benzonitrile-argon van der Waals complex in a cold molecular beam has been demonstrated using ac electric fields. At 2.8 kHz ac frequency, the experimental excitation spectrum is described by simulations based on a thermal distribution of the initial states at 0.8 K. The transmission characteristics, i. e., the signal intensity as a function of the ac switching frequency, are described by trajectory simulations in combination with Stark energy calculations. Simulations show that the permanent electric dipole moment of benzonitrile is retained upon the attachment of the argon atom to within  $\pm 5\%$ . By choosing appropriate ac frequencies, transmission of the complex through the selector has been selectively suppressed. When only the ground states of the two species are populated, e. g., near 0 K rotational temperature, transmission can also be restricted to the complex.

Recently, in a related experiment the spatial separation of the indole-water complex from indole was demonstrated using the electric deflector [97]. For this system, the preparation of a practically pure beam of the molecular complex would also be possible using the selector described here, since the dipole moment of the cluster is considerably larger than that of the monomer.

When two molecular species with known masses are guided using the same electric fields, the position of the onset of the transmission curve of one species, and thereby the permanent electric dipole moment of the same, can be predicted from the effective dipole moments of the other species.

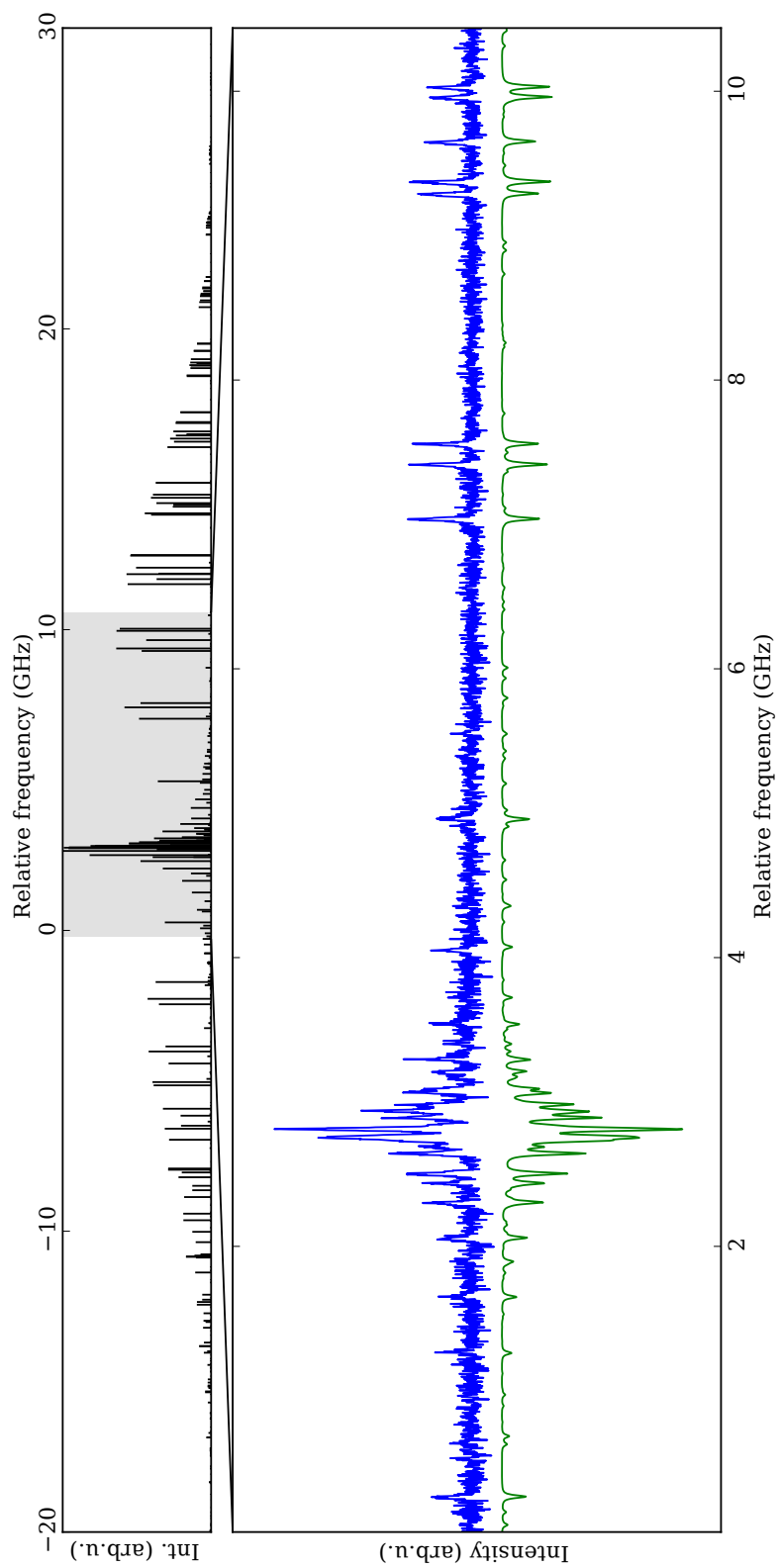


**Figure 6.6:** Simulated and experimental fluorescence excitation spectrum of the benzonitrile-argon complex as previously shown in Figure 6.1 but for a wider range of the excitation frequency.



# Chapter 7

## The alternating-gradient decelerator

In this chapter, the performance of the extended alternating-gradient (AG) decelerator is detailed. The decelerator has 54 deceleration stages, twice as many as the 27 stages employed in the previous prototype [32, 45, 47]. For improved transverse focusing, the direction of the deceleration stages is changed after every two stages whereas it was previously changed after every three stages. The working principle of AG deceleration and the numerical simulation of the decelerator are detailed in Section 3.3.<sup>1</sup>

First, a technical description of the setup is given, followed by its characterization. In the last section, the experimental results and the influence of mechanical misalignments on the molecular transmission are discussed. Possible improvements over the current design are suggested in a brief outlook section.

### 7.1 Experimental details

In Figure 7.1 a), an overview of the setup of the AG decelerator is given. The vacuum system that houses the decelerator is the same as used in the experiments conducted with the ac selector (see Section 4.1 for a detailed description). The only difference is that the chamber in which the decelerator is placed – corresponding to the selector chamber in the other experiment – consists of only two of the identical 530 mm long chambers and the detection chamber. The distance between the nozzle and a 1.5 mm diameter skimmer is 30 mm. The beginning of the 1073 mm long decelerator is placed 37 mm downstream from the tip of the skimmer. The detection laser intersects the molecular beam axis 65 mm behind the end of the last deceleration stage, resulting in a total flight distance from the nozzle to the detection point of 1205 mm.

The decelerator itself consists of 54 deceleration stages placed along the molecular beam axis in two modules holding 27 stages each. The deceleration stages are numbered 1 to 54 starting from the first stage as shown in Figure 7.1 b). Apart from the attachment to the backbone holders, the mounting scheme of the stages inside the modules resembles that of the ac selector. A module consists of a rigid frame with four identical subunits placed inside. As depicted in Figure 7.2, a subunit consists of a baseplate onto which two ceramic electric isolators are placed. To the other end of the isolators 14 mm diameter, 538 mm long steel rods are mounted, serving as backbones for the electrodes. The 6 mm

---

<sup>1</sup>It must be noted that the focusing and deceleration parameters used here are commonly labeled  $f$  and  $d$  and that these should not be confused with the parameters introduced in the theoretical description of the AG selector in Subsection 3.1.2.

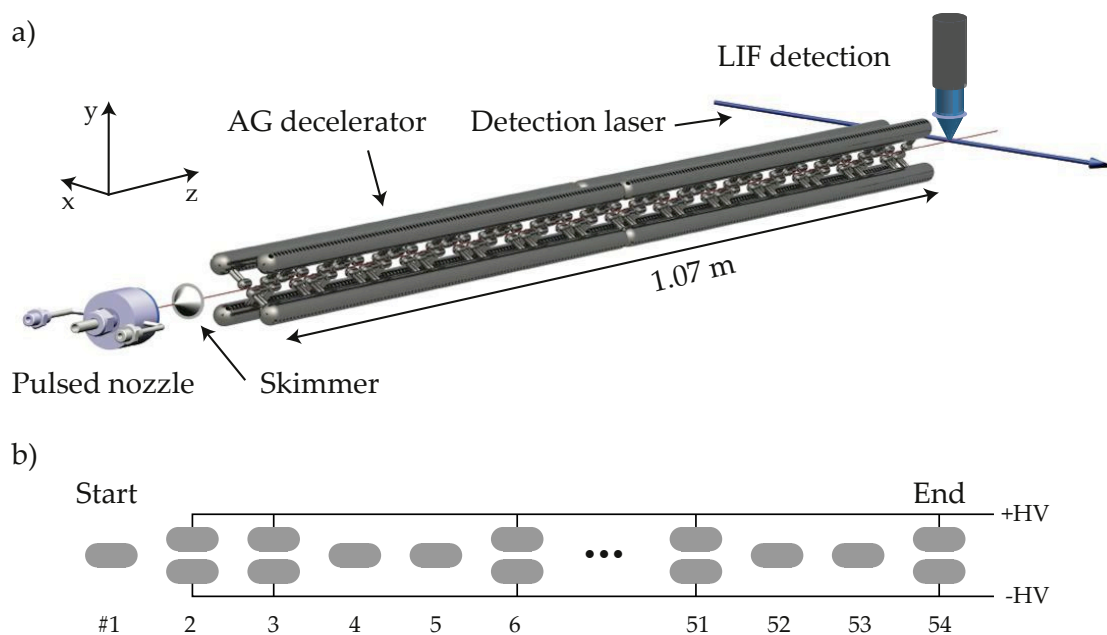


**Figure 7.1:** a) Sketch of the AG decelerator setup. The decelerator consists of two modules, each holding 27 electrode pairs. b) Schematic of the electrode arrangement of the deceleration stages. Indices #1-54 indicate the position of a stage in the array. Stages 1, 4, 5, ... are oriented perpendicular to the other stages and the polarity of the potentials applied to the electrodes in a stage is indicated for stages 2, 3, 6, ...

diameter, 13 mm long stainless steel electrodes are highly-polished and their ends are rounded off with a 3 mm radius of curvature. Each electrode is attached to its respective backbone through two small steel rods each. Inside a stage, the electrodes are placed parallel to each other at a surface-to-surface distance of 2 mm. The distance between two adjacent stages along the molecular beam is 7 mm, leading to a period length of 20 mm.

The output of four rapid 20 kV push-pull switches (Behlke Elektronik, HTS-201-03-GSM) is connected through HV vacuum feedthroughs to the backbones of one module. Corresponding backbones in the two modules are connected using tantalum wires. The HV switches can be triggered independently by the burst unit of a dedicated computer crate.

## 7.2 Focusing and deceleration of benzonitrile

For all measurements presented in this section, benzonitrile is seeded in krypton at room temperature at a stagnation pressure of 1.2 bar, resulting in an estimated beam velocity of 385 m/s and a rotational temperature of about 3.5 K. Ground-state benzonitrile molecules are selectively detected by setting the laser frequency to the center of the  $1_{11} \leftarrow 0_{00}$  transition at  $36\,512.74\text{ cm}^{-1}$ . The arrival time in the time-of-flight (TOF)

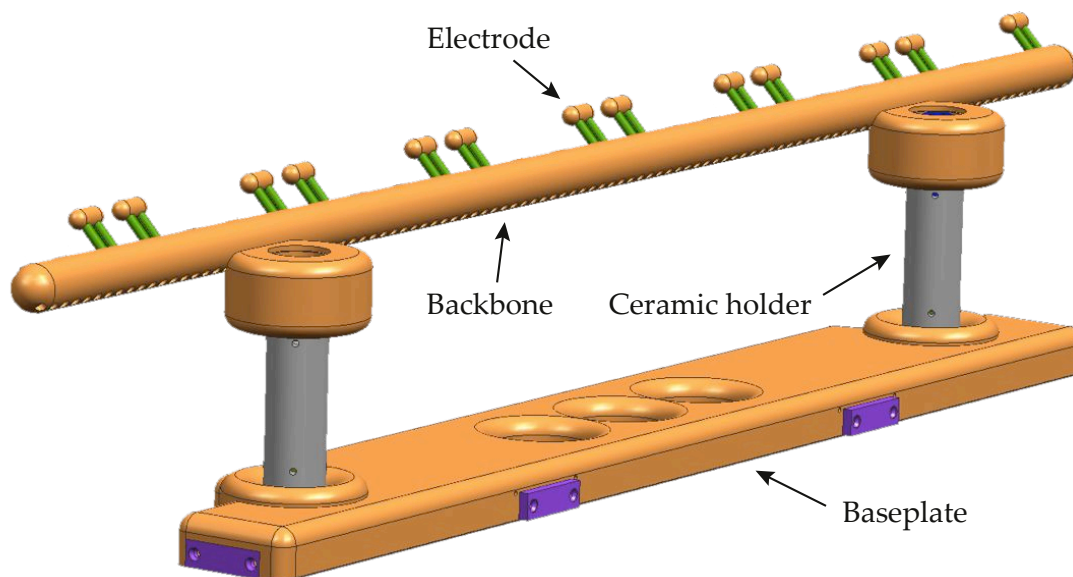


**Figure 7.2:** One of four subunits of an AG decelerator module. The ceramic holders serve as mounts and, at the same time, as electric isolators between the baseplate and the backbone. Each of the cylindrical electrodes is connected to the backbone by two steel rods.

profiles is given relative to the nozzle trigger. All trajectory simulations shown here are performed with the switching sequences from the respective experiments. In order to compare the obtained intensities in experiment and simulation, the free-flight traces are scaled such that their maximum signal is the same in simulation and experiment. The same scaling factor is then used for the other traces. Near the end of the decelerator, the molecular packet stretches over several stages due to the longitudinal velocity spread. The packet is thereby effectively divided into subpackets that contain molecules in the respective stages. The subpacket that contains the synchronous molecule is called the *synchronous packet*.

As a first step in the characterization, to compare experiment and simulation under well-defined conditions, the molecular beam is guided using only a small subset of deceleration stages near the end of the decelerator. To obtain the experimental TOF profiles shown in the upper part of Figure 7.3, the LIF signal of 2500 molecular beam pulses is averaged and the curves are subsequently smoothed by calculating a running average over three points. The lower set of TOF profiles depicts the outcome of trajectory calculations. The applied switching sequences are calculated such that the synchronous molecule is in one of the last deceleration stages (#53,#54) when guiding fields with  $f=10$  mm are applied.<sup>2</sup>

When only the last stage, #54, is used, a clear dip in the TOF profile (green traces)

<sup>2</sup>As defined in Section 3.3, the focusing parameter,  $f$ , is the distance the synchronous molecules travels when the electric field is switched on;  $f$  is centered around the middle of the stage when guiding.

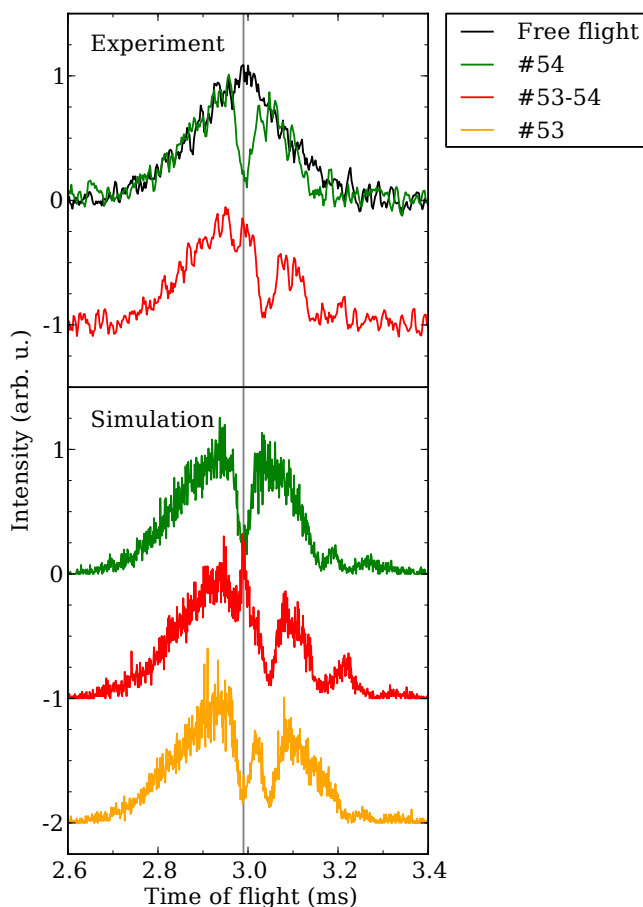


**Figure 7.3:** Time-of-flight profiles obtained in free flight (black trace) and under different switching conditions for guiding with  $f=10$  mm at a beam velocity of 385 m/s. Traces in the upper part of the panel depict experimental data (smoothed using a running average over three adjacent points). The simulations shown in the lower part were performed with the switching sequences used in the experiment. The vertical line indicates the arrival time of the synchronous molecule. The traces are offset for clarity.

is seen at 2.99 ms corresponding to the arrival time of the synchronous packet. The detected LIF intensity in this region is reduced, because the molecules in the subpacket are so strongly defocused/overfocused that they do not intersect the laser beam anymore. At later arrival times, the same effect is seen for molecules that are located inside stages #50–51 at the time the field is switched on, because these stages have the same potential as stage #54. Meanwhile, stages #52–53 are on ground potential and molecules in the corresponding subpackets remain unaltered compared to free flight. A clear dip in the simulated LIF signal is also observed for the synchronous packet when it is only focused in stage #53 (yellow trace). The other dip appearing about 50  $\mu$ s later corresponds to

the subpacket that trails the synchronous packet by one deceleration stage and that is de-/focused in the same way, because stages #52-53 are connected to the same potentials.

As depicted by the red traces, a strong LIF signal is obtained from the synchronous packet when both stages #53–54 are used, exemplifying the dynamic-focusing principle. First, as indicated above, the synchronous packet is de-/focused in stage #53 and, because of the interchanged focusing directions between #53 and #54, the de-/focusing is reversed in #54 and a peak in intensity is observed, effectively "filling" the dip observed before. However, no refocusing occurs for the subpacket trailing the synchronous packet, because these molecules are solely defocused in stage #52 at the time the synchronous molecule is inside stage #53. When they reach stage #53, high voltages are only applied to stages #54, #51–50, . . . so that no refocusing can occur. The experimental TOFs are nicely matched by the simulations, indicating that the burst sequence is chosen such that the synchronous packet is clearly located in the central part of the molecular pulse.

The experimental TOF profiles depicted as the upper traces in Figure 7.4 are obtained by guiding the molecular beam in the last 8 deceleration stages (#47-54) and corresponding simulations are shown as lower traces. The subpackets appear as distinct peaks in the TOF profiles and, according to the measurements shown in Figure 7.3, the synchronous packet corresponds to the peak at an arrival time of 2.99 ms. In the experiment, the peak originating from the synchronous packet is most intense for  $f=6$  mm. No LIF light is detected at all for  $f=9$  whereas it is predicted to be intense in the simulation.

Guiding and deceleration data using all 54 stages of the decelerator is depicted in Figure 7.5. The experimental TOF profiles depicted as upper traces are obtained by averaging the signal of 30000 molecular beam pulses and corresponding simulations are shown in the lower traces in same color. The experimental free-flight signal is shown as black trace. For clarity, the simulated TOF profiles are scaled down by an additional factor of 10 compared to the other figures in this graph. At a focusing length of  $f=4$  mm, the deceleration parameter is varied from  $d=2$  mm, corresponding to guiding, up to  $d=4$  mm.

It is obvious that for both guiding and deceleration traces the number of detected molecules is greatly reduced compared to the free-flight and that mostly structureless, broad TOF profiles are obtained. In each simulated TOF profile, however, several distinct peaks are observed. At the arrival time of the synchronous packet in the simulations, indicated by black arrows, only a faint peak is observed in the experimental traces. With increasing value of  $d$ , these peaks appear at later arrival times, indicating the deceleration.

## 7.3 Discussion and outlook

The simulations predict that the number of molecules in the detection region can be increased compared to the free flight when the decelerator is operated in guiding mode. As shown in Figure 7.4, using only a small subset of the stages near the end of the decelerator results in a low signal. Simulations predict that the transmission increases as the subset of used stages is enlarged towards the beginning of the decelerator (shown in

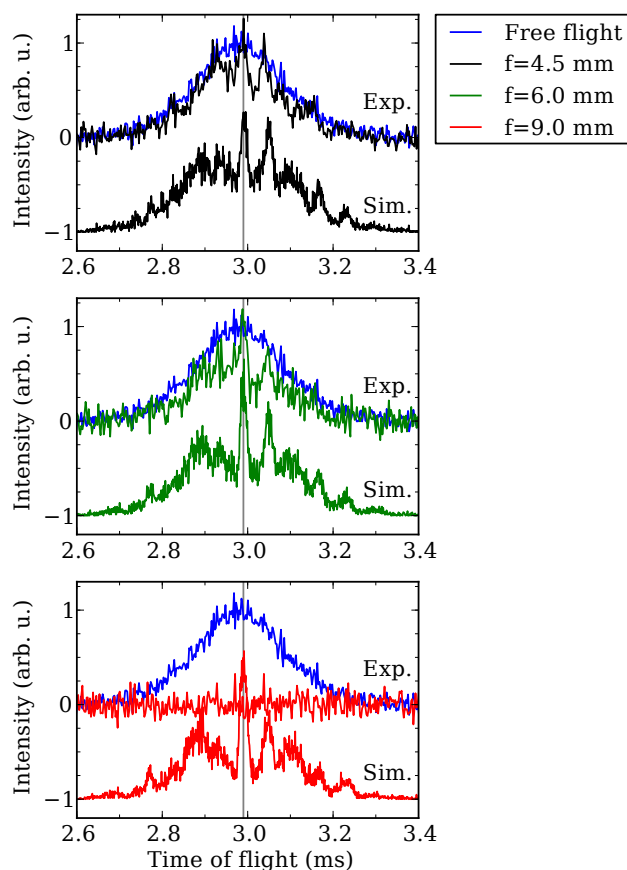


**Figure 7.4:** Guiding of ground-state benzonitrile molecules using the last 8 electrodes of the decelerator at 385 m/s forward velocity and at the indicated focusing lengths. Upper time-of-flight profiles in each panel show the experiment, the lower traces in the same color show corresponding trajectory simulations (offset for clarity). The vertical line indicates the arrival time of the synchronous molecule.

the upper left panel in Figure 7.6). In the experiment, no indication of the enhancement over the free-flight that is predicted by the simulations is seen.

### Effects of misalignment

As shown in Figure 7.5, when all electrodes are used in the experiment for guiding and deceleration, the overall intensity is well below the free-flight intensity and the sharp structures predicted by the simulations are not observed. The disagreement between experiment and simulation is most likely caused by mechanical misalignment of the electrodes. The performance of the decelerator is significantly reduced by such a misalignment which results in distorted electric fields and, thereby, in a reduced number of stable trajectories. Due to the achievable mechanical precision of the machining process

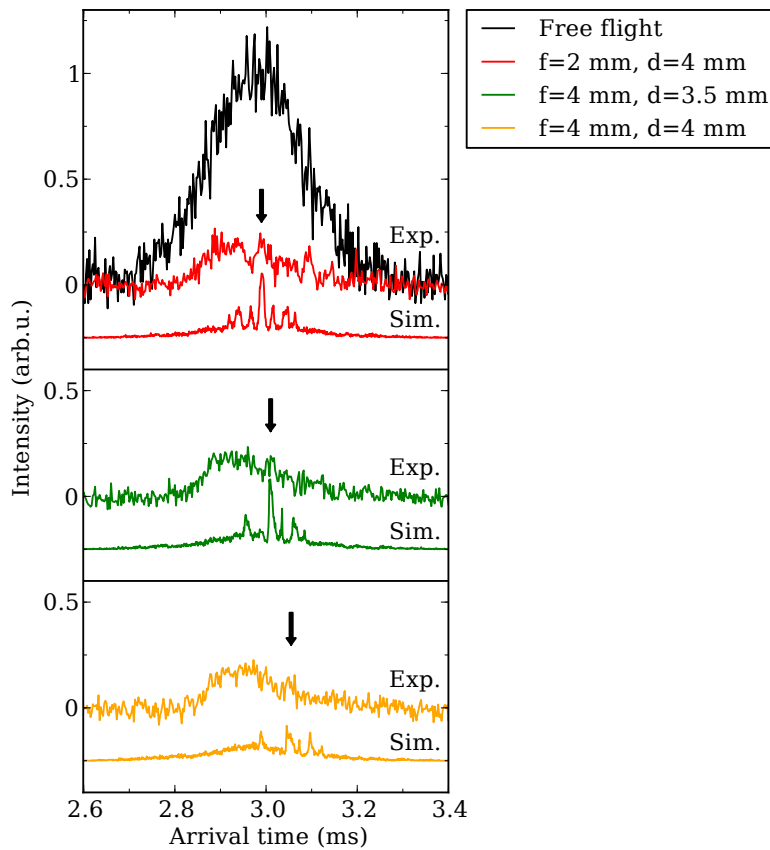


**Figure 7.5:** Guiding and deceleration of ground-state benzonitrile molecules using all electrodes of the decelerator at a focusing length of  $f=4$  mm and at the indicated values of  $d$ . The traces are offset for clarity. See text for details.

and the manual assembly, both the relative alignment of the deceleration stages relative to each other and the alignment of the electrodes inside a stage relative to each other varies.

The effect of transverse misalignment on the TOF profiles obtained with the present decelerator is shown in Figure 7.6. Ground-state benzonitrile molecules with a forward velocity of 320 m/s are guided using focusing lengths in the range from 3 to 9 mm. Each deceleration stage is randomly shifted in the  $x$ - and  $y$ -directions, where the displacements are normally distributed around 0 with the standard deviation  $\Delta$ . While each stage is shifted individually in the experiment, the shift is modeled in the simulations as a simple translation of the calculated electric fields, thereby shifting two adjacent stages in the same way. Figure 7.6 shows the outcome of simulations at the different indicated misalignments  $\Delta$  from 0, i.e., perfect alignment, to 75  $\mu\text{m}$ . Each TOF profile is the average over 10 individual simulations, each performed with a packet of  $2 \times 10^6$  molecules and a specific set of random misalignments. Detection is taken into account by only

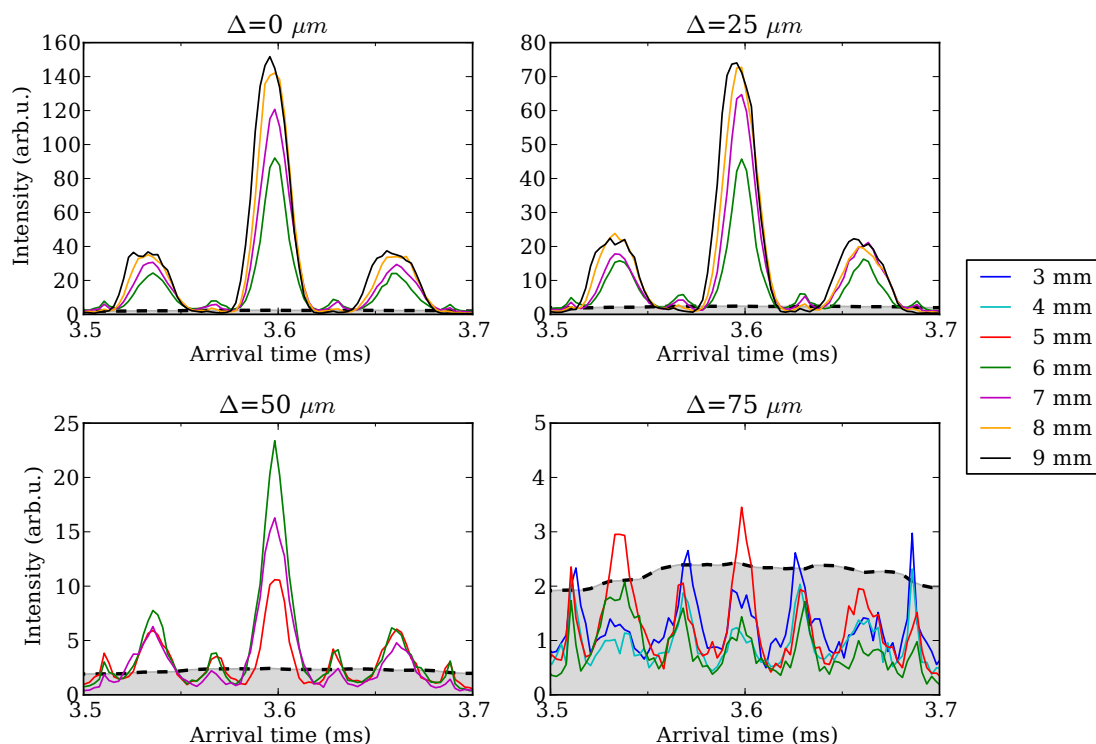


**Figure 7.6:** Simulated TOF profiles for guided ground-state benzonitrile molecules with a forward velocity of 320 m/s as a function of the focusing length  $f$  and misalignment  $\Delta$ . In each panel the free-flight signal is indicated by the dashed line and the grey-shaded area. See text for details.

accepting molecules that intersect the laser beam within a  $\pm 1$  mm vertical range. For comparison, the free-flight signal is shown as dashed black line. The highest intensity is seen at an arrival time of 3.6 ms, where the synchronous peak appears in the guiding simulations. At  $\Delta = 0 \mu\text{m}$ , the peak intensity is increased about 60-fold over the free flight when  $f = 9$  mm is chosen. For higher values of  $\Delta$ , however, the highest intensity is significantly lower than this value. At  $\Delta = 25$  and  $50 \mu\text{m}$ , the peak intensity drops to relative values of 30 and 10, respectively, and at  $\Delta = 75 \mu\text{m}$ , the intensity is on the order of the free flight. This tendency highlights the necessity of an accurate alignment.

Measurements show that for the present decelerator  $\Delta$  is on the order of  $50 \mu\text{m}$  as for the previous design [47]. Such a transverse shift of a deceleration stage is fairly easy to implement in the simulations as translation of the electric field. However, from the simulations for  $\Delta = 50 \mu\text{m}$  it becomes clear that the transverse displacement of individual stages alone cannot explain the low intensities observed in the experiment.

To improve the model of the decelerator in the simulations, more types of misalignment need to be considered, none of which have been implemented yet. For example, stages can be tilted from the beam axis, resulting in a broken symmetry of the AG fields. Longitudinal shifts of the stages influence the field gradients on the beam axis and, as

a result, the obtained deceleration per stage is different than assumed in the switching sequence. Measurements using gauge blocks show that the distance between two adjacent electrodes on the same backbone varies on average by  $40\ \mu\text{m}$  from the design position in the longitudinal direction and by  $50\ \mu\text{m}$  between electrodes on different backbones. The longitudinal position of the ends of two electrodes in a stage varies by  $30\ \mu\text{m}$ . The influence of these misalignments on the transmission is expected to be important, because their values compare to the value of  $\Delta$ . Nevertheless, while the misalignments still remain to be implemented in the simulations to obtain a more accurate description, an improved mechanical accuracy is needed for which suggestions are given in the following.

### **Improving the AG decelerator**

As discussed above, efficient AG guiding and deceleration requires better alignment than currently achieved in our decelerator. In principle, the misalignments could be reduced by employing modern measuring techniques during the assembly. By adapting the holding scheme implemented in the ac selector, for example, the transverse misalignment could potentially be kept below  $\pm 20\ \mu\text{m}$  and the variation of the longitudinal position could be even smaller. However, a tremendous effort has already been spent to achieve the current order of accuracy. Given that significant deceleration requires a further extension of the current decelerator and that the electrode alignment is so critical, it is doubtful that the needed improvements are feasible. Barring further developments, it seems that the applicability of the Stark-deceleration technique will remain restricted to molecules in lfs quantum states and that the application of AG focusing for the deceleration of hfs molecules has come to an end.



# Chapter 8

## Summary and outlook

In this thesis two implementations of the alternating-gradient (AG) focusing technique to control the motion of large neutral polar molecules with inhomogeneous electric fields are described. While small molecules have quantum states in which they can be focused using static electric fields, all states of large molecules with small rotational constants require dynamic focusing schemes, such as AG focusing. Both devices described are characterized using pulsed beams of benzonitrile, which is a prototypical large asymmetric top molecule with a high density of rotational quantum states and a complicated Stark-manifold in electric fields. Furthermore, it has a relatively large dipole-moment-to-mass ( $\mu/m$ ) ratio, making it well-suited for manipulation using the Stark interaction.

A new AG focuser has been set up allowing for the guiding of molecules by dynamic transverse focusing. Its working principle is similar to that of the quadrupole mass-filter for ions. The accuracy of the generated electric fields is crucial for efficient transport through the focuser and it has been greatly enhanced over the previous-generation focuser. As the efficiency of the guiding process is very sensitive to the  $\mu/m$ -ratio, the focuser can be considered a  $\mu/m$ -selector and it has been shown how species that differ in at least one property, mass  $m$  or dipole moment  $\mu$ , can be separated.

In combination with detection using a narrowband continuous wave laser, the quantum-state-specific transmission of the selector, as well as the transverse velocity distribution of the molecules exiting the selector, have been measured as a function of the ac switching frequency. It has been demonstrated that by applying asymmetric ac waveforms, a  $\mu/\Delta\mu$ -resolution can be obtained that is sufficient to exclusively transmit benzonitrile molecules in quantum states that have the same  $\mu/m$ -value as its absolute ground state.

The benzonitrile-argon van der Waals complex is also present in the benzonitrile expansion. It has a considerably higher mass than benzonitrile but is expected to have a similar dipole moment. By choosing appropriate ac frequencies, the transmission of the complex through the selector has been selectively suppressed. It is not possible to suppress benzonitrile while maintaining transmission of the complex, unless only the ground states of the two species are populated, i. e., at a rotational temperature substantially lower than the experimentally achievable temperature.

The measured transmission characteristics of the selector are in good agreement with the outcome of trajectory simulations. This understanding opens the way to applications in future experiments. From simulations in combination with Stark-energy calculations it has been deduced that the orientation of the permanent electric dipole moment of benzonitrile is indeed retained upon the attachment of the argon atom. The magnitude

of the dipole moment was found to be same as for the monomer to within  $\pm 5\%$ . Furthermore, it has been shown how the velocity of the molecular beam can be obtained by exploiting end effects during the guiding process.

Neutral molecules can be aligned in free space by applying strong, nonresonant laser pulses and also oriented by adding a static electric field [98, 99]. The degree of alignment is enhanced by lowering the initial rotational energy [100]. Using the  $m/\mu$ -selector, a beam of benzonitrile molecules in their rovibronic ground state can be produced. This will enhance the alignment and orientation of molecules in, for example, tomographic imaging [101] and x-ray diffraction studies [102]. Furthermore, the selector provides samples of highly oriented molecules [103]. To maintain a defined orientation for a subsequent experiment, an additional static electric guiding field of about 25 kV/cm is needed at the exit of the selector.

As an alternative to the  $m/\mu$ -selector, a static "two-wire" deflector has been used to prepare pure samples of large molecules for alignment and orientation studies [16, 104] as well as to separate structural isomers and clusters of molecules [97, 105]. The working principle is similar to that of the Stern-Gerlach-type selector for atoms with different magnetic-moments. Polar molecules flying through a static electric field that is inhomogeneous in the vertical direction, are deflected depending on their dipole moment. Using focused laser beams, molecules with a certain range of dipole moments can be probed selectively by adjusting the position of the laser focus. Although the implementation of the deflector is more straightforward than that of the focuser, its application is also more limited, because the generated samples are not focused; the difference in applicability between the two devices is similar to the difference in applicability between a static ion deflector (a separator or bender) and a quadrupole mass-filter.

The selector cannot clean the molecular beam from unpolar constituents such as, for example, the benzonitrile dimer [88] and rare-gas atoms from the supersonic expansion. This problem can be overcome by tilting the selector such that unpolar species in the molecular beam do not reach the detection area [33].

AG focusing can also be combined with the Stark deceleration technique in a so-called AG decelerator to slow down beams of large molecules. Such a decelerator has been set up in our group. Compared to the previous generation, the design has been optimized to reach lower beam velocities by doubling the number of deceleration stages and changing their arrangement. While the achieved deceleration is in accordance with trajectory simulations, the transmission through the decelerator is much smaller than predicted by the simulations. This poor efficiency has been attributed to mechanical misalignments of the individual deceleration stages, as suggested by trajectory simulations in which misalignment effects were included. To achieve beam velocities low enough for the envisioned trapping of benzonitrile, the decelerator needs to be extended considerably, i. e., the number of deceleration stages must be doubled from 54 to about 100. At the currently achieved accuracy of the generated electric fields, the application of such an extension is not feasible, highlighting the need to implement a better mechanical setup.

## Bibliography

- [1] S. Y. T. van de Meerakker, H. L. Bethlem, N. Vanhaecke, and G. Meijer, *Manipulation and Control of Molecular Beams*, Chemical Reviews **112**, 4828–4878 (2012).
- [2] R. Krems, W. C. Stwalley, and B. Friedrich, editors, *Cold Molecules: Theory, Experiment, Applications*, CRC Press, Taylor&Francis Group (2009), ISBN 9781420059038.
- [3] G. Scoles, editor, *Atomic and molecular beam methods*, volume 1 & 2, Oxford University Press, New York, NY, USA (1988 & 1992), ISBN 0195042808.
- [4] D. H. Levy, *The spectroscopy of very cold gases*, Science **214**, 263–269 (1981).
- [5] T. R. Rizzo, Y. D. Park, L. Peteanu, and D. H. Levy, *Electronic spectrum of the amino acid tryptophan cooled in a supersonic molecular beam*, J. Chem. Phys. **83**, 4819–4820 (1985).
- [6] S. Y. T. van de Meerakker, H. L. Bethlem, and G. Meijer, *Taming molecular beams*, Nature Phys. **4**, 595 (2008).
- [7] T. E. Wall, S. Armitage, J. J. Hudson, B. E. Sauer, J. M. Dyne, E. A. Hinds, and M. R. Tarbutt, *Transport of polar molecules by an alternating gradient guide*, Phys. Rev. A **80**, 043407 (2009).
- [8] S. D. Hogan, M. Motsch, and F. Merkt, *Deceleration of supersonic beams using inhomogeneous electric and magnetic fields*, Phys. Chem. Chem. Phys. **13**, 18705–18723 (2011).
- [9] E. Narevicius and M. G. Raizen, *Toward Cold Chemistry with Magnetically Decelerated Supersonic Beams*, Chemical Reviews **112**, 4879–4889 (2012).
- [10] S. Merz, N. Vanhaecke, W. Jäger, M. Schnell, and G. Meijer, *Decelerating molecules with microwave fields*, Phys. Rev. A **85**, 063411 (2012).
- [11] J. F. Barry, E. S. Shuman, E. B. Norrgard, and D. DeMille, *Laser Radiation Pressure Slowing of a Molecular Beam*, Phys. Rev. Lett. **108**, 103002 (2012).
- [12] M. A. Chieda and E. E. Eyler, *Prospects for rapid deceleration of small molecules by optical bichromatic forces*, Phys. Rev. A **84**, 063401 (2011).
- [13] A. Osterwalder, S. A. Meek, G. Hammer, H. Haak, and G. Meijer, *Deceleration of neutral molecules in macroscopic traveling traps*, Phys. Rev. A **81**, 051401 (2010).

- [14] N. E. Bulleid, R. J. Hendricks, E. A. Hinds, S. A. Meek, G. Meijer, A. Osterwalder, and M. R. Tarbutt, *Traveling-wave deceleration of heavy polar molecules in low-field-seeking states*, Phys. Rev. A **86**, 021404 (2012).
- [15] H. Kallmann and F. Reiche, *Über den Durchgang bewegter Moleküle durch inhomogene Kraftfelder*, Z. Phys. **6**, 352–375 (1921).
- [16] L. Holmegaard, J. H. Nielsen, I. Nevo, H. Stapelfeldt, F. Filsinger, J. Küpper, and G. Meijer, *Laser-induced alignment and orientation of quantum-state-selected large molecules*, Phys. Rev. Lett. **102**, 023001 (2009).
- [17] O. Stern, *Ein Weg zur experimentellen Prüfung der Richtungsquantelung im Magnetfeld*, Z. Phys. **7**, 249–253 (1921).
- [18] W. Gerlach and O. Stern, *Der experimentelle Nachweis der Richtungsquantelung im Magnetfeld*, Z. Phys. **9**, 349–352 (1922).
- [19] W. Gerlach and O. Stern, *Das magnetische Moment des Silberatoms*, Z. Phys. **9**, 353–355 (1922).
- [20] E. Wrede, *Über die Ablenkung von Molekularstrahlen elektrischer Dipolmoleküle im inhomogenen elektrischen Feld*, Z. Phys. **44**, 261–268 (1927).
- [21] I. Estermann and R. G. J. Fraser, *The Deflection of Molecular Rays in an Electric Field: The Electric Moment of Hydrogen Chloride*, J. Chem. Phys. **1**, 390–399 (1933).
- [22] I. Compagnon, R. Antoine, D. Rayane, P. Dugourd, and M. Broyer, *Molecular beam deflection experiments on mixed clusters - Permanent dipole of transition metal-C-60 compounds*, Eur. Phys. J. D **16**, 365–368 (2001).
- [23] R. Antoine, I. Compagnon, D. Rayane, M. Broyer, P. Dugourd, G. Breaux, F. C. Hagemester, D. Pippen, R. R. Hudgins, and M. F. Jarrold, *Electric dipole moments and conformations of isolated peptides*, Eur. Phys. J. D **20**, 583–587 (2002).
- [24] H. G. Bennowitz, W. Paul, and C. Schlier, *Fokussierung polarer Moleküle*, Z. Phys. **141**, 6 (1955).
- [25] J. P. Gordon, H. J. Zeiger, and C. H. Townes, *The Maser - New Type of Microwave Amplifier, Frequency Standard, and Spectrometer*, Phys. Rev. **99**, 1264–1274 (1955).
- [26] D. Auerbach, E. E. A. Bromberg, and L. Wharton, *Alternate-gradient focusing of molecular beams*, J. Chem. Phys. **45**, 2160 (1966).
- [27] E. D. Courant and H. S. Snyder, *Theory of the alternating-gradient synchrotron*, Ann. Phys. **3**, 1–48 (1958).

- 
- [28] D. Kakati and D. C. Lainé, *Alternate-gradient focusing of a molecular beam of ammonia*, Phys. Lett. A **24**, 676 (1967).
- [29] H. L. Bethlem, A. J. A. van Roij, R. T. Jongma, and G. Meijer, *Alternate gradient focusing and deceleration of a molecular beam*, Phys. Rev. Lett. **88**, 133003 (2002).
- [30] J. van Veldhoven, H. L. Bethlem, and G. Meijer, *AC electric trap for ground-state molecules*, Phys. Rev. Lett. **94**, 083001 (2005).
- [31] T. Junglen, T. Rieger, S. A. Rangwala, P. W. H. Pinkse, and G. Rempe, *Two-Dimensional Trapping of Dipolar Molecules in Time-Varying Electric Fields*, Phys. Rev. Lett. **92**, 223001 (2004).
- [32] K. Wohlfart, F. Grätz, F. Filsinger, H. Haak, G. Meijer, and J. Küpper, *Alternating-gradient focusing and deceleration of large molecules*, Phys. Rev. A **77**, 031404(R) (2008).
- [33] F. Filsinger, U. Erlekam, G. von Helden, J. Küpper, and G. Meijer, *Selector for structural isomers of neutral molecules*, Phys. Rev. Lett. **100**, 133003 (2008).
- [34] W. Paul and H. Steinwedel, *Ein neues Massenspektrometer ohne Magnetfeld*, Z. Naturforsch. A **8**, 448–450 (1953).
- [35] W. Paul and M. Raether, *Das elektrische Massenfilter*, Z. Phys. **140**, 262–273 (1955).
- [36] W. Paul, O. Osberghaus, and E. Fischer, *Ein Ionenkäfig*, Forschungsbericht, Wirtschafts- und Verkehrsministerium Nordrhein Westfalen (1958).
- [37] F. Filsinger, U. Erlekam, G. von Helden, J. Küpper, and G. Meijer, *Selector for structural isomers of neutral molecules*, Virt. J. Bio. Phys. Res. **15** (2008).
- [38] R. M. Helm, H. P. Vogel, and H. J. Neusser, *Highly resolved UV spectroscopy: structure of S1 benzonitrile and benzonitrile-argon by correlation automated rotational fitting*, Chem. Phys. Lett. **270**, 285–292 (1997).
- [39] H. L. Bethlem, G. Berden, and G. Meijer, *Decelerating neutral dipolar molecules*, Phys. Rev. Lett. **83**, 1558–1561 (1999).
- [40] H. L. Bethlem, G. Berden, A. J. A. van Roij, F. M. H. Crompvoets, and G. Meijer, *Trapping neutral molecules in a traveling potential well*, Phys. Rev. Lett. **84**, 5744–5747 (2000).
- [41] E. R. Hudson, J. R. Bochinski, H. J. Lewandowski, B. C. Sawyer, and J. Ye, *Efficient Stark deceleration of cold polar molecules*, Eur. Phys. J. D **31**, 351–358 (2004).
- [42] S. Y. van de Meerakker, I. Labazan, S. Hoekstra, J. Küpper, and G. Meijer, *Production and deceleration of a pulsed beam of metastable NH ( $a^1\Delta$ ) radicals*, J. Phys. B **39**, S1077–S1084 (2006).

- [43] T. E. Wall, J. F. Kanem, J. M. Dyne, J. J. Hudson, B. E. Sauer, E. A. Hinds, and M. R. Tarbutt, *Stark deceleration of CaF molecules in strong- and weak-field seeking states*, Phys. Chem. Chem. Phys. **13**, 18991–18999 (2011).
- [44] M. R. Tarbutt, J. J. Hudson, B. E. Sauer, and E. A. Hinds, *Prospects for measuring the electric dipole moment of the electron using electrically trapped polar molecules*, Faraday Discuss. **142**, 37–56 (2009).
- [45] K. Wohlfart, F. Filsinger, F. Grätz, J. Küpper, and G. Meijer, *Stark deceleration of OH radicals in low-field-seeking and high-field-seeking quantum states*, Phys. Rev. A **78**, 033421 (2008).
- [46] M. R. Tarbutt, H. L. Bethlem, J. J. Hudson, V. L. Ryabov, V. A. Ryzhov, B. E. Sauer, G. Meijer, and E. A. Hinds, *Slowing Heavy, Ground-State Molecules using an Alternating Gradient Decelerator*, Phys. Rev. Lett. **92**, 173002 (2004).
- [47] K. Wohlfart, *Alternating-gradient focusing and deceleration of large molecules*, Dissertation, Free University, Berlin, Germany (2008).
- [48] W. Gordy and R. L. Cook, *Microwave Molecular Spectra*, John Wiley & Sons, New York, NY, USA, 3 edition (1984).
- [49] H. W. Kroto, *Molecular Rotation Spectra*, Dover Publications, New York, NY, USA (1975).
- [50] M. Born and R. Oppenheimer, *Zur Quantentheorie der Molekeln*, Ann. Physik **84**, 457–484 (1927).
- [51] M. Abd El Rahim, R. Antoine, M. Broyer, D. Rayane, and P. Dugourd, *Asymmetric Top Rotors in Electric Fields: Influence of Chaos and Collisions in Molecular Beam Deflection Experiments*, J. Phys. Chem. A **109**, 8507–8514 (2005).
- [52] J. K. G. Watson, *Aspects of Quartic and Sextic Centrifugal Effects on Rotational Energy Levels*, in J. R. Durig, editor, *Vibrational Spectra and Structure*, volume 6, chapter 1, Marcel Dekker (1977).
- [53] S. C. Wang, *On the Asymmetrical Top in Quantum Mechanics*, Phys. Rev. **34**, 243 (1929).
- [54] J. Küpper and F. Filsinger, *libcoldmol: A particle trajectory calculation framework* (2003-2012), URL: <http://libcoldmol.cold-molecules.info>.
- [55] P. R. Bunker and P. Jensen, *Molecular Symmetry and Spectroscopy*, NRC Research Press, Ottawa, Ontario, Canada, 2 edition (1998).
- [56] K. Wohlfart, M. Schnell, J.-U. Grabow, and J. Küpper, *Precise dipole moment and quadrupole coupling constants of benzonitrile*, J. Mol. Spec. **247**, 119–121 (2008).

- 
- [57] D. R. Borst, T. M. Korter, and D. W. Pratt, *On the additivity of bond dipole moments. Stark effect studies of the rotationally resolved electronic spectra of aniline, benzonitrile, and aminobenzonitrile*, Chem. Phys. Lett. **350**, 485–490 (2001).
- [58] W. L. Meerts, M. Schmitt, and G. C. Groenenboom, *New applications of the genetic algorithm for the interpretation of high-resolution spectra*, Can. J. Chem. **82**, 804–819 (2004).
- [59] C. Ratzer, *Strukturänderungen aromatischer Moleküle bei elektronischer Anregung*, Dissertation, Heinrich-Heine-University, Düsseldorf, Germany (2004).
- [60] S. Putzke, F. Filsinger, J. Küpper, and G. Meijer, *Alternating-gradient focusing of the benzonitrile-argon van der Waals complex*, The Journal of Chemical Physics **137**, 104310 (2012).
- [61] U. Dahmen, W. Stahl, and H. Dreizler, *The Rotational Spectrum of the Benzonitrile-Argon Van der Waals Complex*, Ber. Bunsenges. Phys. Chem. **98**, 970–974 (1994).
- [62] C. M. Western, *PGOPHER, a Program for Simulating Rotational Structure*, University of Bristol, Bristol, UK, URL: <http://pgopher.chm.bris.ac.uk>.
- [63] F. Filsinger, *Manipulation of large neutral molecules with electric fields*, Ph.D. thesis, Radboud Universiteit, Nijmegen, The Netherlands (2010).
- [64] H. L. Bethlem, M. R. Tarbutt, J. Küpper, D. Carty, K. Wohlfart, E. A. Hinds, and G. Meijer, *Alternating gradient focusing and deceleration of polar molecules*, J. Phys. B **39**, R263–R291 (2006).
- [65] F. Filsinger, S. Putzke, H. Haak, G. Meijer, and J. Küpper, *Optimizing the resolution of the alternating-gradient  $m/\mu$  selector*, Phys. Rev. A **82**, 052513 (2010).
- [66] S. Earnshaw, *On the nature of the molecular forces which regulate the constitution of the luminiferous ether*, Trans. Camb. Phil. Soc. **7**, 97–112 (1842).
- [67] W. Paul, *Electromagnetic traps for charged and neutral particles*, Rev. Mod. Phys. **62**, 531 (1990).
- [68] J. G. Kalnins, G. Lambertson, and H. Gould, *Improved alternating gradient transport and focusing of neutral molecules*, Rev. Sci. Instrum. **73**, 2557–2565 (2002).
- [69] P. H. Dawson, editor, *Quadrupole mass spectrometry and its applications*, Elsevier (1976).
- [70] N. Konenkov, M. Sudakov, and D. Douglas, *Matrix Methods for the Calculation of Stability Diagrams in Quadrupole Mass Spectrometry*, J. Am. Soc. Mass. Spectrom. **13**, 597–613 (2002).

- [71] J. A. Richards, R. M. Huey, and J. Hiller, *On the time varying potential in the quadrupole mass spectrometer*, in *Proceedings of the Institution of Radio and Electronics Engineers, Australia*, volume 32, 321–322 (1971).
- [72] J. A. Richards, R. M. Huey, and J. Hiller, *A New Operating Mode for the Quadrupole Mass Filter*, *Int. J. Mass Spectrom. Ion Proc.* **12**, 317–339 (1973).
- [73] L. A. Pipes, *Matrix Solution of Equations of the Mathieu-Hill Type*, *J. Appl. Phys.* **24**, 902–910 (1953).
- [74] Comsol, *Multiphysics 3.4* (2007), <http://www.comsol.com/products/news/3.4>.
- [75] J. Küpper, H. Haak, K. Wohlfart, and G. Meijer, *Compact in-place gate valve for molecular-beam experiments*, *Rev. Sci. Instrum.* **77**, 016106 (2006).
- [76] G. Bardizza, *Setup of a narrow linewidth UV/VIS laser system for high-resolution spectroscopy of cold large molecules*, Master’s thesis, Università degli Studi di Milano, Milano, Italy (2005).
- [77] S. Gerstenkorn and P. Luc, *Atlas du Spectre d’Absorption de la Molecule d’Iode entre*, CNRS, Paris (1985).
- [78] R. W. P. Drever, J. L. Hall, F. V. Kowalski, J. Hough, G. M. Ford, A. J. Munley, and H. Ward, *Laser Phase and Frequency Stabilization Using an Optical Resonator*, *Appl. Phys. B* **31**, 97–105 (1983).
- [79] J. Küpper, H. Junkes, and U. Hoppe, *KouDA: A general purpose data acquisition system* (2003-2012), <http://kouda.cold-molecules.info>.
- [80] B. G. Lindsay, K. A. Smith, and F. B. Dunning, *Control of long-term output frequency drift in commercial dye-lasers*, *Rev. Sci. Instrum.* **62**, 1656–1657 (1991).
- [81] S. M. Jaffe, M. Rochon, and W. M. Yen, *Increasing the frequency stability of single-frequency lasers*, *Rev. Sci. Instrum.* **64**, 2475–2481 (1993).
- [82] J. H. T. Burke, O. Garcia, K. J. Hughes, B. Livedalen, and C. A. Sackett, *Compact implementation of a scanning transfer cavity lock*, *Rev. Sci. Instrum.* **76**, 116105 (2005).
- [83] D. Allan, *Statistics of atomic frequency standards*, *Proceedings of the IEEE* **54**, 221 – 230 (1966), ISSN 0018-9219.
- [84] C. W. Chou, D. B. Hume, J. C. J. Koelemeij, D. J. Wineland, and T. Rosenband, *Frequency Comparison of Two High-Accuracy Al<sup>+</sup> Optical Clocks*, *Phys. Rev. Lett.* **104**, 070802 (2010).
- [85] F. Czerwinski, A. C. Richardson, and L. B. Oddershede, *Quantifying Noise in Optical Tweezers by Allan Variance*, *Opt. Express* **17**, 13255–13269 (2009).

- 
- [86] M. Andersson, F. Czerwinski, and L. B. Oddershede, *Optimizing active and passive calibration of optical tweezers*, *Journal of Optics* **13**, 044020 (2011).
- [87] S. Putzke, F. Filsinger, H. Haak, J. Küpper, and G. Meijer, *Rotational-state-specific guiding of large molecules*, *Phys. Chem. Chem. Phys.* **13**, 18962–18970 (2011).
- [88] T. Kobayashi, K. Honma, O. Kajimoto, and S. Tsuchiya, *Benzonitrile and its van der Waals complexes studied in a free jet. I. The LIF spectra and the structure*, *J. Chem. Phys.* **86**, 1111–1117 (1987).
- [89] F. Lahmani, C. Lardeux-Dedonder, and A. Zehnacker, *Spectroscopy and Dynamics of Benzonitrile-Benzene Complexes in a Supersonic Free-Jet*, *Laser Chem.* **10**, 41–50 (1989).
- [90] S. Schlunk, A. Marian, P. Geng, A. P. Mosk, G. Meijer, and W. Schöllkopf, *Trapping of Rb atoms by ac electric fields*, *Phys. Rev. Lett.* **98**, 223002 (2007).
- [91] H. J. Loesch and A. Remscheid, *Brute force in molecular reaction dynamics: A novel technique for measuring steric effects*, *J. Chem. Phys.* **93**, 4779 (1990).
- [92] B. Friedrich and D. R. Herschbach, *On the possibility of orienting rotationally cooled polar molecules in an electric field*, *Z. Phys. D* **18**, 153 (1991).
- [93] M. Härtelt and B. Friedrich, *Directional states of symmetric-top molecules produced by combined static and radiative electric fields*, *J. Chem. Phys.* **128**, 224313 (2008).
- [94] T. V. Nguyen and D. W. Pratt, *Permanent electric dipole moments of four tryptamine conformers in the gas phase: A new diagnostic of structure and dynamics*, *J. Chem. Phys.* **124**, 054317 (2006).
- [95] G. Scoles, editor, *Atomic and molecular beam methods*, volume 1, Oxford University Press, New York, NY, USA (1988).
- [96] J. G. Choi, J. S. Hayden, M. T. O’Connor, and G. J. Diebold, *Direct detection of momentum flux in atomic and molecular beams*, *J. Appl. Phys.* **52**, 6016–6020 (1981).
- [97] S. Trippel, Y.-P. Chang, S. Stern, T. Mullins, L. Holmegaard, and J. Küpper, *Spatial separation of state- and size-selected neutral clusters*, *Phys. Rev. A* **86**, 033202 (2012).
- [98] J. J. Larsen, K. Hald, N. Bjerre, H. Stapelfeldt, and T. Seideman, *Three dimensional alignment of molecules using elliptically polarized laser fields*, *Phys. Rev. Lett.* **85**, 2470–2473 (2000).
- [99] H. Sakai, S. Minemoto, H. Nanjo, H. Tanji, and T. Suzuki, *Controlling the orientation of polar molecules with combined electrostatic and pulsed, nonresonant laser fields*, *Phys. Rev. Lett.* **90**, 083001 (2003).

- [100] H. Sakai, C. P. Safvan, J. J. Larsen, K. M. Hilligsøe, K. Hald, and H. Stapelfeldt, *Controlling the alignment of neutral molecules by a strong laser field*, J. Chem. Phys. **110**, 10235 (1999).
- [101] J. Itatani, J. Levesque, D. Zeidler, H. Niikura, H. Pépin, J. C. Kieffer, P. B. Corkum, and D. M. Villeneuve, *Tomographic imaging of molecular orbitals*, Nature **432**, 867–871 (2004).
- [102] H. N. Chapman, A. Barty, M. J. Bogan, S. Boutet, S. Frank, S. P. Hau-Riege, S. Marchesini, B. W. Woods, S. Bajt, W. H. Benner, L. W. A., E. Plönjes, M. Kuhlmann, R. Treusch, S. Düsterer, T. Tschentscher, J. R. Schneider, E. Spiller, T. Möller, C. Bostedt, M. Hoener, D. A. Shapiro, K. O. Hodgson, D. van der Spoel, F. Burmeister, M. Bergh, C. Caleman, G. Huldt, M. M. Seibert, F. R. N. C. Maia, R. W. Lee, A. Szönke, N. Timneanu, and J. Hajdu, *Femtosecond diffractive imaging with a soft-X-ray free-electron laser*, Nature Phys. **2**, 839–843 (2006).
- [103] B. Friedrich and D. R. Herschbach, *Spatial Orientation of Molecules in Strong Electric Fields and Evidence for Pendular States*, Nature **353**, 412–414 (1991).
- [104] F. Filsinger, J. Küpper, G. Meijer, L. Holmegaard, J. H. Nielsen, I. Nevo, J. L. Hansen, and H. Stapelfeldt, *Quantum-state selection, alignment, and orientation of large molecules using static electric and laser fields*, J. Chem. Phys. **131**, 064309 (2009).
- [105] F. Filsinger, J. Küpper, G. Meijer, J. L. Hansen, J. Maurer, J. H. Nielsen, L. Holmegaard, and H. Stapelfeldt, *Reine Proben einzelner Konformere: Die Trennung von Stereoisomeren komplexer Moleküle mittels elektrischer Felder*, Angew. Chem. **121**, 7033–7035 (2009).
- [106] H. Mann, H. Schiffelgen, and R. Froyep, *Einführung in die Regelungstechnik*, volume 7, Hanser (1997).

## List of publications

1. Optimizing the resolution of the alternating-gradient  $m/\mu$  selector  
Frank Filsinger, Stephan Putzke, Henrik Haak, Gerard Meijer, and Jochen Küpper  
*Phys. Rev. A* **82**, 052513 (2010)
2. Rotational-state-specific guiding of large molecules  
Stephan Putzke, Frank Filsinger, Henrik Haak, Jochen Küpper and Gerard Meijer  
*Phys. Chem. Chem. Phys.* **13**, 18962 (2011)
3. Producing translationally cold, ground-state CO molecules  
Janneke H. Blokland, Jens Riedel, Stephan Putzke, Boris G. Sartakov, Gerrit C. Groenenboom, and Gerard Meijer  
*J. Chem. Phys.* **135**, 114201 (2011)
4. Alternating-gradient Focusing of the Benzonitrile-Argon Van der Waals Complex  
Stephan Putzke, Frank Filsinger, Jochen Küpper and Gerard Meijer  
*J. Chem. Phys.* **137**, 104310 (2012)



# Curriculum vitae

For reasons of data protection, the curriculum vitae is not included in the online version.  
Der Lebenslauf ist in der Online-Version aus Gründen des Datenschutzes nicht enthalten.



# Selbstständigkeitserklärung

Hiermit erkläre ich, Stephan Putzke, die vorliegende Arbeit selbstständig und nur unter Verwendung der angegebenen Hilfsmittel und Literatur angefertigt zu haben.

Berlin, den 9.10.2012

Stephan Putzke



## Danksagung

The most exciting phrase to hear  
in science, the one that heralds  
new discoveries, is not 'Eureka!'  
but 'That's funny...'

---

*(Isaac Asimov)*

Während meiner Zeit am Fritz-Haber-Institut habe ich die großartige Unterstützung von vielen Personen erfahren, durch deren Hilfe diese Arbeit erst ermöglicht wurde.

Zuerst möchte ich Prof. Gerard Meijer danken, denn er hat mich in seiner Abteilung Molekülphysik am Fritz-Haber-Institut aufgenommen und mir die Möglichkeit gegeben, ein für mich völlig neues Gebiet der Physik kennenzulernen. Er hat mich in jeder Phase meiner Arbeit unterstützt und mit großem Interesse den Fortgang der jeweiligen Experimente verfolgt. Für die Übernahme des Zweitgutachtens danke ich Herrn Prof. Ludger Wöste.

Meine Projekte wurden während der gesamten Zeit kompetent von Prof. Jochen Küpper betreut und ich konnte von ihm unter anderem über Molekülphysik, Spektroskopie und das Simulieren der Experimente lernen. Insbesondere für die Beherrschung des komplizierten Lasersystems war seine Hilfe für mich entscheidend. Ich hatte das Glück, in Dr. Frank Filsinger einen stets hilfsbereiten und offenen Ansprechpartner bezüglich der Experimente und Simulationen zu haben. Gegen Ende meiner Messphase war mir Dr. Nicolas Vanhaecke ein aufmerksamer Ratgeber. Für die Konstruktion des Fokussierers waren die Kreativität und Erfahrung von Henrik Haak von entscheidender Bedeutung, für die geleistete Unterstützung vielen Dank.

Inga von Dölln und Andrea Braaker danke ich für Organisation hinter den Kulissen, die so oft unbemerkt zu bleiben scheint. Große Unterstützung habe ich von den Mitarbeitern des Elektroniklabors erfahren, insbesondere von Georg Heyne, Viktor Platschkowski und Patrick Schlecht. Außerdem konnte ich mich stets auf die Hilfe der Mitarbeiter der Werkstätten verlassen, stellvertretend für alle dortigen Kollegen geht hier mein Dank an Herrn Schwäricke für die immer schnelle und zuverlässige Umsetzung meiner Vorstellungen. Genauso konnte ich zu jeder Zeit auf die Hilfe von Petrik Bischoff zählen, nicht nur, wenn es um dringende mechanische Dinge ging. Uwe Hoppe war immer zur Stelle, um meine Probleme rund um die Messsoftware zu lösen – und das stets schneller als gedacht. Außerdem möchte ich auch Heinz Junkes von der Computer Support Gruppe meinen Dank aussprechen für die stetige Verbesserung der Messtechnik. Von Sandy Gewinner konnte ich viel über Lasertechnik lernen (er von mir zumindest einiges über Mittelfeldduelle). Georg Hammer, Rolf Meilicke und Andreas Liedke halfen mir bei allen weiteren kleinen und großen technischen Problemen.

Unsere direkte Zusammenarbeit war zwar recht kurz (dafür relativ erfolgreich), trotzdem habe ich über die Jahre in Dr. Janneke Blokland eine wichtige Kollegin und Freundin gefunden, die mir zu jeder Zeit als Diskussionspartnerin zur Verfügung stand – zu welchem Thema auch immer. Vielen Dank für eine tolle gemeinsame Zeit!

Prägend war für mich die hervorragende und konstruktive Zusammenarbeit innerhalb der Kalte-Moleküle-Gruppe. Die gemeinsame Zeit im Labor war sehr lehrreich und hat

mir täglich viel Freude bereitet. Insbesondere möchte ich hier Peter, Ludwig, Fabian, Janneke, Christian Schewe, Jens, Wolfgang, Moritz, Simon und Bas-T erwähnen. Dr. Kirstin Wohlfart stand mir auch nach ihrem Abschied aus der Abteilung als Ratgeberin zur Seite.

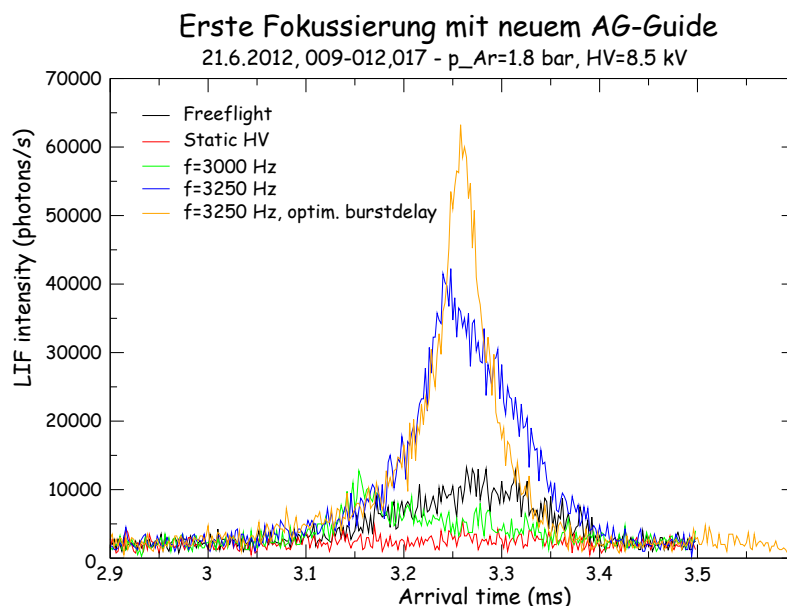
Für das intensive Korrekturlesen meiner Arbeit danke ich Janneke, Frank, Jochen, Prof. Bob Field (MIT), Dr. Phil Bunker (NRC Canada), Dan Engelhart und Ludwig. Ferner hatte ich stets das große Glück, mein Büro mit netten und aufgeschlossenen Kollegen teilen zu können. Mein Dank geht an Torsten, Ludwig, Amudha, Claudia und Isabel.

Ein Höhepunkt war für mich der Auftritt mit unserer Abteilungsband beim Sommerfest 2011. Mein Dank für eine schöne Abwechslung vom Laboralltag geht an die MPLifiers: Janneke, Claudia, Torsten, Petrik, Mikhail, Stephan und Stefan sowie an unseren größten Fan Wolfgang Schultze.

Des Weiteren danke ich allen bislang unerwähnten Kollegen, die mich im Laufe der Jahre begleitet und zur besonderen Stimmung in unserer Abteilung beigetragen haben!

Meinen Eltern danke ich für die Förderung meines Interesses an der Wissenschaft. Ohne ihre fortwährende Unterstützung wäre mir das Physikstudium nicht möglich gewesen und ich wäre ich nicht zu diesem Abschluss gekommen.

Birte, ich konnte mich immer auf Dich verlassen und Du hast mir stets den Rücken frei gehalten und gestärkt. Vielen Dank für die Entbehrungen der letzten Jahre! So wie ich damals ist auch unser Sohn Felix fasziniert vom Labor und ich bin gespannt, ob es ihn in dritter Generation an das Fritz-Haber-Institut ziehen wird...



Erste mit dem neuen AG Fokussierer gemessene Flugzeitprofile von Benzonitrilmolekülen im Grundzustand (21.6.2010).

# Appendix A

## Laser-frequency stabilization

In this appendix, technical details of the laser-frequency stabilization setup described in Subsection 4.3.3 are given. The figures in this appendix are adapted from figures made by Frank Filsinger.

### A.1 Components

In Table A.1, the technical and optical components of the frequency-stabilization setup are summarized. A schematic overview of the setup is given in Figure 4.8.

Component	Details
Control computer	MEN Kahlua Box, running VxWorks 6.3
Arbitrary waveform generator	MEN M68, $\pm 10$ V, 16 bit, 100 kHz
Timer	MEN M72, 4 independent counters, clock frequency 40 MHz
Voltage amplifier	Etalon driver: FHI Elab #3399, 20-fold amplification RDL driver: FHI Elab #3774
Ring Dye Laser	Coherent 899-21 cw laser, typically operated at 548 nm
Frequency stabilized HeNe-Laser	Sios SL 03, nominal wavelength 632.99 nm, specified stability $\pm 1$ MHz/h, 2 MHz/K
Fabry-Perot-Interferometer	Toptica FPI 100, free spectral range 1 GHz, finesse 250, 430-660 nm
Polarizing cube beamsplitter	Ekspla BK7, 10x10x10 mm, $R_s > 95\%$ , $T_p > 95\%$ at 500-650 nm
Fast photodiodes	Thorlabs Det110 Si PIN, rise time 20 ns, active area 13 mm <sup>2</sup> , spectral range: 350-1100 nm
Peakdetectors	FHI Elab #3398
Optical isolator	Laser 2000 - IO-2D-633-VLP, 44 dB

**Table A.1:** Technical and optical components used in the frequency-stabilization setup.

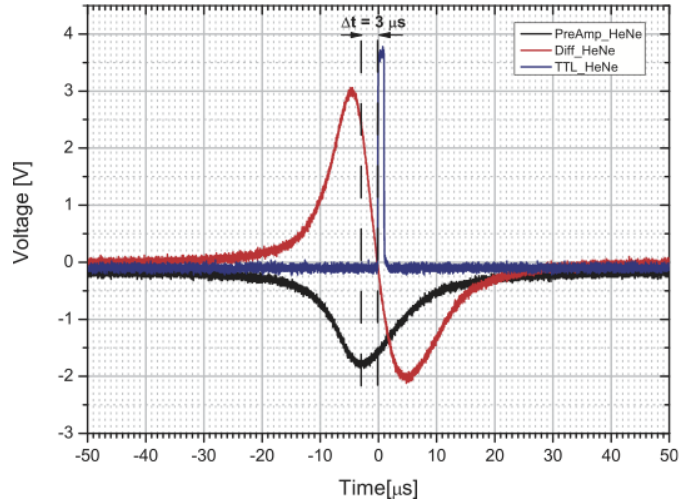


**Figure A.1:** Input signal to the peak detector hardware from the photo diode placed behind the scanning etalon, differentiated signal and generated TTL pulse.

## A.2 Peak detection

The HeNe and RDL light transmitted through the scanning etalon is separated using a polarized cube beamsplitter and independently measured using two fast photo diodes. At each maximum of the photo-diode signal, i. e., at the center of an etalon transmission fringe, home-built peak finding electronics generate a TTL pulse for further processing. The circuit layout of the electronics is shown in Figure A.4. In order to achieve short signal runtimes, the electronics are directly connected to the signal output of the photo diodes. First, the signal is preamplified and differentiated using operation amplifiers. Then, the zero crossing of the differentiated signal, i. e., the maximum of the transmission fringe, is detected by a comparator that subsequently generates a TTL pulse. An adjustable threshold is used to prevent stray light causing unwanted TTL pulses. In Figure A.1, the measured preamplified signal of a detected transmission fringe from the HeNe laser is shown along with the differentiated signal and the generated TTL pulse. All these signals are available for monitoring via dedicated outputs at the detectors.

A delay of about 3  $\mu\text{s}$  is observed between the peak maximum and the rising flank of the TTL pulse, originating from RC elements in the signal processing. Because the resulting delay is always the same, does not affect the time resolution of the peak detection.

## A.3 Input logic - signal processing

The waveforms that are generated by the arbitrary waveform generator (AWG) of the Kahlua Box to drive the scanning etalon and the signal processing are shown schematically in Figure A.2. Channel 0 of the AWG is used to generate a sawtooth voltage that is amplified 20-fold and fed to the Piezo of the scanning etalon. During 87% of a sawtooth period, the voltage is increased linearly by typically 3.2 V, thereby ramping up

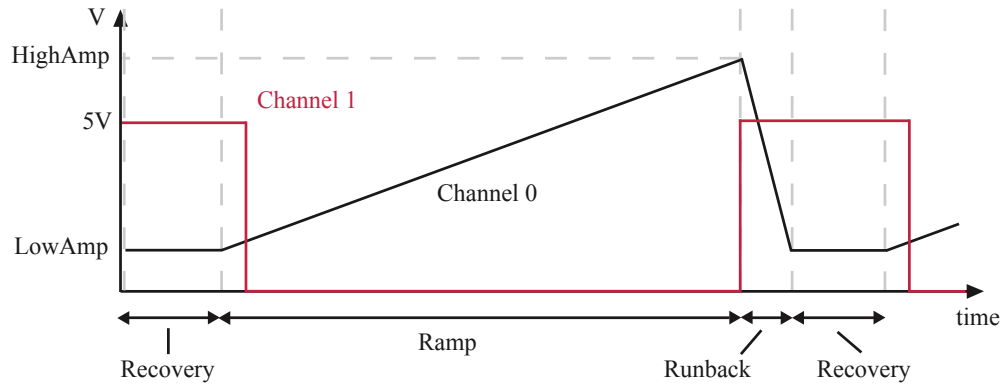


**Figure A.2:** Waveforms generated by the arbitrary waveform generator (M68 M-Module). Channel 0 is used to generate the linear voltage ramp that is applied to the Piezo of the scanning etalon. During the runback phase, the voltage is driven back to the initial value and the Piezo can relax to its starting position during the recovery phase. The output of channel 1 is a square wave used for suppression of peaks that are detected during the runback and recovery phases.

the Piezo voltage by 64 V, corresponding to more than two free spectral ranges of the etalon. After reaching the maximum value, the voltage is driven back to the minimum value. During this short runback phase of 3% of the cycle, the Piezo's position is not well defined, because the bandwidth of the amplifier is too low to follow the input signal. To allow the Piezo to recover back to its initial position and reduce hysteresis effects, the voltage is kept constant during the last 10% of a cycle. TTL pulses might also occur from the transmission fringes appearing during the runback and recovery phases. These pulses are suppressed by gating the counters with a square wave.

As shown on the left side of Figure A.3, the output of channel 1 of the AWG is fed to an OR-gate together with the TTL output of the HeNe peak detector. The resulting signal – shown schematically to the right – is fed to the input of counter 0 of the M72 module. Counter 0 is started by the first falling edge and stopped by the following rising edge (by operating it in its so-called PERIOD\_MODE) and is reset at the end of every full ramp cycle. The number of M72 clock cycles separating the falling edge of the square wave from the rising edge of the TTL pulse from the first HeNe-transmission peak corresponds to the actual value of the detected HeNe laser frequency. Counter 2 has the same input signals as counter 1, but is started on the first rising edge and stopped after the second rising edge (PULSE\_LOW\_MODE). This way, counter 2 measures the time corresponding to a full free spectral range of the etalon.

## A.4 Software stabilization loops

To correct the RDL frequency in a continuous control loop, two discrete software proportional–integral–derivative (PID) controllers [106] are implemented on the Kahlua Box.

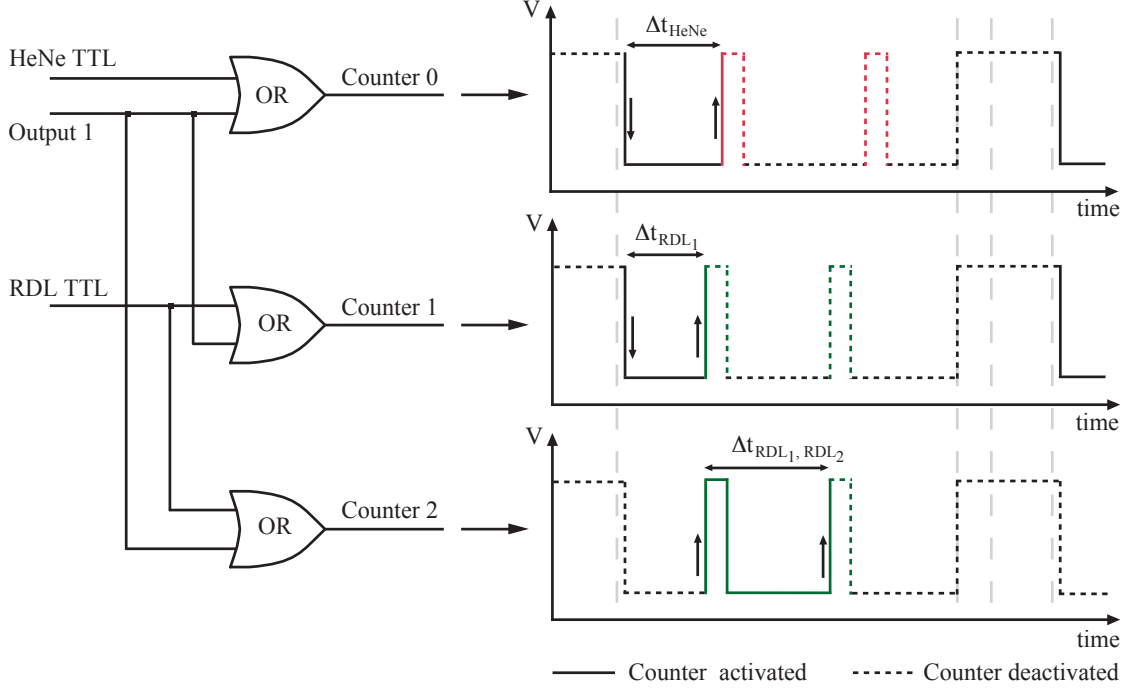


**Figure A.3:** Schematic diagram of the input logic for the Kahlua Box counters. Left: Schematic of the logic circuit processing the TTL pulses to activate the timers. Right: Dashed vertical lines indicate the phases of the sawtooth waveform shown in Figure A.2.

After each cycle of the Piezo ramp with duration  $\Delta t$ , i. e., at a typical repetition frequency of 100 Hz, an error signal,  $e_n$ , is calculated as the difference between the measured value,  $x_n$ , and the set point,  $s_n$ . From the error signal a control signal,  $y_n$ , is calculated that is sent as input to the controlled system, i. e., the servo motor of the RDL master cavity.  $y_n$  is the sum of a proportional component,  $y_{n,P}$ , an integral component,  $y_{n,I}$ , and a derivative component,  $y_{n,D}$ :

$$y_n = y_{n,P} + y_{n,I} + y_{n,D}. \quad (\text{A.1})$$

An efficient implementation of a discrete PID controller is achieved by deriving the following expression

$$y_n = y_{n-1} + c_0 \cdot e_n + c_1 \cdot e_{n-1} + c_2 \cdot e_{n-2} \quad (\text{A.2})$$

with the coefficients

$$\begin{aligned}
c_0 &= K_{\text{PR}} \cdot \left( 1 + \frac{\Delta t}{2T_i} + \frac{T_d}{\Delta t} \right) \\
c_1 &= -K_{\text{PR}} \cdot \left( 1 - \frac{\Delta t}{2T_i} + \frac{2T_d}{\Delta t} \right) \\
c_2 &= K_{\text{PR}} \cdot \frac{T_d}{\Delta t}.
\end{aligned}$$

$K_{\text{PR}}$  is the system's transfer coefficient,  $T_i$  is the integral action coefficient, and  $T_d$  is the derivative time coefficient, all of which need to be determined experimentally. Thus, the loop only has to keep track of the control signal in the previous sampling interval and the two previous error values. The coefficients  $c_0, c_1, c_2$  have to be calculated once for fixed parameters  $K_{\text{PR}}, T_i$  and  $T_d$ . As implemented in the RT-Kouda program, implemented by Heinz Junkes (FHI), the coefficients are recalculated on any change of the parameters while the sawtooth voltage is continuously applied to the scanning etalon.

The first controller stabilizes the time at which the HeNe transmission is detected (counter 0). Because the output frequency of the HeNe laser is well-defined, any change of its detection time can be attributed to drifts that result, for example, in a varying length of the etalon cavity. This is compensated by generating an error signal and adjusting the voltage offset of the sawtooth waveform after each period, thereby shifting the detection time of the first HeNe transmission fringe. As the Piezo ramp scans the etalon length over more than two spectral ranges per scan, a second transmission fringe occurs that is not used for detection.

The second controller corrects for the frequency drift of the RDL by stabilizing the detection time of one selected RDL fringe relative to the HeNe detection time (counter 1 or 2 relative to counter 0). The availability of two fringes for stabilization is important as the RDL frequency can be scanned by changing the set point of the time difference to the HeNe fringe. The controller automatically chooses the transmission fringe that is closest to the set point such that the RDL frequency can – in principle – be scanned over more than two spectral ranges of the scanning etalon in a single run.

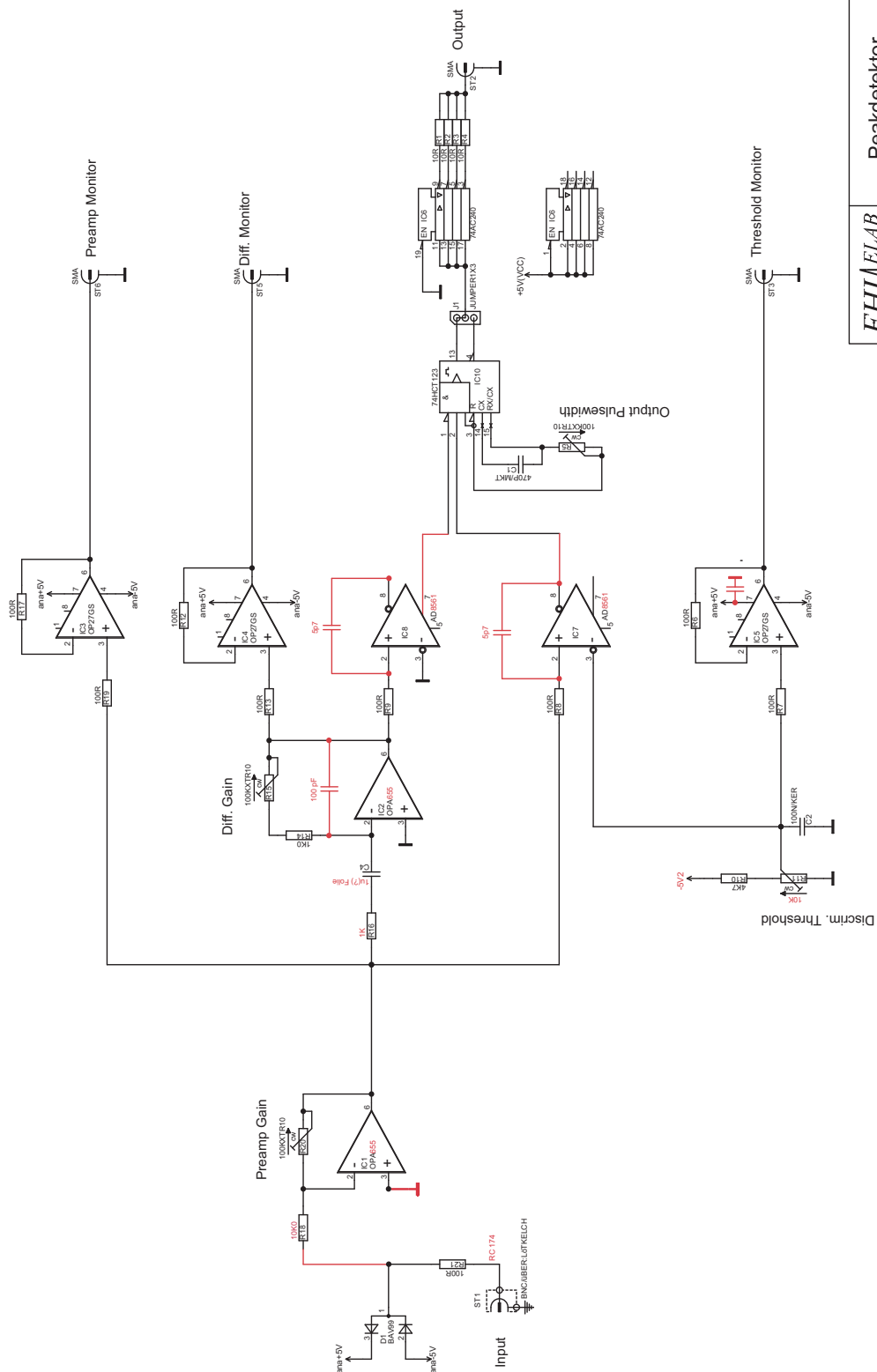


**Figure A.4:** Schematic circuit diagram of the peak detection electronics as developed by Victor Platschkowski, FHI Elab.

<b>FHI ELAB</b> #3398	Peakdetektor
Element: schaltung	
Filename: 3398_Peakdetektor.ddb	
Bearbeiter: VP	Version: 1.0 vom: 28.11.2005
Speicherzeit: 13.12.2005 . 12:48:19	Layoutversion: 1.0
© 2005 Fritz-Haber-Institut der MPG	Blatt: 1 (2)